INVESTIGATION OF SMALL SCALE (<50 M) SURFACE FEATURES ON MARS' NORTH POLAR CAP USING DATA FROM HIRISE

TUE GIANG NGUYEN

A THESIS SUBMITTED TO
THE FACULTY OF GRADUATE STUDIES
IN PARTIAL FULFILMENT OF THE REQUIREMENTS
FOR THE DEGREE OF

MASTER OF SCIENCE

GRADUATE PROGRAM IN EARTH AND SPACE SCIENCE
YORK UNIVERSITY
TORONTO, ONTARIO

May 2018

Abstract

The North Polar Layered Deposits (NPLD) of Mars host a wide array of small scale (<50m) features likely to be formed by aeolian processes. Taking data from the High Resolution Imaging Scientific Experiment (HiRISE), features less than 50 m over the entirety of the NPLD are characterized and mapped. A 2D Fast Fourier Transform is used to infer general spacing and orientation tendencies of surface patterns where the results are compared with modelled winds. Whether these features can be formed by sublimation processes is also tested. Of the 559 pictures from 499 HiRISE images extracted, roughly 69% of features are found whose morphology suggest that they are aeolian in origin. Some ripples found align themselves with the local katabatic winds and their changing orientations are likely subjected to katabatic jumps. Sublimation-driven features, penitentes, that can form are found to orientate themselves east-west with the tilt pointing towards the equator. Atmospheric scattering was also found to assist in forming penitentes at high latitudes. However, their modelled size ranges from 10^2 - 10^3 m.

Dedication

To family and friends.

Acknowledgements

First and foremost, I want to acknowledge my supervisor, Dr. John Moores. It was an absolute pleasure working under him where his guidance proved to be instrumental for my work. His knowledge on anything planetary along with his eagerness to help is inspirational and I look forward to indulge in his enthusiasm in the sciences for future projects.

I want to thank Dr. Mark Gordon for being the chair of the defense committee and his recommendations for my research evaluation should not be understated. Academically, I'm honoured to be taught by Dr. Gordon as well as Dr. Gary Klaassen for their courses in atmospheric physics. I'd also like to give thanks to Dr. Marshall McCall and Dr. Peter Taylor for being part of defense committee.

The works of Alexandra Innanen is also greatly appreciated. Her help in gathering HiRISE data and subsequent analysis of the data alleviated my workload considerably. Dr. Jani Radebaugh's input on dune classification has also been very helpful in the surface features analysis done in this thesis. Dr. Christina Smith and her work on dealing with Martian atmospheric scattering was extremely helpful in getting me started on sublimation processes.

Members of the Planetary Volatiles Laboratory were quite encouraging during my time as a master's student at York University. Casey Moore and Jake Kloos were very accommodating as senior graduate students. Thank you to other members of PVL for making the last two years quite memorable.

Table of Contents

List of Tables

List of Figures

Chapter 1

Introduction

1.1 A Brief History

In recent history, there has been a huge drive towards planetary exploration, particularly Mars. From the 1960s to the 1970s, NASA began its Mariner program aimed at exploring Mercury, Venus and Mars. With Mariner 9 mission providing scientific data throughout and after the global-wide Martian dust storms, atmospheric properties such as diurnal variation and wind inferences from temperature fields were studied extensively paving the way for future research (Hanel et al., 1972). More recent and ongoing missions such as the Mars Science Laboratory (MSL) emphasized the goals of assessing habitability and environmental history on the Martian surface (Grotzinger et al., 2012). Future planned missions such as Mars 2020 aim to fulfill more daunting objectives such as storing samples in a cache for future sample-return missions and preparing for human exploration of Mars (Mustard et al., 2013). The field of Martian research has been integral to space agencies such as NASA, CSA, and ESA and will remain so in the near future.

Mars' proximity to Earth and the presence of a thin Martian atmosphere makes for an excellent case study for planetary research. Similar to Earth, the diverse Martian surface

was observed to have been affected by impact, volcanic, and tectonic activities (McCauley et al., 1972). Mars also has diurnal and seasonal atmospheric variation yet is different to Earth in experiencing dust storms on a global scale (Haberle et al., 1982). Insights into the dynamics of the Martian surface and atmosphere showcase the environmental diversity of planetary bodies outside of Earth and may hold valuable knowledge on the history of our solar system.

Studying the Martian environment requires observations from ground-based telescopes, orbital spacecraft, and surface vehicles. Ground-based telescopes can provide basic properties such as Mars' orbital mechanics. More recent spectroscopy from Earth-based telescopic measurements has helped to determine certain compositions of the surface such as sulfate minerals (Blaney and McCord, 1995). Orbital spacecraft such as NASA's Mars Reconnaissance Orbiter (MRO), however, have access to more remote locations and given adequate resolution, can also provide invaluable information about the Martian atmosphere. Surface vehicles such as NASA's MSL rover Curiosity allow for in-depth environmental analyses at the surface but are more constrained geographically.

Instruments from orbital spacecraft such as MRO's SHARAD (SHAllow RADar) provide information on surface and subsurface properties of Mars (Seu et al., 2007). Also on-board the MRO is the HiRISE (High Resolution Imaging Science Experiment) camera which allows for high resolution (up to 0.25 m/pixel) images of the Martian Surface. HiRISE's scientific objectives involve cratering, volcanic and tectonic studies. However, a particular objective of interest from HiRISE is the study of bedforms where interactions between the atmosphere and surface are investigated in-depth (McEwen et al., 2007). These interactions include aeolian processes where surface features are formed by past and present winds through deposition and erosion of materials. Other interactions can also involve atmospheric scattering of radiation that affects the sublimation and condensation of volatiles.

Aeolian processes are widely recognized to be important in forming surface features on

Mars. Landforms range from wind-sculpted features such as ventifacts and transverse aeolian ridges (TARs) to self-organizing sediment structures, such as dunes and ripples made of rock and ice particles. Such features were first identified in Viking Orbiter data, where Tsoar and Greeley (1980) identified dunes on many terrains across the planet. Hayward et al. (2007) continued this work by building the Mars Global Dune Database to observe aeolian-driven features across the surface of Mars. From the region of Nili Patera, Silvestro et al. (2010) observed the changing ripple patterns on barchan dunes suggesting local wind event(s) were strong enough for regional ripple migration. Bridges et al. (2012) later noted that low-frequency gusts along with moderate winds can aid in maintaining the migration trend found in the region.

Shifting the geographic focus to the north polar region, there have been many observations of aeolian activities on the cap and in the surrounding region. From looking at polar margin dunes, Thomas and Gierasch (1995) constrained wind components from analyzing the albedo contrasts of dunes. Byrne and Murray (2002) as well as Fishbaugh and Head (2000) have looked at surface features shaped by aeolian processes at the edge of the North Polar Layered Deposits (NPLD) to draw interesting implications on the evolution of the North Polar Cap. Work by Massé et al. (2012) on dune fields in the region revealed the transport of gypsum from the ice cap. On the cap itself, observations of kilometer-scale sedimentation waves made by Herny et al. (2014) proved to be analogous to megadunes (large bedforms filled with compound and complex dunes) on Mars. While rock particles and ice particles transported by wind are capable of forming aeolian features, their differences in composition and relative density can lead to differences in dune characteristics, particularly the sizes of the dunes (Durán et al., 2011).

In contrast to aeolian processes, the effects of insolation on surface volatiles which in turn can affect the terrain morphology via surface self-illumination is less studied on Mars. However, there have been studies of sublimation-driven surface features, or penitentes, both

on Earth and Pluto. Terrestrially, Cathles et al. (2014) have showed that these features are geographically bound to the mid-latitudes and have a strong preference towards orienting east-west due to earth's orbit. Further work by Claudin et al. (2015) delving into penitente formation found that the spacing is primarily controlled by a balance between heat conduction and vapor diffusion. Penitentes had not been conclusively identified outside of earth until Moores et al. (2017) supplied evidence of bladed terrain on Pluto's Tartarus Dorsa region. Surface water and carbon dioxide ice capable of forming penitentes on Mars are more abundant on the poles which make the polar regions most likely to host these sublimation-driven patterns, if the conditions are right.

1.2 Background Information

1.2.1 Properties of Mars and its Polar Caps

Mars is similar to Earth for a variety of reasons. Mars' rotational period is 39.5 minutes longer and its 25.2^o tilt relative its the orbital plane allows for seasonal variations across its hemispheres. However, Mars has a higher eccentricity (ϵ=0.09) than the Earth (ϵ=0.01). Differential heating between the equator and the poles creates circulation within the atmosphere transporting heat and material over the entire planet. Atmospheric dynamics of both Earth and Mars are therefore dependent on complex weather systems of varying scales.

Despite the similarities in orbital mechanics in terms of day length and obliquity, there are still significant differences between the atmosphere of Earth and Mars. The Martian atmosphere is much thinner where the Phoenix mission measured the surface pressure from Ls 77-148 at the polar region (69^o N) to be around 7.2-8.6 mbar (Taylor et al., 2010). Its composition is 95% carbon dioxide as opposed to the nitrogen dominated atmosphere of Earth. However, there are still traces of water in the Martian atmosphere where ESA's Mars Express mission have measured the summertime polar region to have over 40 pr-μm of water

(Fouchet et al., 2007). This allows for hydrological cycles on Mars in terms of condensation, deposition and sublimation. In winter, the polar regions are cold enough for carbon dioxide to condense onto the surface, leading to a global pressure drop.

The layered deposits of the Martian polar caps have been observed to be asymmetric. The North Polar Layered Deposits (NPLD) lie within Vastitas Borealis dropping to around 5 km below the mean Martian surface while the South Polar Layered Deposits (SPLD) lies on the highlands reaching altitudes of 1-1.5 km above the mean Martian surface. The mean Martian surface, here, is the mean radius determined by the Mars Orbiter Laser Altimeter (Smith et al., 2001) instead of the reference pressure level of 6.1 mbar which is subjected to seasonal variability (Smith and Zuber, 1998). Both PLDs are overprinted by large troughs although the troughs of the SPLD have a wider range of symmetry and depth (Smith et al., 2015).

The cratering record of the SPLD suggests a surface age of 10^7 yrs (Koutnik et al., 2002). As the name of the layered deposits implies, the PLDs are domes composed of dusty water ice. Both polar regions show etch pitting that seems to be a unique process to the poles (Soderblom et al., 1973). Analyzing the geology of the south residual cap has shown depositional and ablation events suggesting repetitive formation of the southern cap morphology attributed to periodic variation in Mars' orbit and obliquity (Thomas et al., 2000). From studying the erosional pits in the southern cap, Thomas et al. (2016) calculated the annual change of the south polar cap to be between -6 to 4 km^3 per Martian year and that the cap had been steadily cycled with large dust events occasionally altering this steady behaviour.

By contrast, ice stability models suggested that the NPLD has accumulated within the last 5 million earth years during the period of low obliquity (Laskar et al., 2002). Using the cratering record, the surface age of the NPLD is seen to be around 10^5 yr (Tanaka 2005). The difference in surface ages of the PLDs can be attributed to the altitude difference of

6.4 km where volatiles condense more easily in the higher surface pressure conditions of the northern lowlands (Herkenhoff and Plaut, 2000). The stratigraphy of the top 250 m of the NPLD is best matched with a theoretical deposition rate of 0.05 cm/yr (Byrne 2009). The earlier work of Fishbaugh and Head (2000) detailed the presence of longitudinal dunes in the Olympia lobe and Byrne and Murray (2002) later suggested that the material there is an extension of the basal unit of the NPLD. While the large stratified domes on the PLDs appear to be stable in current climate, the basal units suggests both domes were not stable in earlier Martian climate implying that past Martian obliquity may have exceeded 40^{o} (Byrne, 2009). Smith and Holt (2015) separated the NPLD into different regions from their survey of the troughs and this is very useful for regional physical properties that will be discussed at later chapters. This is included as figure 1.1.

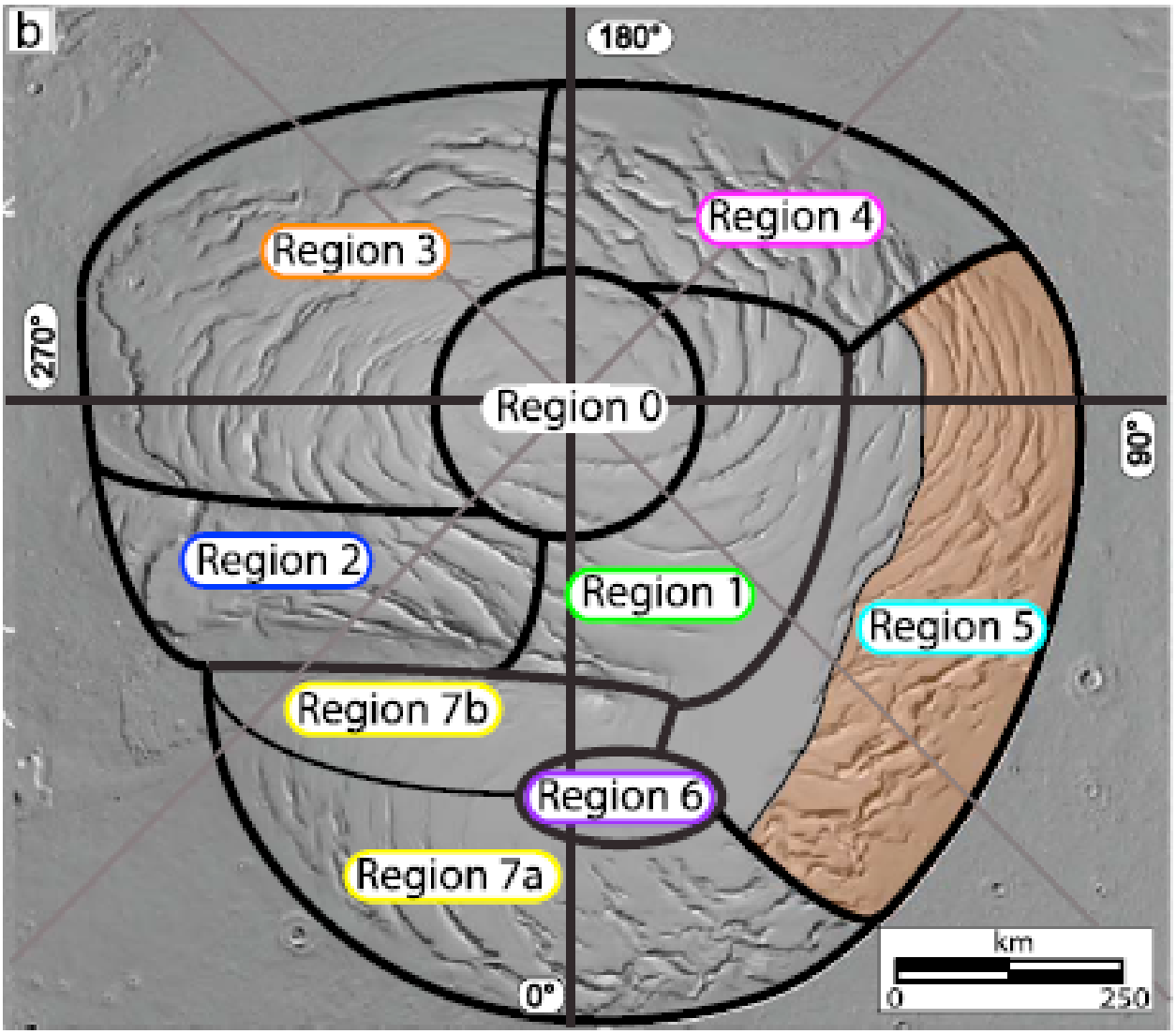

Figure 1.1: Figure 1 of Smith and Holt (2015) where the NPLD is split into 9 regions.

1.2.2 Polar Dynamics

When looking at the north polar erg via the Viking Orbiter, Tsoar et al. (1979) discerns two predominant wind directions in the summer: off-pole katabatic winds that become easterly and on-pole winds that become westerly. The winds were derived from analyzing dune shapes and their slipface orientation. In the winter and spring, on-pole winds predominate. In the summer, each of the two wind directions can dominate in various regions or wind belts detailed in figure 1.2. Their work also noted the prevalence of summer cyclones 110°-220° W along the edge of the cap that generate high velocity winds which favoured sand accumulation. The coriolis-deflected off-pole winds possibly interacting with ablation are likely to account for the spiral patterns of troughs on the NPLD (Howard, 2000; Smith and Holt, 2010). The work of Hansen et al. (2012) detected active sand transport in ergs surrounding the polar cap suggesting the current Martian climate is actively maintaining these dunes.

An important dynamic within the polar region, mainly in wind flow, is the prevalence of katabatic winds. Katabatic flow, or drainage flow, occurs when cold and dense air is formed at high elevations making it negatively buoyant. The natural tendency for these packets of air is to descend, which is accelerated by the downward sloping terrain. Conversely, anabatic flow occurs when the air is warm and less dense which is likewise accelerated up the slope. These flows are in no way restricted to polar regions and are favoured to occur in large sloping terrain with strong diurnal temperature variation and weak ambient winds (Savijarvi and Siili, 1993). These "slope" winds can cause the wind vector to rotate throughout the day (Moores et al., 2010; Holstein-Rathlou et al., 2010). Such flows are likely to occur across the Martian surface and can be analogous to terrestrial deserts where anabatic flow prevails in the day and katabatic flow prevails in the night (Parish and Howard, 1993). However, katabatic winds on Mars are very similar to the winds observed over the Antarctic Plateau (Parish and Howard, 1993). Katabatic winds have been confirmed to be prevalent on the

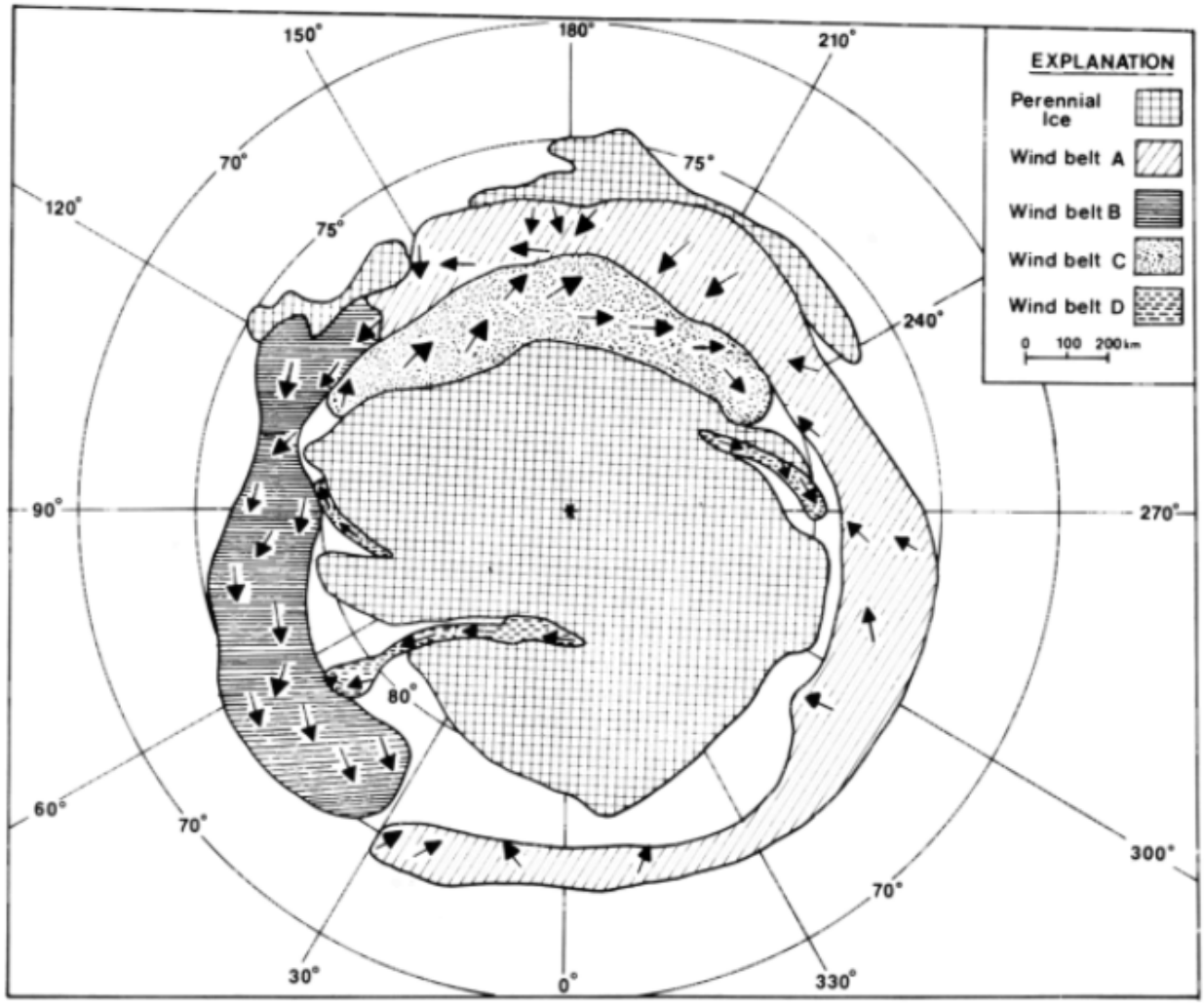

Figure 1.2: Figure of inferred wind belts in the Martian north polar region from Tsoar et al. (1979).

PLDs through low altitude clouds formed by katabatic jumps where the flow encountering a trough creates significant changes in pressure, wind speed and temperature (Smith et al., 2015). These clouds are shown in figure 1.3. While figure 1.2 from Tsoar et al (1979) lacks inferred wind on the cap, Massé et al (2012) was able to derive katabatic flow on the cap through their investigation of gypsum distribution on the polar region. This is shown in figure 1.4.

Other polar dynamics involving the sublimation and deposition of both water and CO_2 ice are important to the overall climate of Mars. The high-albedo ice, once deposited at the cap,

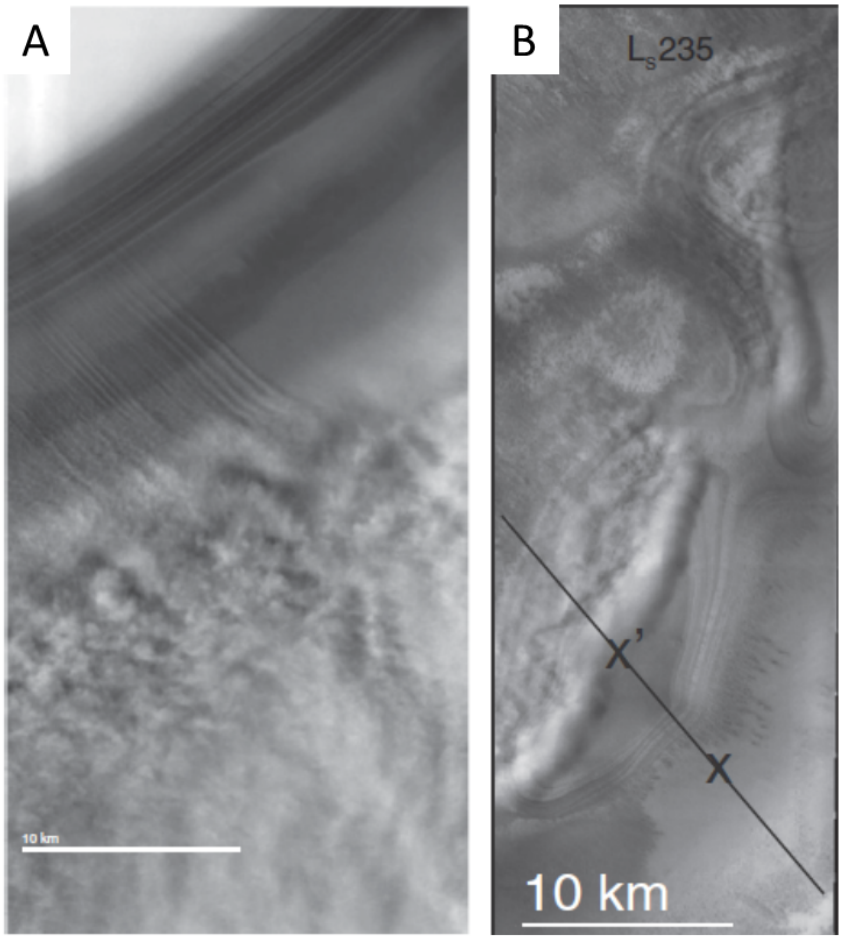

Figure 1.3: Panel A shows low altitude clouds caused by katabatic jumps taken at the NPLD (Smith and Holt 2010). Panel B shows the clouds at the SPLD (Smith et al., 2015).

acts as a trap for water vapour that partially dehydrates other warmer areas (Kieffer et al., 1976). This positive feedback provides potential to build very thick polar caps and gives rise to a very sharp contrast of albedo and temperature compared to surrounding regions (Kieffer et al., 1976). Data from the Viking Orbiter suggests that the cap is a major source of water in the summer but the weak polar circulation does not transport water very far from the cap (Haberle and Jakosky, 1990) yet observations from Mars Express show net sublimation of water in the summer on the cap (Langevin et al., 2005). Furthermore, Langevin et al.'s (2005) observations from OMEGA/Mars Express looking at albedo variation showed that in the northern summer, smaller ice grains (<100 μm) sublimate first leaving behind larger grains of permanent ice around 1 mm in size. By midsummer, analysis of albedo spectra

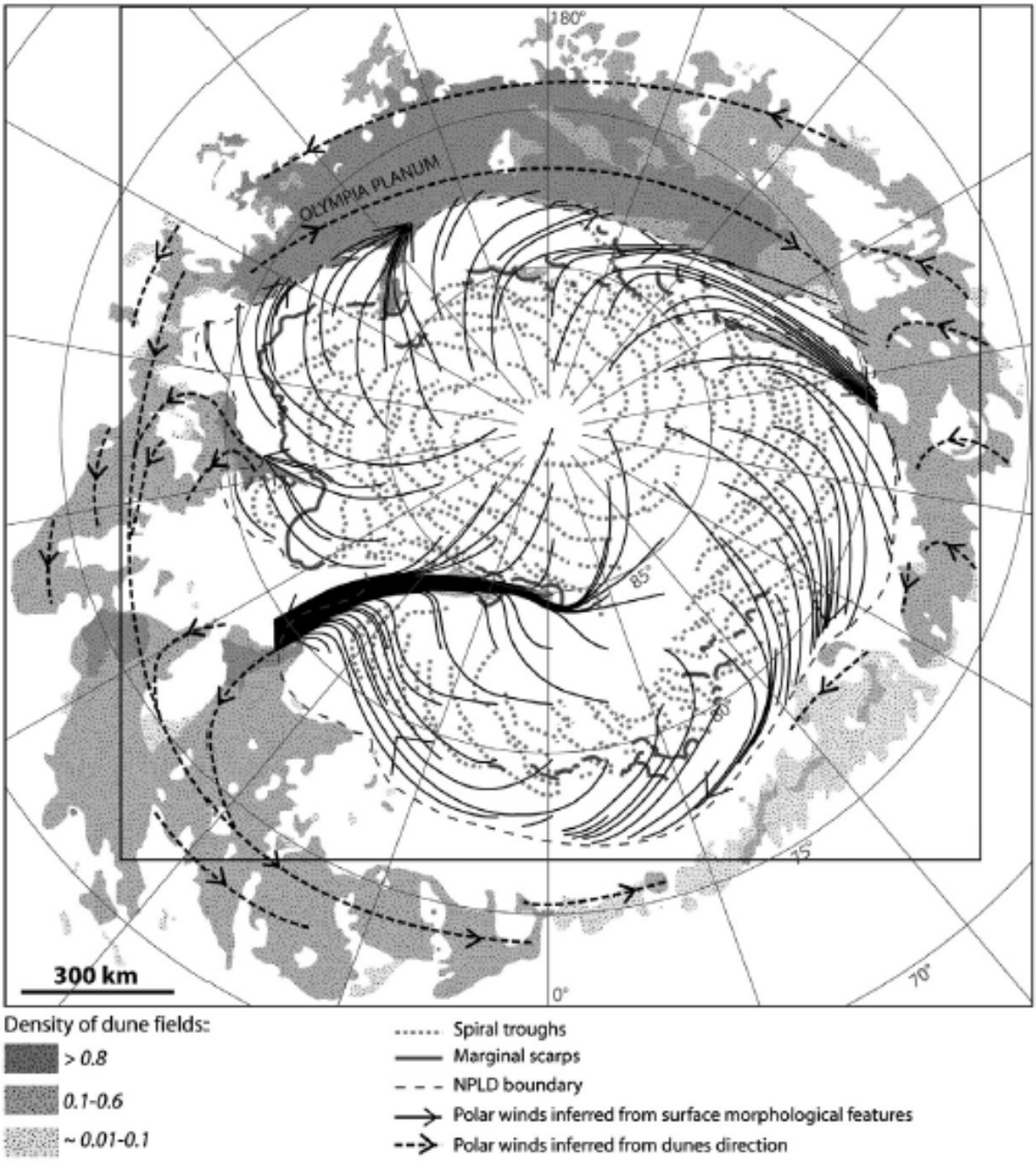

Figure 1.4: Figure shows inferred katabatic flow from Massé et al (2012).

showed that the ice still has low levels of dust-contamination suggesting either global dust storms deposit very little dust or that the sublimation process cleans the ice of dust. Hansen et al. (2012) has shown that sublimation of CO_2 can entrain surface material; this is discussed more in depth in subsection 1.2.4.

1.2.3 Aeolian Processes on Earth

Although the focus of this work is Mars, much of what is known about ripples and dunes comes from studying aeolian processes on Earth. This section will provide a brief qualitative explanation on the formation mechanisms of terrestrial ripples and dunes, their important characteristics as well as how well this is able to relate to Mars.

Formation Mechanism

The bulk of studies on aeolian processes on Earth have been done on sand and therefore the focus will be on the aeolian transport of sand for now. Aeolian sand deposits and their bedforms are typically split into a distinct hierarchy with three components: ripples, dunes and megadunes. The distinction between the three primarily derives from their different scales (although their morphology may be observed to be very similar to one another) with ripples occupying the centimetre to metre scale, dunes occupying the tens-of-metre to hundreds-of-metre scale and megadunes occupying the kilometre scale. This sizing scale is affected by the associated length scale of the sand transport by their respective atmospheric regime (Pelletier, 2009).

Important processes in understanding aeolian sand transport are saltation and reptation. Saltation is the process where the wind picks up a sand grain and drops off the grain at a location downstream. Reptation consists of sand grains moving by small hops where they are ejected from the bedform caused by impacts from saltating grains. The distance that these grains travel is generally shorter than the saltation length. However, the ejected grain may be subjected to the uplift of wind which will direct it towards a saltating trajectory (Durán et al., 2011). Other terminologies include tractation, coined by Andreotti et al (2002), where the grains are simply dragged by the wind (although this process is more prominent in aqueous regimes) similar to avalanches except the main driving force is caused by fluid dragging as opposed to gravity. Another process, suspension, occurs when the grains are

lifted by the wind but end up staying in the air. Aeolian transport of sand can be summed up in figure 1.5 from Lancaster (1995).

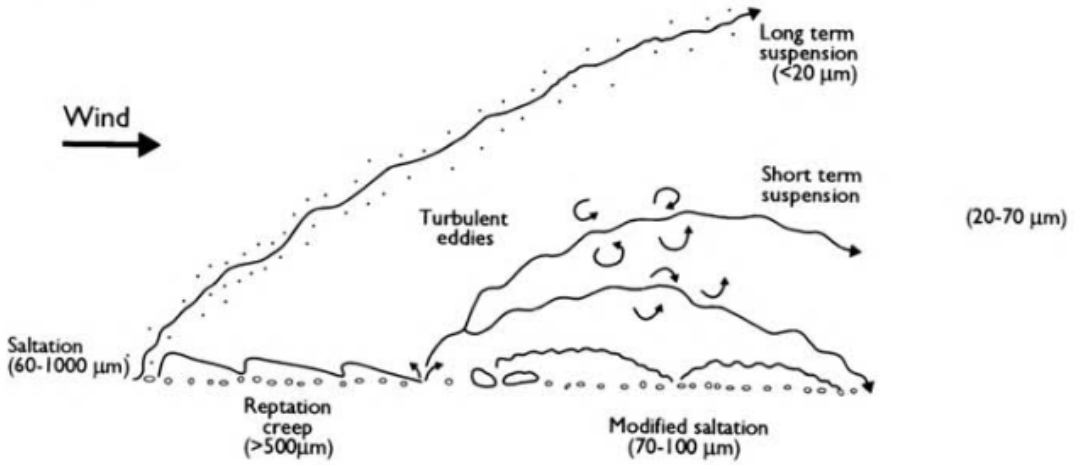

Figure 1.5: Figure of aeolian sand transport taken from Lancaster (1995).

Ripples can be formed from a flat bed with abundant sand supply where a saltating grain makes an impact with the bed to displace other grains at a relatively small scale. A past theoretical model from Anderson (1987) showed that a flat bed will be unstable to infinitesimal perturbation. His work also notes that the saltation distance may not be relevant to the scaling sizes of ripple wavelengths and is more dependent on the angle of high-energy impacts of saltating grains.

Unlike ripples that can form from a flat bed, the larger scale dunes require existing instabilities mainly the surface roughness. Since ripples that grow on a flat bed eventually become the dominant roughness element, ripples can then grow to become dunes. Using numerical models, Pelletier (2008) showed that spacing for both ripples and dunes are controlled by grain size and excess shear velocity. The hydrodynamics involved in the formation of dunes revolves around pressure perturbation due to surface roughness creating a zone of erosion on the high pressure area windward slope and depositional low pressure lee side (Kok et al., 2012; Charru et al., 2013).

Megadunes are large areas of aeolian sand deposits. They are compound and complex

dunes of varying scales that are superimposed on one another, especially on sand seas. Lancaster (1988) detailed two models for their development where one relies on climatic changes that create different wind regimes responsible for specific scales of dunes forming on the bed and the other revolves around flow conditions of rivers and estuaries. Ultimately, the formation of megadunes is suggested to have multiple periods of construction (Pelletier, 2008). General large bedforms capable of hosting a collection of dunes can be referred to as ergs. Wilson (1973) noted that in highland areas, there is a distinct absence of ergs due to the divergence of accelerating wind causing the undersaturated sandflow.

Characteristics of Ripples and Dunes

The work done by McKee (1979) on global sand seas, Lancaster (1995) and Melosh (2011) are excellent sources of characterizing dunes and ripples via their morphology. This section will delve into different classes of dunes and ripples spanning barchanoid dunes, transverse dunes, linear/longitudinal dunes and star dunes. This subsection aims to give adequate description of the morphology as well as conditions likely to give rise to these classes of aeolian-driven features. Visual appearances of the dunes mentioned are shown in figure 1.6 taken from Lancaster (1995).

Barchanoid dunes or barchans are curvy dunes and are likewise sometimes referred to as crescentic dunes. Their orientation, usually defined by the peak of their curve, should be aligned with the mean flow of the sand transport and are associated with relative low variability of effective wind direction. They are similar to transverse dunes except that they are more spaced apart due to differences in available sand to be transported (McKee, 1979).

Transverse dunes are wavy features, morphologically similar to ripples, tending to orientate perpendicular to the mean flow of aeolian sand transport. They are relatively asymmetric with a gentle stoss (windward) slope accompanied by a steep lee face (slipface). Because of their uniformity with respect to each other and orthogonality with the wind direction,

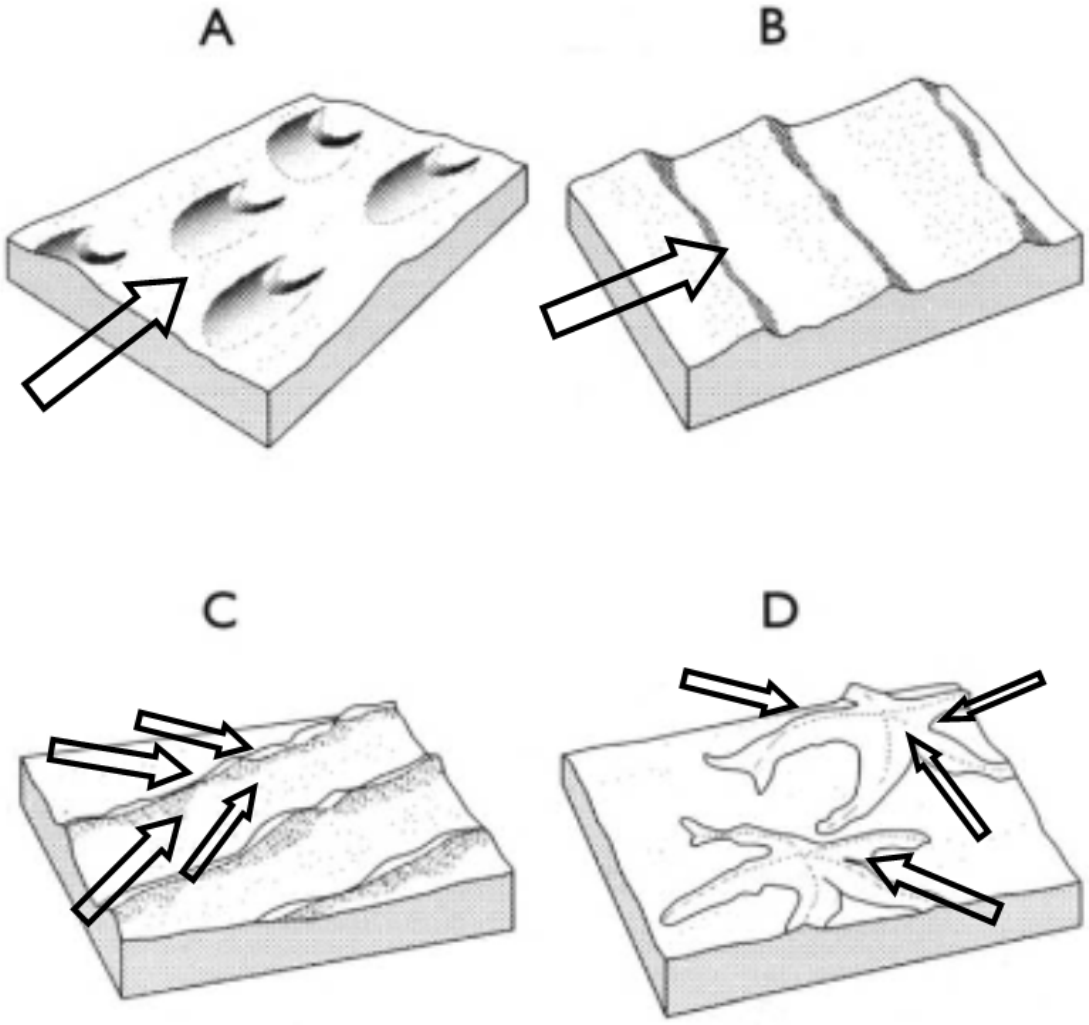

Figure 1.6: Figure showing different morphologies of various dune forms discussed in this thesis taken from Lancaster (1995) with prominent wind directions giving rise to the dune forms from Melosh (2011). Panel A shows barchans. Panel B shows transverse dunes. Panel C shows longitudinal/linear dunes and panel D shows star dunes.

their size and spacing follow spacing laws dependent on the densities of the air and grains and grain size (Durán et al., 2011). Transverse dunes have the same formation mechanism as barchans except transverse dunes are exposed to more available sand in the bedform (Melosh, 2011).

Linear dunes are distinguished from transverse dunes by their symmetry along the crest. This symmetry stems from the variability in wind direction in their formation process which

commonly gives them reversing crest and slipfaces (Rubin and Hunter, 1985). They are expected to be formed in areas with a wide unimodal or a bimodal wind regime. Their orientation has been observed to be more parallel to the wind than transverse dunes and barchans (McKee, 1979).

Star dunes have complex morphology which is likewise akin to their formation in complex wind regimes. They are common in very windy areas where dominant modes of wind directions may be directly opposed (McKee, 1979). Areas containing large and widely spaced star dunes tend to have a very fine and well sorted sand. By depositing sediment through climbing superimposed dunes on lee flanks, this process contributes greatly to the growth of large linear dunes and possibly star dunes (Lancaster, 1988).

1.2.4 Aeolian Processes on Mars

From building the Mars Global Dune Database by Hayward et al. (2007), dunes of many classifications have been observed on Mars although many dune forms found are not adequately classified by terrestrial standards. Looking at the region from 65° S to 65° N, a large percentage of dunes analyzed are classified as transverse. Examples of dunes found from this study are shown in figure 1.7. Of the dunes observed, Martian dunes are typically larger than their terrestrial analogues. Dunes observed in craters such as Kaiser, Rabe and Russell yielded an average wavelength/spacing of 510 m whereas dunes extensively studied in the Atlantic Sahara of Morocco yielded an average of 20 m (Claudin and Andreotti, 2006). Herny et al. (2014) also noted this discrepancy in size scales where large Martian sedimentation waves in the NPLD morphologically comparable to megadunes in Antarctica differ by one order of magnitude in spacing and two orders of magnitude in amplitude from their terrestrial counterparts. With observations made by the Curiosity rover, Lapotre et al (2016) investigated meter-scale wavelength wind-driven bedforms and suggested that they are fluid-drag ripples (where tractation is dominant) rather than terrestrial wind ripples (where saltation

and reptation are dominant). More recent work done by Vaz et al. (2017) looking at active and migrating meter-scale ripples on Herschel crater found a lack of transverse migration and concluded that the orientation of these meter-scale features is not required to align with the current wind regimes when formed.

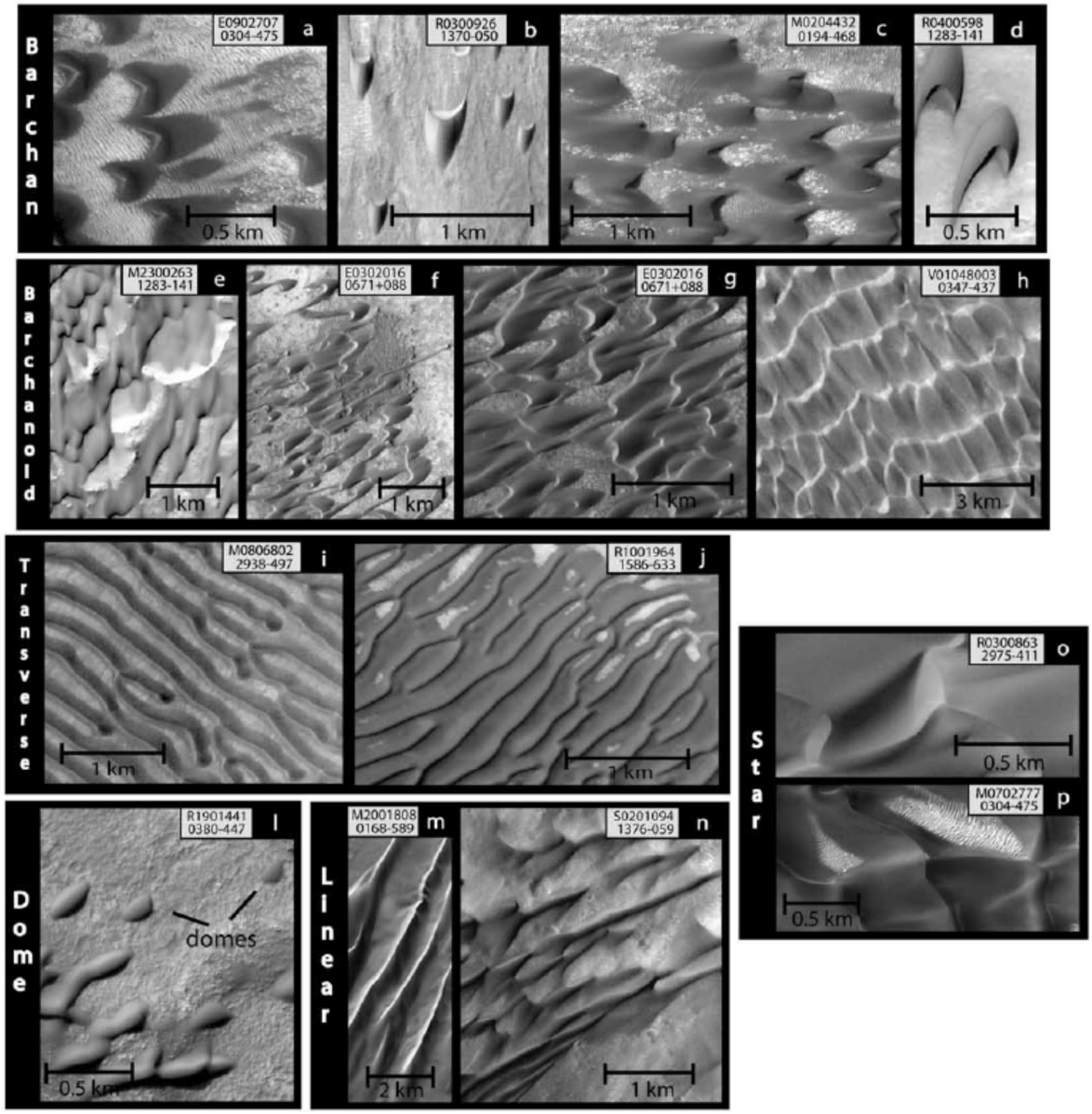

Figure 1.7: The figure shows examples of dune types found on Mars taken from Hayward et al (2007).

Despite the differences between Earth and Mars, scientists have not been deterred from exploring the dynamics of Martian aeolian processes. Tsoar and Greeley (1980) have made attempts to estimate characteristic grain sizes, deducing from the Viking Orbiter data that many barchan dunes in the north polar region are composed of fine sand (< 0.25 mm). Even though many Martian dunes are observed to be slow to evolve and some may even be static, Claudin and Andreotti (2006) argued that with grain sizes inferred from the rovers Spirit and Opportunity, Martian dunes should be active under the current climate. The active bedforms that have been observed in Nili Patera move 1-3 magnitudes slower than the fastest barchans on Earth found in Bodélé, Chad (Bridges et al., 2013). A more in-depth look into scaling laws implies that Martian dune wavelengths are 80 times larger than terrestrial dunes but the velocity threshold is in the same magnitude (1.4 times) as Earth (Durán et al., 2011).

Unique dynamics of Mars not found on Earth are the prevalence of dust transport and the sublimation of CO_2. Laboratory studies done by Rasmussen et al. (2015) stressed the importance of dust on aeolian processes as widespread dust can affect how sediments are transported. Dust particles coming into contact with one another leads to electrification which causes the dust particles to aggregate with each other through electrostatic attraction. Formation and subsequent breaking of aggregated dust can alter the dune scales where grain size and density play vital roles. Another observation common in Martian dunes is the sublimation of CO_2 which particularly affects dunes in the polar regions. Hansel et al. (2012) detailed this process where the CO_2 layer beginning to sublimate in the spring is weakened due to being thinner. Incoming insolation through the translucent ice layer accompanied with subsurface thermal conduction will lead to sublimation of CO_2 at the base of the layer building up gas in the process. The weakened ice layer eventually cracks wherever there is a significant slope due to the stress exerted by gravity. Numerical models suggest that the trapped pressurized gas underneath the layer escapes via the cracks and is capable of mobilizing loose sand grains thus entraining surface materials. Hansen et al. (2012) emphasized that CO_2 frost is often an agent for initiating sediment transport.

Other common surface features unique to Mars are the Transverse Aeolian Ridges (TAR). Because of their unknown origin, they were subsequently given a non-genetic name by Bourke et al. (2003). There has been much debate on whether they are ripples or dunes. Although many TARs are small bright crescents, they seem to have varying morphology and would therefore be prone to split into different characterizations such as forked or sinuous TARs, networked TARs and radial TARs (Geissler, 2014). Examples of TARs are shown in figure 1.8. Observations made by the Opportunity rover helped to infer that TARs-like features have a core composed of fine grains (< 0.25 mm) covered by granule-size (2-4 mm) grains (Balme et al., 2008). Because of this composition, there should not be significant migration under the current wind regime.

Upon studying bedform migration on Mars, Bridges et al. (2013) were able to confirm that all TARs are immobile. When observed in the Meridiani area, Balme et al. (2008) noticed that TARs transition into larger features suggesting the TARs in the area are ripples in nature. However, Zimbelman (2008) suggested TARs with high symmetry and height exceeding 1 m are likely to originate from dunes more consistently. Only recently has there been work done on a likely terrestrial analogue to TARs; Hugenholtz and Barchyn (2017) have found features in the Lut Desert of Iran to be morphologically similar to simple TARs. If the terrestrial features are indeed analogous to TARs, this implies that TARs are ripples.

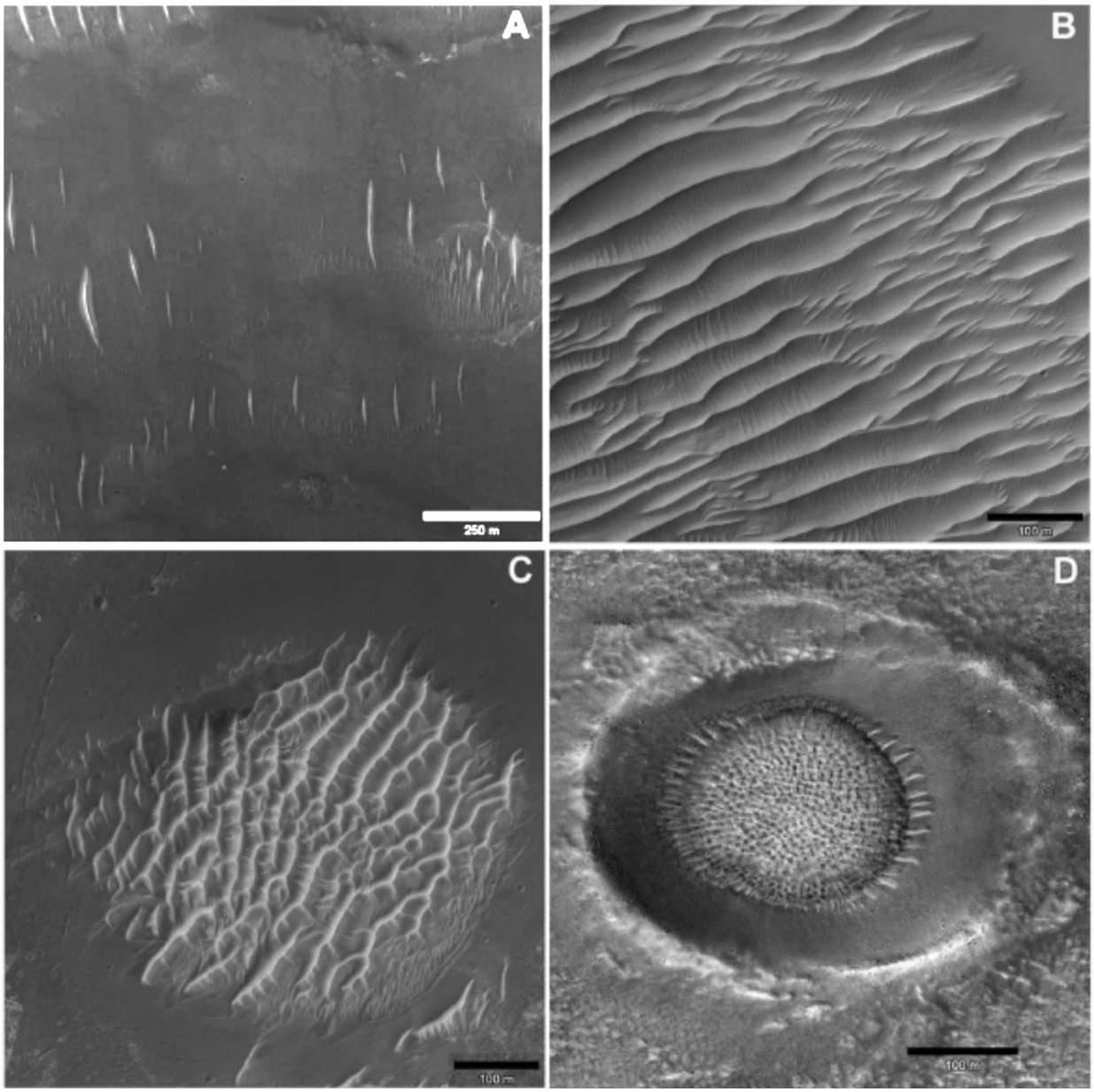

Figure 1.8: The figure shows examples of TARs found on Mars taken from Geissler (2014). Panel A shows simple TARs. Panel B shows sinuous and forked TARs. Panel C shows networked TARs. Panel D shows radial TARs.

1.2.5 Sublimation-Driven Features: Penitentes

While aeolian processes are prevalent in shaping the Martian surface, it is also useful to investigate other processes such as sublimation that drives the formation of penitentes. Penitentes are jagged blade-like patterns that formed naturally from ice and snow found at high altitudes where there is low humidity accompanied with strong insolation (Claudin et al., 2015). With limited observations of penitentes in Greenland and Antartica, most penitentes are found within 37° S to 46° N. These surface features are also observed to have a strong tendency to orientate in an east-west direction with flat surfaces facing the equator (Cathles et al., 2014).

Cathles et al. (2014) focused on intra-surface radiative transfer where insolation is trapped by reflections between the walls of the ridges. Their work starts by considering a contour representing the cross-section of the penitentes where the sun is simulated shining onto the penitentes for an extended period of time. The model was able to show that the sun's path throughout the year does indeed play a role in geographically restricting the formation of penitentes and forcing them to orientate equator-ward. Finding favourable conditions for the formation of penitentes is accomplished by maximizing radiation from the sun, directly or indirectly as light bounces off the high-albedo snow or ice, into the bottom of the penitente ridges. While this accounts for the orientation tendency, the sizing scale of penitentes requires additional calculation. Taking into account physical processes, Claudin et al. (2015) formulated a model with heat conduction and vapour diffusion in mind. They were able to derive a scaling law for penitentes growth and stressed the importance of vapour mixing above the ice/snow surface.

Outside of earth, it is still possible to form penitentes. Moores et al. (2017) have shown that Tartarus Dorsa on Pluto does host penitentes. Taking data from the New Horizons spacecraft and comparing with penitentes growth models, they were able to reproduce trimodal orientation and the spacing of the Plutonian penitentes. These kilometer-scale features

are shown to be composed of Methane ice that has a formation timescales of approximately 10^7 years. The study of penitentes is helpful for understanding atmospheric dynamics by providing insight about the energy budget as surface roughness reduces the effective albedo of the surface (Cathles et al., 2014).

1.3 Objectives

Overall, there are relatively few studies of small scale (<50 m) surface features especially on the Martian polar caps where the northern polar region is the area of interest for this study. By gathering images taken from the HiRISE and using a 2D-Fast Fourier Transform (FFT) to infer spacing and orientation of patterns present in the images, this thesis aims to fill this gap by characterizing and mapping these surface features, especially features whose morphologies suggest that they are likely to be associated with aeolian activities or sublimation patterns. By comparing the orientations of the small scale features to larger-scale Aeolian features and model-derived wind fields (Massé et al., 2012), it is possible to test whether or not these small-scale features are indeed Aeolian in origin. Furthermore, by examining trends in the spacing of those features across the cap, it becomes possible to constrain the atmospheric processes which created them. The orientation and spacing is also compared with insolation models (Cathles et al., 2014; Claudin et al., 2015) to identify penitentes should their formation be possible on Mars.

This chapter served as introductory material for aeolian and sublimation processes. Chapter 2 will detail the methods used for the spectral analysis of features on the NPLD and the process behind simulating penitente growth on Mars. Chapter 3 showcases the results in terms of morphological characteristics of all the features found on the NPLD as well as results from the penitente growth simulations. Chapter 4 will discuss aeolian processes observed and their implication, whether penitentes can form on the NPLD, and possible

flaws in this work. Finally chapter 5 will summarize the discussion on aeolian-driven and sublimation-driven processes on the NPLD as well as avenues for future research on the topic.

Chapter 2

Methods

2.1 Spectral Analysis

This section deals with techniques used to infer spacing and orientation of features found in data from the High Resolution Imaging Experiment (HiRISE). Based on the works of Moores et al. (2015) when analyzing Martian atmospheric movies from NASA's Curiosity Rover and similar to Bechtel et al. (1990) when analyzing North American topography, spectral analysis techniques such as the 2D FFT are the preferred methods to systematically measure pattern tendencies for large sets of data. Another method, the variogram, is also explored as an alternate method to infer spatial and orientation distributions of the HiRISE dataset.

2.1.1 The 2D Fast Fourier Transform

Surface features formed by aeolian processes or sublimation follow patterns that exhibit regular trends in spacing and orientation. Repeating patterns are good candidates for a frequency domain analysis such as Fourier transforms. Fourier transforms in 1-dimension,

common in signal processing, treats a signal as a weighted combination of sinusoids varying in frequency, amplitude/power and phase shifts. When using the 2D Fourier Transform, the output also yields weighted combinations of sinusoids but frequencies can now vary spatially where orientation inferences are possible. Ultimately, the 2D-FFT finds periodic variations in pixel brightness within an image and characterizes the variations found as a combination of sinusoidal waves. Computationally, a Discrete Fourier Transform algorithm is used to sample a smaller range of frequencies which is determined by the size of the image to be transformed.

Images taken from the HiRISE are used for the analysis of surface features on Mars' northern cap because of their very high resolution on the cap of 0.25 m/pixel or 0.5 m/pixel. Using the Java Mission-planning and Analysis for Remote Sensing (JMARS) software, map-projected images are downloaded and are visually scanned for any noteworthy surface patterns. A 2048x2048 pixel frame is extracted for any areas of interesting surface features within the HiRISE image. This process is shown in figure 2.1.

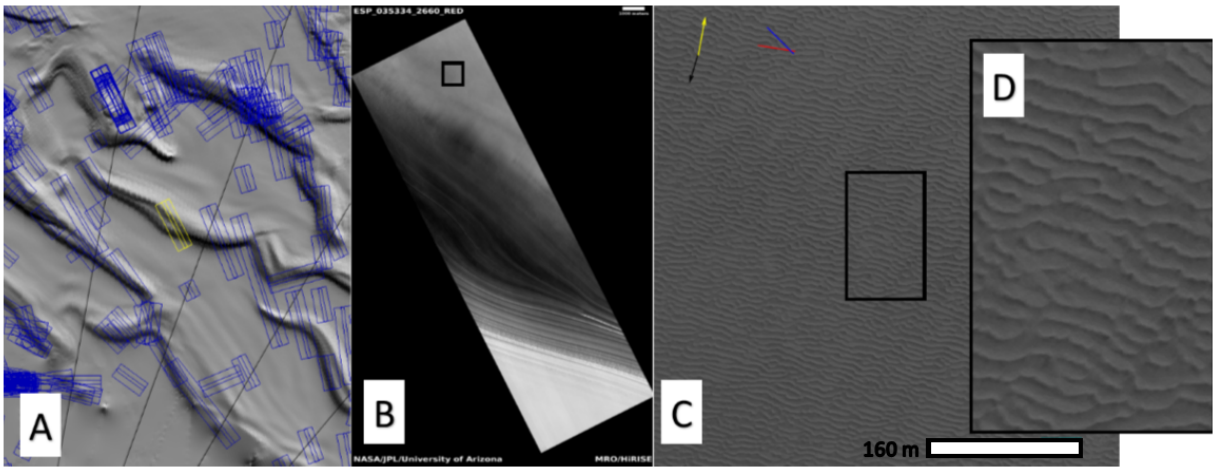

Figure 2.1: HiRISE image ESP_035334_2660. Panel A shows outlined HiRISE stamps overlaying a digital elevation map of the NPLD. Panel B shows the map-projected HiRISE image represented by the yellow outlined stamp from panel A. Panel C shows the frame extracted from the boxed region from panel B. On panel C, the black arrow on the top left of the panel points to north while the yellow arrow points to the direction of the sun; the size scale is located on the bottom right. Panel D shows the magnification of the boxed region in panel C.

The use of frequency-domain analysis has been previously used by Bechtel et al. (1990) in determining the thickness of the lithosphere in North America. Further use of frequency-domain analysis was done by Moores et al. (2015) where a 2D Fast Fourier Transform (FFT) is used to distinguish between noise and cloud morphologies of atmospheric movies taken from Curiosity Rover on Mars. Similar to the works of Bechtel et al. (1990) where the frequency domain is compared between two datasets, topography and gravity data, Moores et al. (2015) used coherence analysis to compare the atmospheric movies dataset and simulated noise. This thesis uses the same technique as Moores et al. (2015) where the two datasets being compared are HiRISE images and noise. Noise is simulated by creating a second frame with the same size and brightness parameter as the HiRISE data. Each pixel from the randomized/noise frame is generated randomly from a normal distribution with the same brightness mean and standard deviation from the original HiRISE frame. A parabolic or Welch window (Welch 1967) is applied to limit spectral leakage from the effects of the FFT on pixels at the edge (Moores et al. 2015).

To reduce noise when calculating the spacing and orientation from the 2D FFT of the extracted frame, the 2D FFT of the randomized frame is radially averaged. Pixel values from the 2D FFT of the extracted frames are then subtracted from the averaged 2D FFT of the randomized frame. The spacing of the surface features are inferred from the frequency that has the largest extra power in the 2D FFT of the extracted frame as compared to the generated randomized frame. Orientation is inferred from finding the direction that corresponds to the peak in power of the subtracted 2D FFT. The orientation of the features is then taken to be the perpendicular to the peak in orientation of the FFT for easier human interpretation; the orientation inferred from the FFT is the direction in which waves propagate but in this case we define the orientation to be the orientation of the troughs and crests. This is shown in figure 2.2. When the spacing and orientation of the surface features are determined on an extracted frame, visual confirmation is done to ensure the FFT-derived value corresponds to an identifiable feature where a qualitative value for confidence of the

spacing and orientation is assigned. Extracted frames are then grouped together in terms of visual similarities for further analysis of the Mars' norther polar cap.

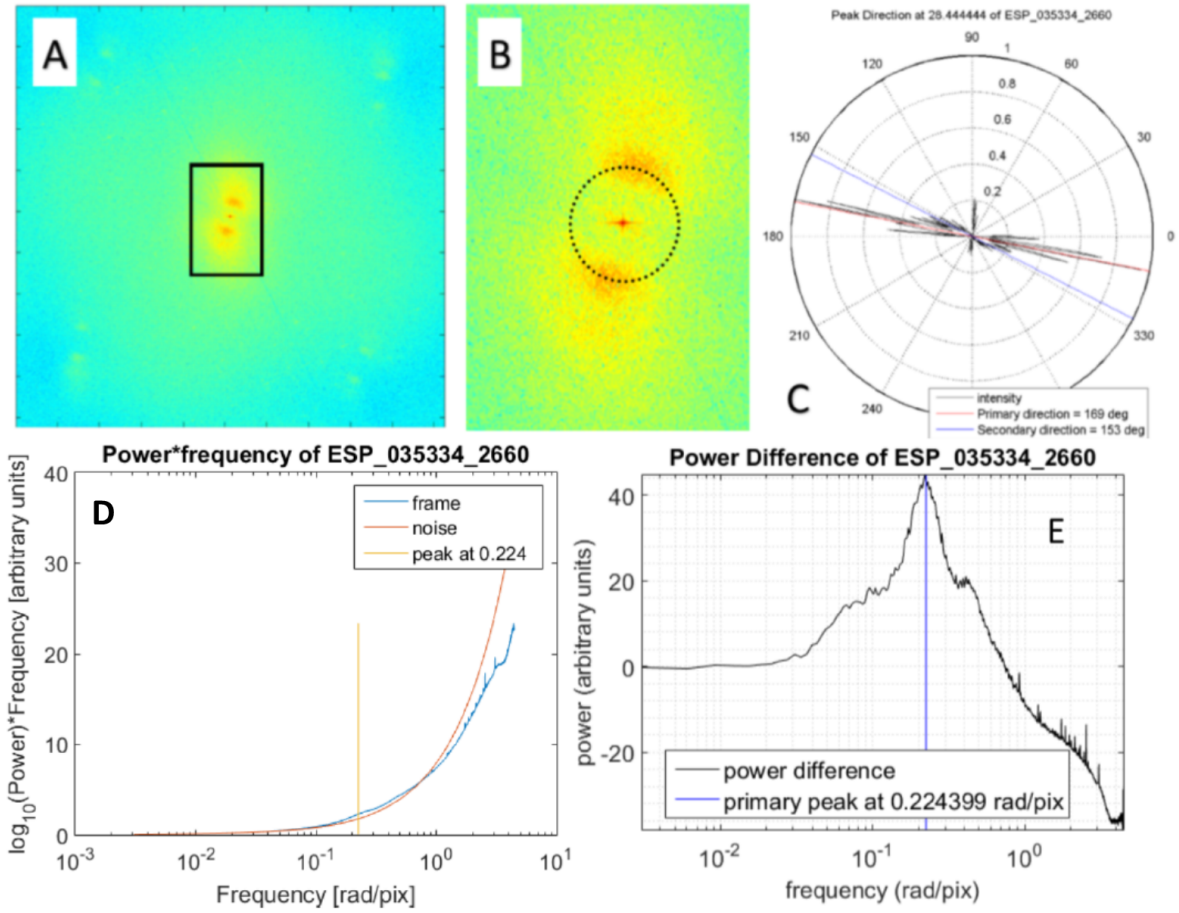

Figure 2.2: HiRISE image ESP_035334_2660. Panel A shows FFT output of the frame from figure 1. Panel B shows the magnification of the FFT output of the box on panel A. Panel C shows the power of different directions after noise reduction at the peak frequency highlighted as a dashed circle on panel B. Panel D shows the power spectra times the frequency of the HiRISE data labeled "frame" and simulated noise data labeled "randomized". Panel E shows the difference between the two datasets where the highest difference, the "primary peak", corresponds to the dashed circle on panel B.

The size of the frames extracted is chosen to be 2048x2048 pixels because it is computationally manageable while being reasonably accurate. Figure 2.3 shows the power spectra of the same HiRISE image but with different frame sizes ranging from 256x256 pixels to 4096x4096 pixels. On the power spectra plot in figure 2.3, it can be seen that the smaller the

frame, the less pronounced the peak of interest around the average peak frequency of 0.24 rad/pix. Therefore, the larger the frames that can be used for the FFT, the more confident the analysis. However, the runtime for the 2D FFT of a 2048x2048 pixel frame is generally 30 seconds while the FFT for a 4096x4096 pixel frame would take 180 seconds to run. When dealing with a large dataset and limited time, the selected size of a 2048 pixel square is preferable due to the balance between the accuracy of the spectral analysis and the time it takes to analyze the data.

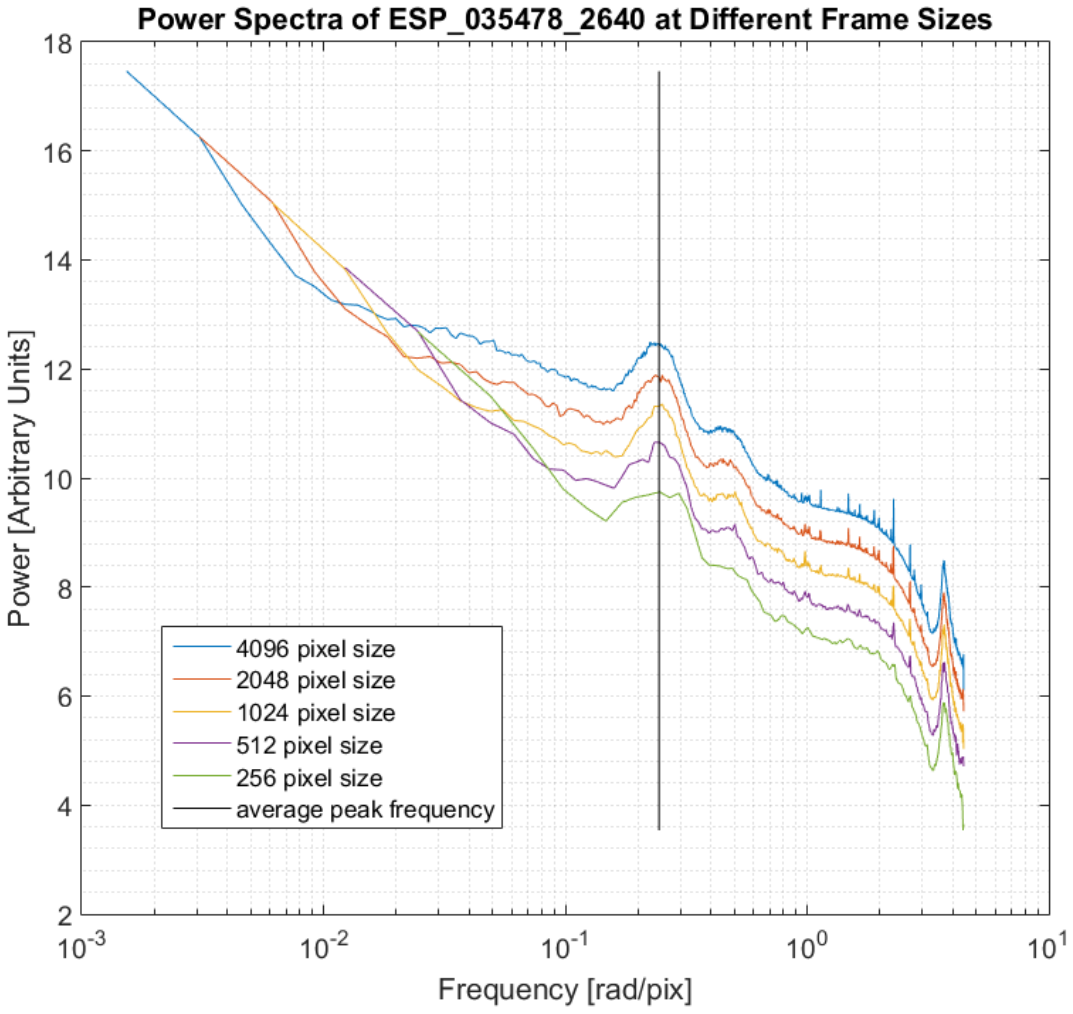

Figure 2.3: The figure shows the power spectra plots of different sized frames extracted from HiRISE image ESP_035478_2640 (The actual frame is featured and can be found in figure 4.5).

Since the 2048 size frames are fairly small representing generally less than 1% of the actual HiRISE image, it would be interesting to see how the FFT analysis varies across the entire HiRISE image. This is done in figure 2.5 where the frame used for the data is shown as figure 2.4 and the analysis for the entire HiRISE image is shown in figure 2.5. It can be noted that a HiRISE image can contain many different features, especially when a trough is present in the image. The example shown in figure 2.4 and 2.5 shows that the values inferred from the frame used for the dataset is a good representation of the entire HiRISE image as the most prevalent peak frequency and orientation tendency matches with the dataset frame. However, the orientation tends to vary much more than the spacing inferred.

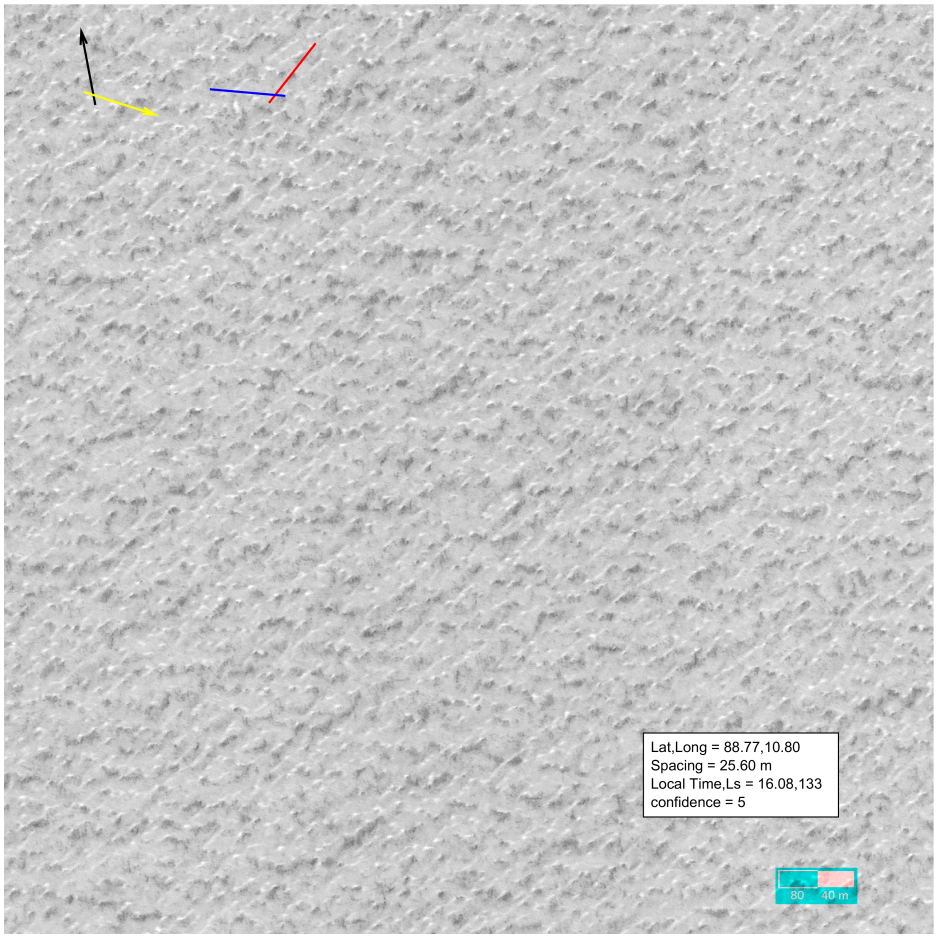

Figure 2.4: The figure is the frame used for the dataset taken from HiRISE image ESP_045443_2690. Within the image, the inferred spacing is 25.6 m which means the wavelength at the peak frequency is approximately 51 pixels. The orientation inferred in the frame is measured to be 52° counter-clockwise from the horizontal.

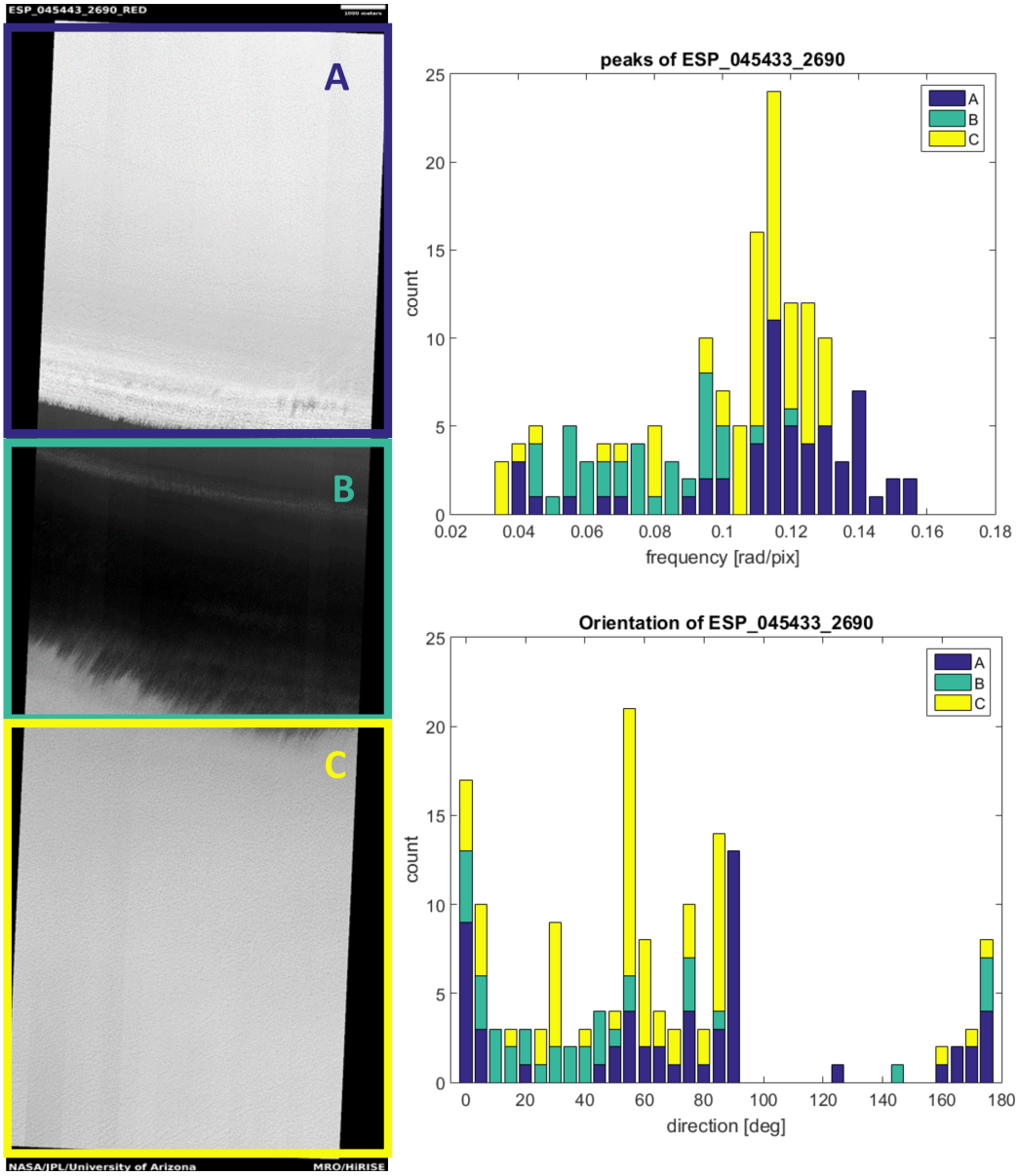

Figure 2.5: The figure shows the entire HiRISE image where figure 2.4 is taken from along with the FFT analysis for the entire image when partitioned into 154 2048x2048 frames. The left panel shows the HiRISE image being separated into 3 zones, each with different terrain and geomorphology. The frame used for the dataset, figure 2.4, was taken from zone C. The top right panel shows the histogram of prominent peak frequencies for the FFT analysis of the 154 frames in the HiRISE image. The bottom right panel shows the histogram of the orientation tendency inferred via the FFT analysis. For the peak frequency histogram, the bin size of the frequency is 0.005 rad/pix where the most prevalent peak frequency is 0.115-0.120 rad/pix corresponding to a wavelength of 52-55 pixels. For the orientation tendency histogram, the bin direction size is 5° where the most prevalent orientation tendency is 55°-60° counter-clockwise from the horizontal. The values used for the dataset, wavelength of 51 pixels and orientation of 52° from the horizontal, is fairly close to the most prevalent wavelength of 52-55 pixels and 55-60° orientation.

Confidence levels introduced ranges from 1 to 5. Confidence level 5 assigned to a frame signifies that the surface features observed are consistent and that the spacing and orientation inferred corresponds to an identifiable feature upon visual inspection. Confidence level 4 requires some manual input restricting the power spectrum peak finding to a specified frequency range but within that range, the spacing and orientation are consistent with visual confirmation; this is often the case for features of different scale superimposed on one another. An example of a frame with confidence level 4 is shown in figure 2.6 Confidence level 3 signifies that the orientation is consistent but the spacing is not whereas level 2 is vice versa. Confidence level 1 signifies that while there may be noteworthy patterns featured on the frame, the patterns are not consistent enough for the measured spacing and orientation from the FFT to make any physical sense. This is summarized in table 2.1.

Table 2.1: The table summarizes how confidence is introduced by seeing how inferred measurements from the FFT analysis visually compare to the features observed.

Confidence lvl.	description
5	consistent spacing and orientation
4	consistent spacing (in a specified range) and orientation
3	inconsistent spacing but consistent orientation
2	consistent spacing but inconsistent orientation
1	inconsistent spacing and orientation

Confidence levels of each frame can be subjective but there were some quantifiable aspects in assigning confidence from the FFT analysis. High confidence in spacing is generally accompanied with a prominent peak that can clearly be seen on the power spectrum plot and the power difference plot (figure 2.2 panel E and D). The width of the peak can also leave a clue on how consistently spaced the patterns on the frame are. The comparison between confidence in spacing is shown in 2.7. High confidence in orientation generally occurs when the power in the direction with the biggest power difference is roughly 10 times the average power at the specified frequency. Comparisons between high and low confidence in orientation is shown in figure 2.8. High confidence in orientation, especially for a wide range of frequencies, can also be assigned when it is visually obvious on the FFT output of

the frame.

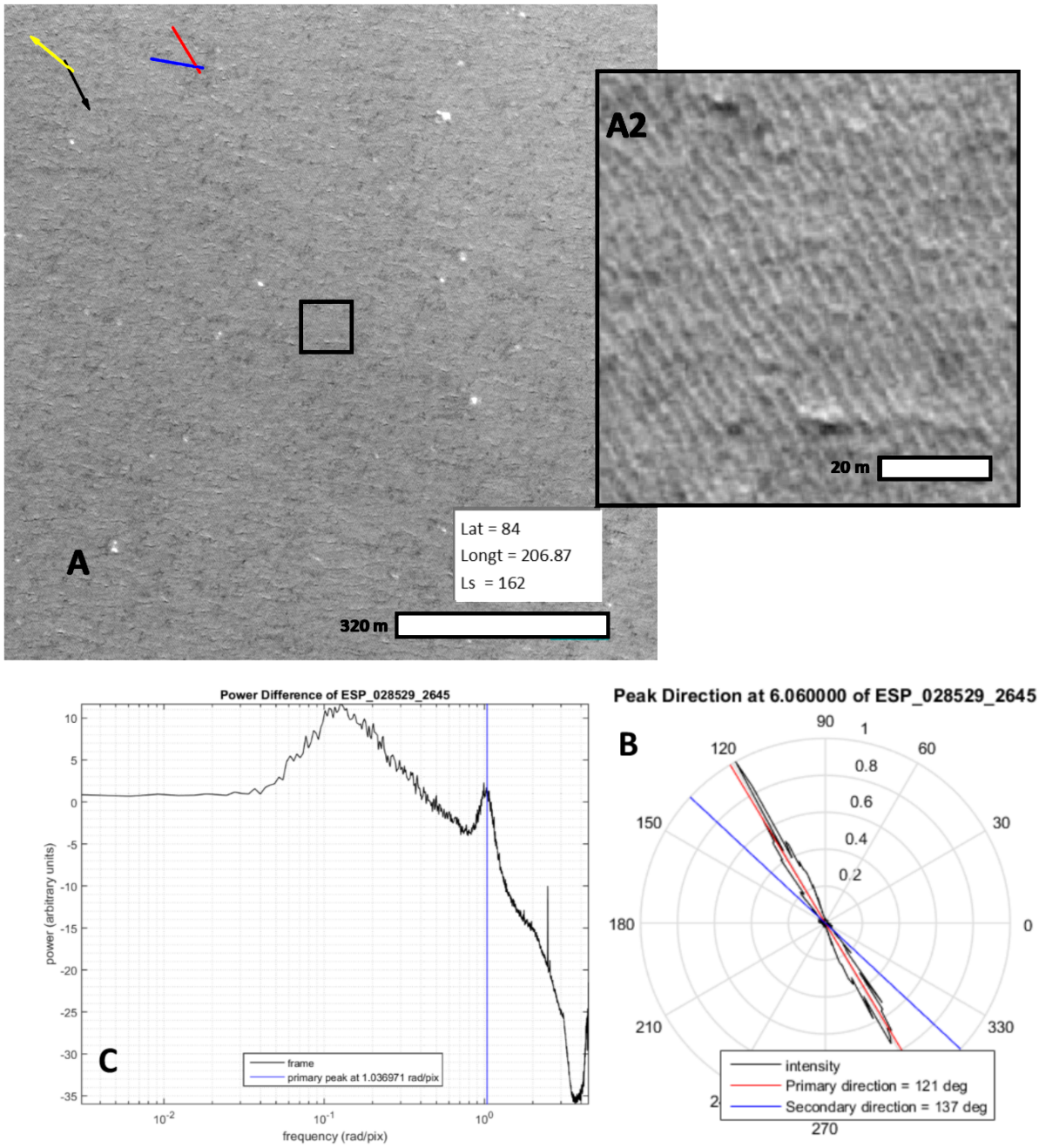

Figure 2.6: Panel A-C shows an example of a frame assigned a confidence level 4 from HiRISE image ESP_028529_2645. Panel A shows the extracted frame while panel A2 zooms in at the features. Panel C shows the power difference while panel D shows the different directions of power specified at the frequency labeled "primary peak" on panel C. The figure shows that the identifiable features correspond to a less pronounced peak at a higher frequency (inferred spacing of 3 m).

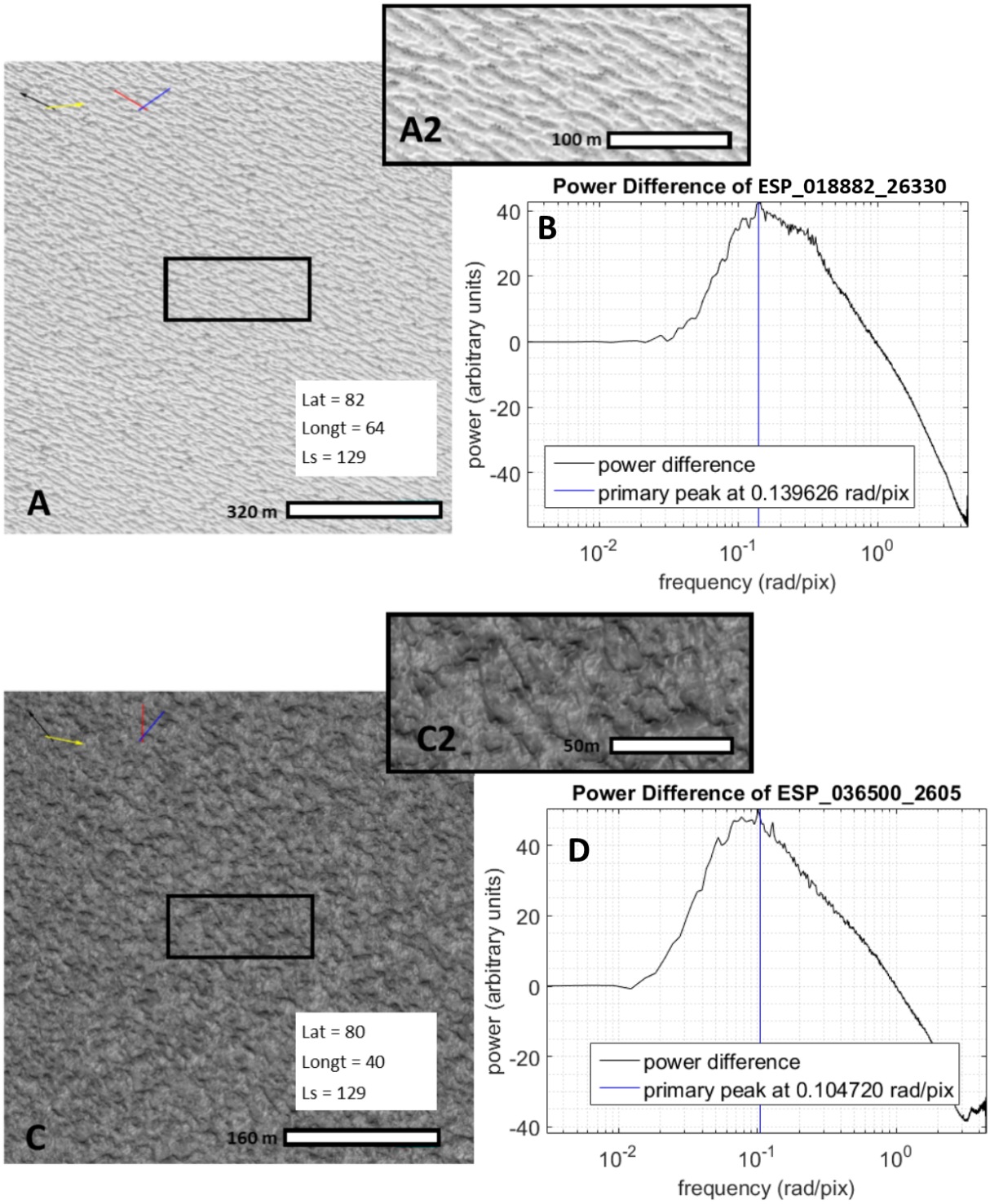

Figure 2.7: Panel A-B shows high confidence in spacing. Panel A shows HiRISE image ESP_018882_2630 while panel A2 zooms in the highlighted rectangle of panel A. Panel B shows the power difference where the inferred spacing corresponds to identifiable and consistent features. Panel C-D shows low confidence in spacing represented by HiRISE image ESP_036500_2605.

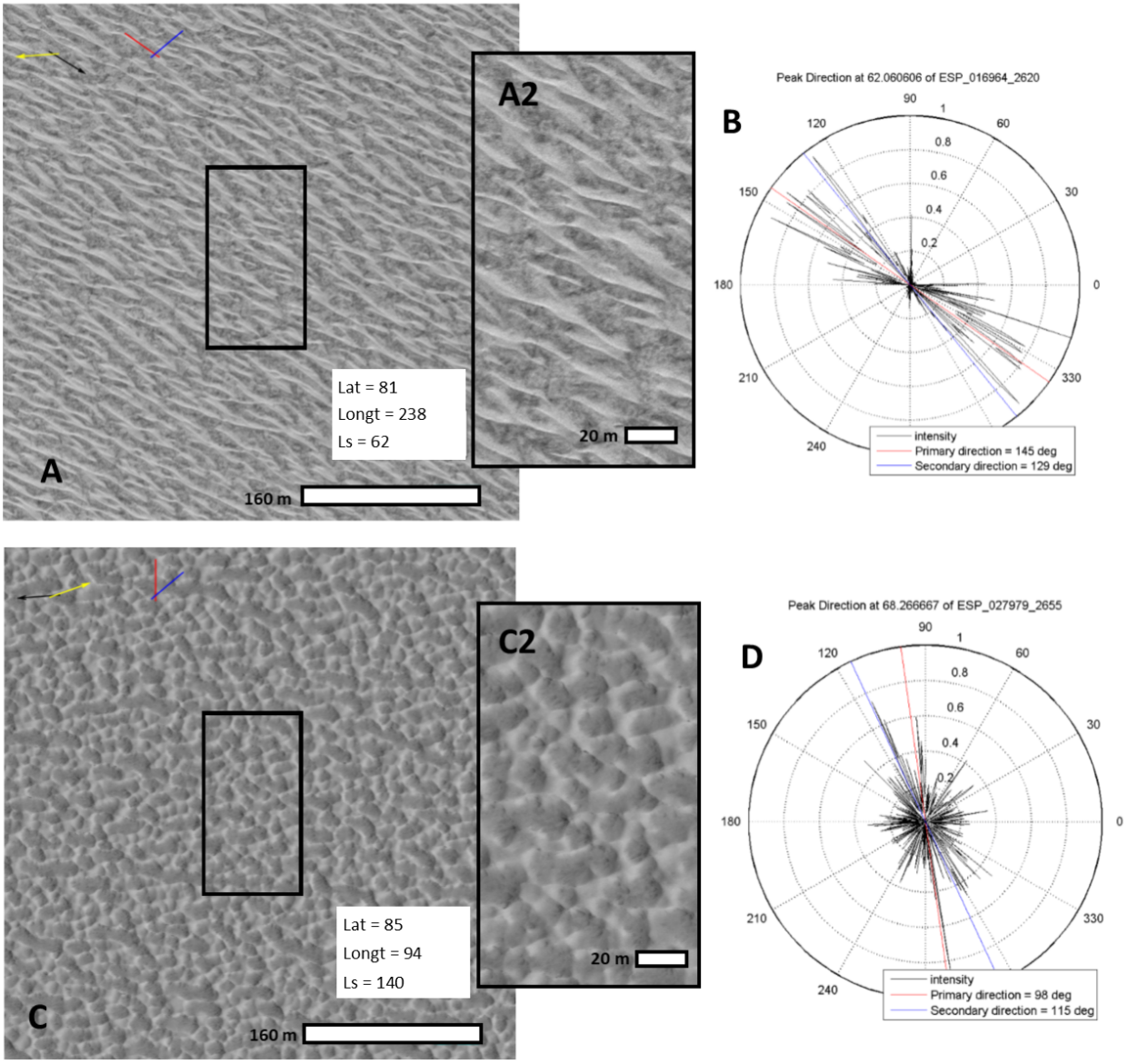

Figure 2.8: Panel A-B shows high confidence in orientation represented by HiRISE image ESP_016964_2620. Panel A and A2 show the frame extracted and its magnification. Panel B shows the power with respect to direction at the frequency with the biggest power difference peak. Panel C-D shows low confidence in orientation represented by HiRISE image ESP_027979_2655.

2.1.2 Comparison with the Variogram Method

While spectral analysis with the FFT is preferred due to being native to MATLAB, the variogram is a more direct approach. Implementing the Welch window, transforming the image into frequency space, and comparing with simulated noise is not necessary when measuring the spacing and orientation of cyclic patterns. Brightness patterns of pixels behaving like waves will produce low variance between pixels that have the corresponding wavelength. Similar to the FFT, variance at specific wavelengths can be broken up into different directions giving information on the propagation orientation of the waves. The variance between pixels at a distance d can be calculated with the following equation:

$$\sigma(d) = \frac{1}{N(d)} \sum_{i,j=1}^{N(d)} (x_i - x_j)^2 \tag{2.1}$$

x denotes the pixel brightness, i and j are the indexes for the position of the pixels, and N is the number of pairs that share distance d within the image. The process for using the variance to measure spacing and orientation using a sample image (figure 2.9) is as follows:

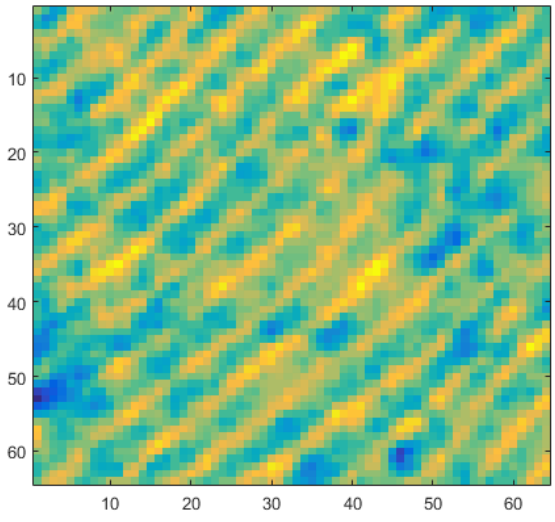

Figure 2.9: sample image with size 64×64 pixels

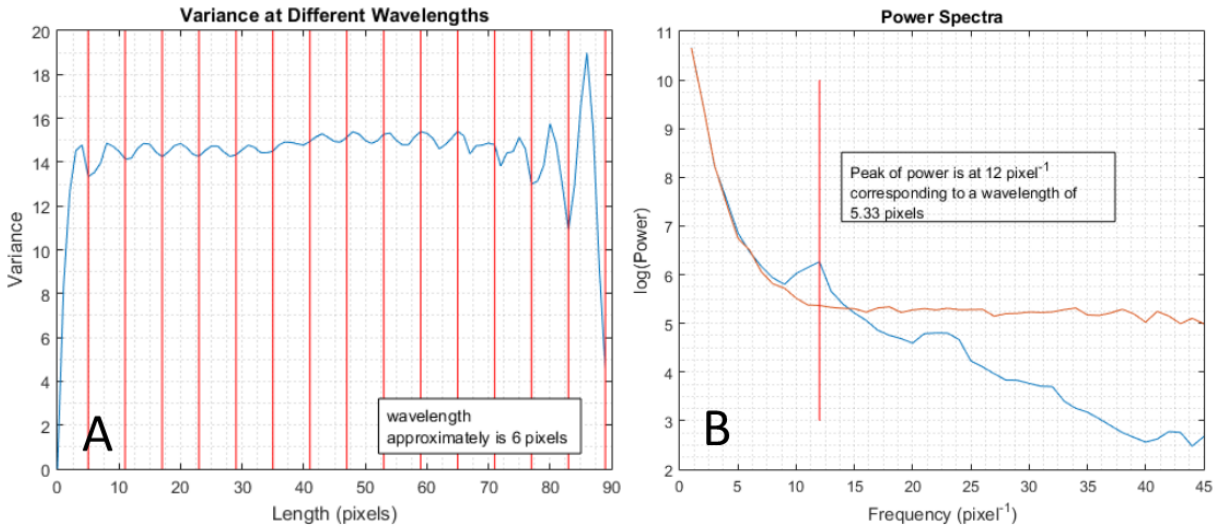

Figure 2.10: Panel A shows the variance of brightness where the first few dips are spaced 6 pixels apart. The red lines signify the wavelength spacing of 6 pixels to identify possible wavelike behaviours. Panel B shows the standard FFT where the blue line is the power spectrum of the actual image and the orange line is the randomly generated image. The red line on panel B also denotes the peak found which corresponds to a wavelength of 5.33 pixels.

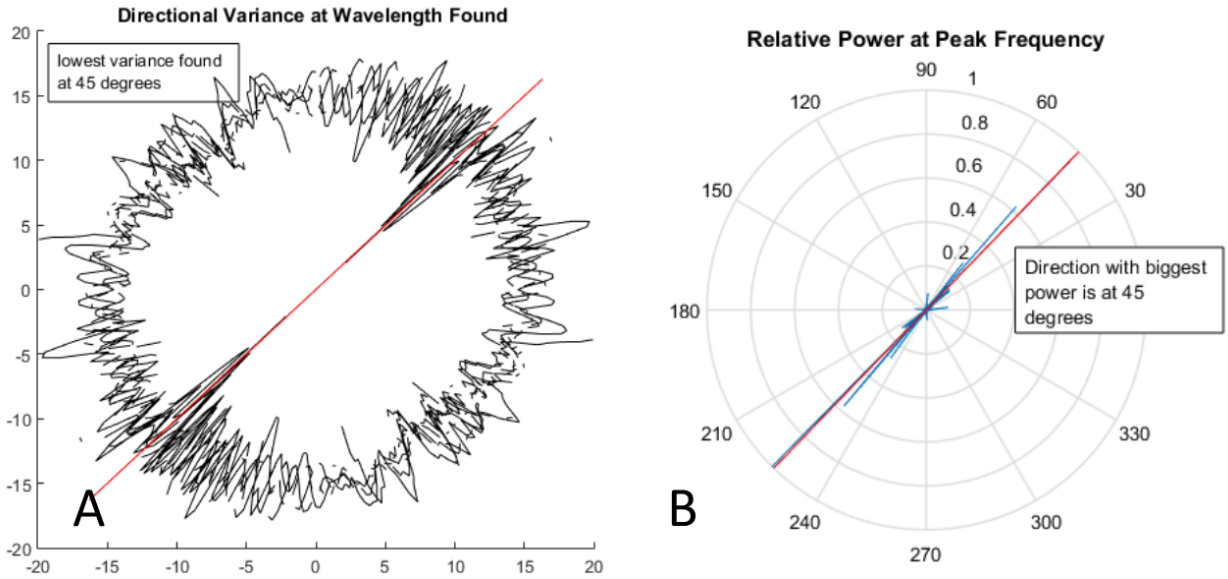

Figure 2.11: Panel A shows the variance in brightness at each dip taking into account multiples of wavelengths of 6 pixels. The red line denotes the lowest value in variance of the dips at 46 degrees with respect to the horizontal. Panel B shows the power at the peak wavelength of 5.33 pixels in different directions where the red line identifies the highest peak at 46 degrees above the horizontal.

Figure 2.10 shows the spacing inferred between both methods and figure 2.11 shows the orientation. As opposed to the FFT where the power peaks are identified, the variance method relies on tracking the variance dips. While both methods produce similar results that correspond to easily identifiable features on the image, the FFT is preferred as it is already native to MATLAB. If the variogram is produced from just the variance equation (eq. 2.1), the lack of optimization can lead to a heavy computational load. By making sure no calculation is repeated when comparing different pixels, the variogram method can be quite successful in measuring spatial and orientation tendencies of HiRISE data.

However, problems may arise when using a systematic approach. When the spacing or wavelength of a feature is inferred, the variogram will also tend to show dips in variance at multiples of the inferred wavelength. For example, if the inferred spacing of a feature is 6 m, then the variogram will also show dips at wavelengths of 12 m, 18 m, 24 m... This may be troublesome when using an automated process of finding the most prevalent wavelength within a pattern as the wavelength found may not be representative of the feature analyzed. Referring to panel A of figure 2.10, simply finding the lowest dip in variance (not including the edges) will lead to an inferred spacing of 84 pixels. However, upon visual inspection, the features of interest are spaced 6 pixels apart and the inferred spacing of 84 pixels is actually 14 multiples of the 6-pixel wavelengths. This could be remedied by having a smaller range of wavelengths to infer the spacing but that ultimately requires some prior knowledge of the features analyzed which can be problematic for surveying unfamiliar terrain.

2.2 Simulating Penitentes on Mars

This section will detail the necessary steps needed for modeling growth of penitentes on the surface of Mars. Using a water ice surface, Martian conditions such as its orbit and its dusty atmosphere are considered to check for possible sublimation-driven pattern's tendency.

Like Cathles et al. (2014) and Moores et al. (2017), orientation tendencies of penitentes are determined by simulating incoming solar radiation at a specified geographical location within the polar region. The sun-path throughout the day is calculated where each day is spread out on small intervals of Ls. The sun location on the Martian sky, defined by azimuthal direction and zenith angle, is calculated from the Mars24 algorithm implemented by Allison and McEwen (2000). With significant dust in the atmosphere, scattering of the incoming solar radiation is calculated from the model used by Moores et al. (2017) when calculating incoming UV fluxes. The scattering model will provide a gridded sky with varying solar radiation coming in from each grid point. The flux absorbed and reflected by the surface is then calculated.

The incoming flux F_{tot} is calculated from the radiance R_a of the sun as seen from Mars (Andrews, 2010). The flux F_{tot} is then calculated in equation 2.2 where radiance going through a surface times the dot product between the surface normal $\vec{n_r}$ and a direction vector $\vec{r}$ is integrated with respect to the solid angle s covering half of the hemisphere. From each point in the sky with varying solar flux due to scattering, the projected flux is calculated via equation 2.4 (Moores et al., 2017). To actually find the orientation, the surface is rotated so that all the directions are considered when calculating the received insolation; the projection of the insolation on the rotating surface is given by equation 2.4 and 2.5 (Cathles et al. 2014).

$$F_{tot} = \int_{2\pi} R_a \vec{n_r} \cdot \vec{r}.ds(\vec{r}) \tag{2.2}$$

$$F_{rec} = F_{tot} \frac{-\vec{F}_{dir} \cdot \hat{n}}{|F_{dir}|} \tag{2.3}$$

$$F_{proj} = F_{tot} \sqrt{cos\theta_Z^2 + (sin\theta_Z cos\phi)^2} \tag{2.4}$$

$$\theta_{proj} = tan^{-1}\left(\frac{cos\theta_Z}{sin\theta_Z cos\phi}\right) \tag{2.5}$$

In equation 2.3, F_{rec} is the flux received by the surface per unit area, F_{tot} is the magnitude of the flux, $\vec{F}_{dir}$ is the solar flux vector, and $\hat{n}$ is the normal unit vector of the surface. In equation 2.4, F_{proj} is the projected flux onto the plane of the rotating surface, θ_Z is the solar zenith angle, and ϕ is the azimuthal angle. In equation 2.5, θ_{proj} is the projected zenith angle onto the plane, θ_Z and ϕ are the same as in equation 2.4. Figure 2.12 shows the geometry of equation 2.3.

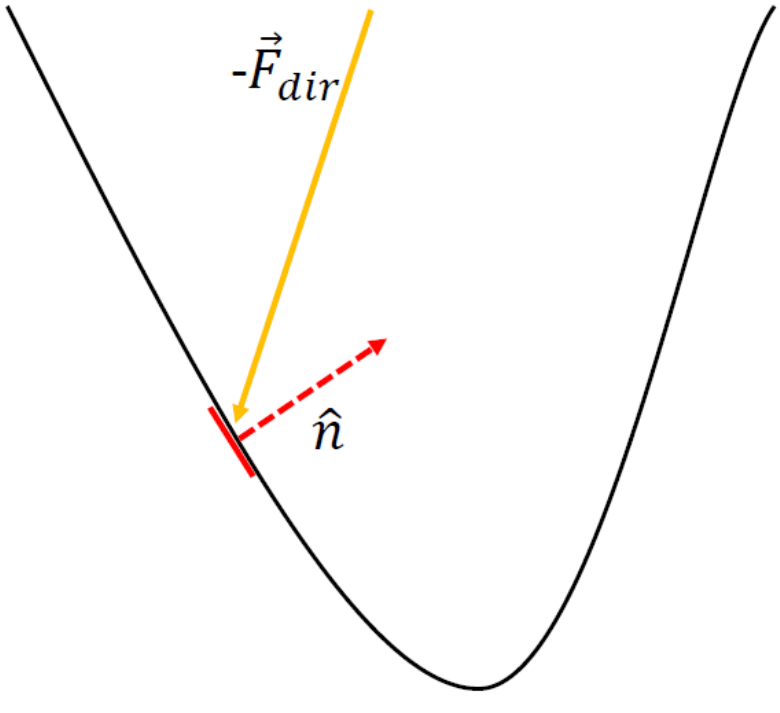

s

Figure 2.12: The figure shows incoming flux (coloured orange) coming into contact with a portion of the surface (coloured red).

The surface is taken to be a parabola specified by width and depth. The surface rotates along the vertical axis with matrix 2.6 where ω is the counter-clockwise rotation and a vertical tilt for the parabola centre can be taken into consideration. Upon receiving the incoming flux, part of the flux is absorbed but the other part defined by the albedo will be

reflected outward where other parts of the surface can receive this reflected flux. Throughout the day, each grid point on the surface will accumulate incoming flux which is then added with other days in order to get a full look throughout the year. By seeing which orientation favours the concentration of insolation towards the centre of the parabola, it is possible to see if penitentes can form on the NPLD and the orientation in which it is likely to occur.

$$C(w) = \begin{bmatrix} cos\omega & -sin\omega \\ sin\omega & cos\omega \end{bmatrix} \tag{2.6}$$

The spacing of the penitentes $(1/k)$ can be determined from the calculations of its growth rate given by equation 2.7 (Claudin et al., 2015; Moores et al., 2017):

$$\frac{\rho_s \mathcal{L}}{\Psi_a}\sigma = \frac{k\Lambda}{1 + \mathcal{P}tanh(kl) + \mathcal{R}k\Lambda} \times \left[\left(1 - \frac{1}{\sqrt{1+k^2\Lambda^2}}\right) + \Omega\left(1 - \frac{k\Lambda}{\sqrt{1+k^2\Lambda^2}}\right) - \left(1 - \frac{1}{cosh(kl)}\right)\mathcal{P}\right] \tag{2.7}$$

$$\mathcal{P} = \frac{\kappa_s}{\rho'_{sat} D_\rho \mathcal{L}} \tag{2.8}$$

$$\mathcal{R} = \frac{\kappa_s}{\rho'_{sat} \alpha \Lambda \mathcal{L}} \tag{2.9}$$

In equation 2.7, σ is the penitente surface deepening rate, ρ_s is the density of the subliming solid, $\mathcal{L}$ is the latent heat of sublimation, Ψ_a is the volumetric heat deposition, Λ is the exponential constant of light penetration onto the sublimating solid, k is the wavenumber of the penitente structure, l is the mixing length scale away from the surface, $\mathcal{R}$ is the kinetics of sublimation constant calculated via equation 2.8, $\mathcal{P}$ is the mass diffusion constant calculated via equation 2.9, and Ω is the phase velocity defined by ω/k.

In equation 2.8 and 2.9, κ_s is the thermal conductivity of the sublimating solid, ρ'_{sat} is the first derivative of the saturation vapour density, D_ρ is the sublimating vapour diffusivity, and α is the kinetic constant of sublimation. The next step is to numerically solve for k_m to maximize the penitente growth rate σ which will lead to the most unstable wavelength $\lambda_m = 2\pi/k_m$.

Given volatile materials (H_2O and CO_2) on Mars, this model can also be tested for carbon dioxide. Using the Cathles et al. (2014) method, it is possible to see if Martian penitentes are as restricted geographically as they are on earth and what their orientation tendencies are. Using the model of Claudin et al. (2015), it is also possible to determine the most likely spacing of penitentes. Should their formation be possible within reasonable parameters, comparisons with actual HiRISE data can be made to identify sublimation-driven surface features on Mars.

2.2.1 Finding the Preferred Orientation

Penitentes sizing and orientation preferences are modeled using equations 2.3 to 2.9. When modeling the orientation, a parabolic contour is created representing the cross-section of a penitente feature. The size of the parabola is arbitrary where the width ranges from 2-10 m and the depth is 2 m with a surface resolution of 5 cm. The size of the surface contour is arbitrary as internal reflection within a concave surface depression promoting penitente formation can occur at any scale (Claudin et al., 2015). The surface then undergoes flux absorption for a full day where the surface will rotate 10° counter-clockwise from an initial east-west orientation. This is done for every 10 Ls where specific time period for penitente growth can then be found. A tilt is also applied to the parabolic surface to see the effects of inclination which is important for high-latitude regions; the latitudes used for the simulations are 70° and 80°. Favourable illumination for penitentes maintenance is defined as higher average flux received or higher energy absorption in the bottom third of the feature's depth

compared to the sides or the upper $2/3^{rd}$. The surface albedo used ranges from 0.2 to 0.5 corresponding to the albedo range of the summertime's polar cap measured by the Viking Infrared Thermal Mapper (Bass et al., 2000). The process for finding favourable orientation of the features are thoroughly described in figures 2.13 and 2.14.

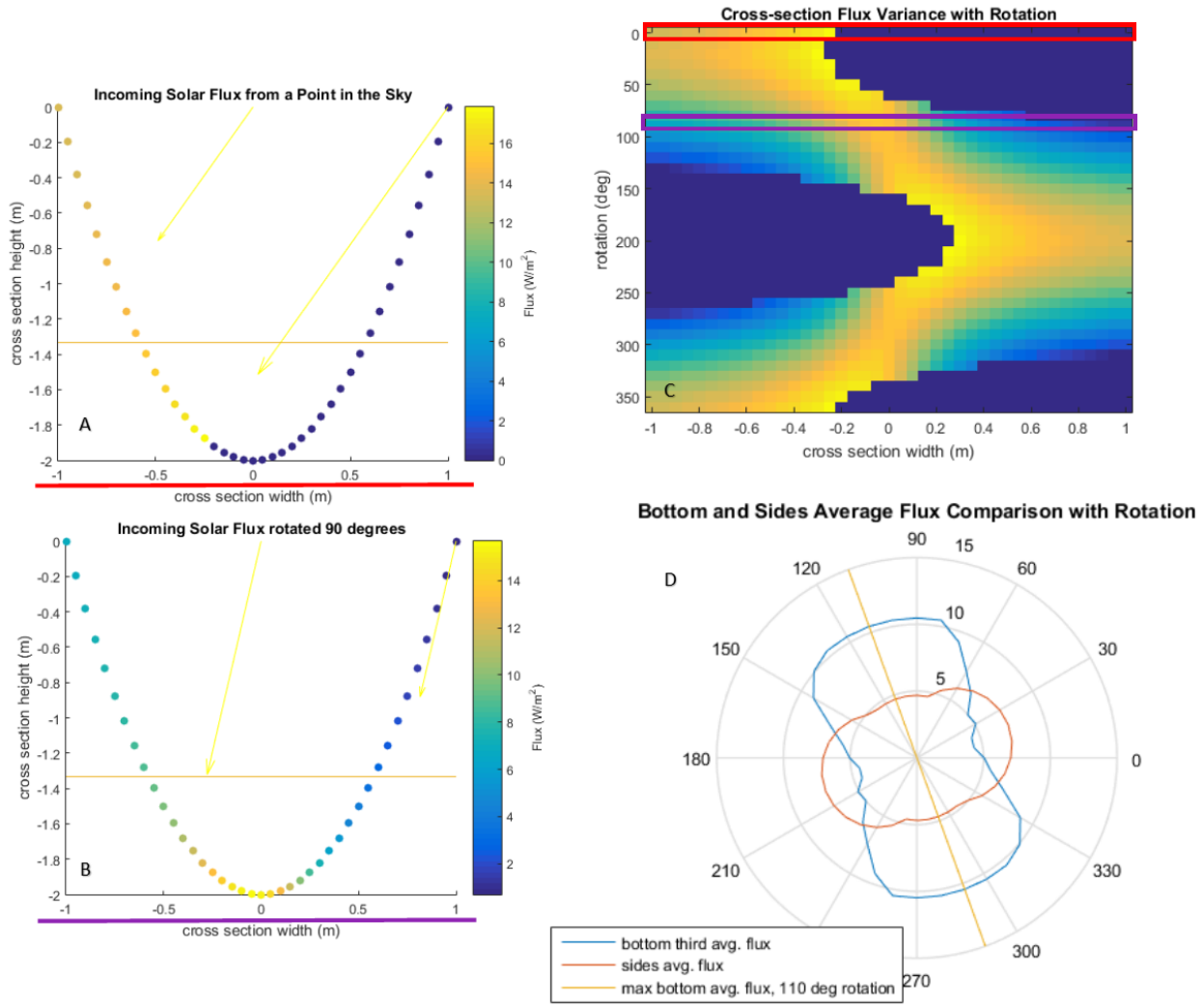

Figure 2.13: Panel A shows the cross-section at the initial trough orientation on the east-west axis. The right wall is the northern wall while the left wall is the southern wall. The yellow arrows represent the incoming flux from a sample point in the sky. The orange horizontal line represents the bottom third depth. Panel B is the same cross-section surface as panel A but is now rotated 90 degrees. Panel C shows the top-down view of the flux absorbed by the cross-section surface as the surface is rotated. The red rectangle is the surface contour in panel A while the purple rectangle is the surface of panel B. Panel D shows the average flux absorbed by the surface below the bottom third depth as well as the side surfaces as the cross-section is rotated. For this example, the bottom third of the surface receives the most flux when the contour is rotated 110°.

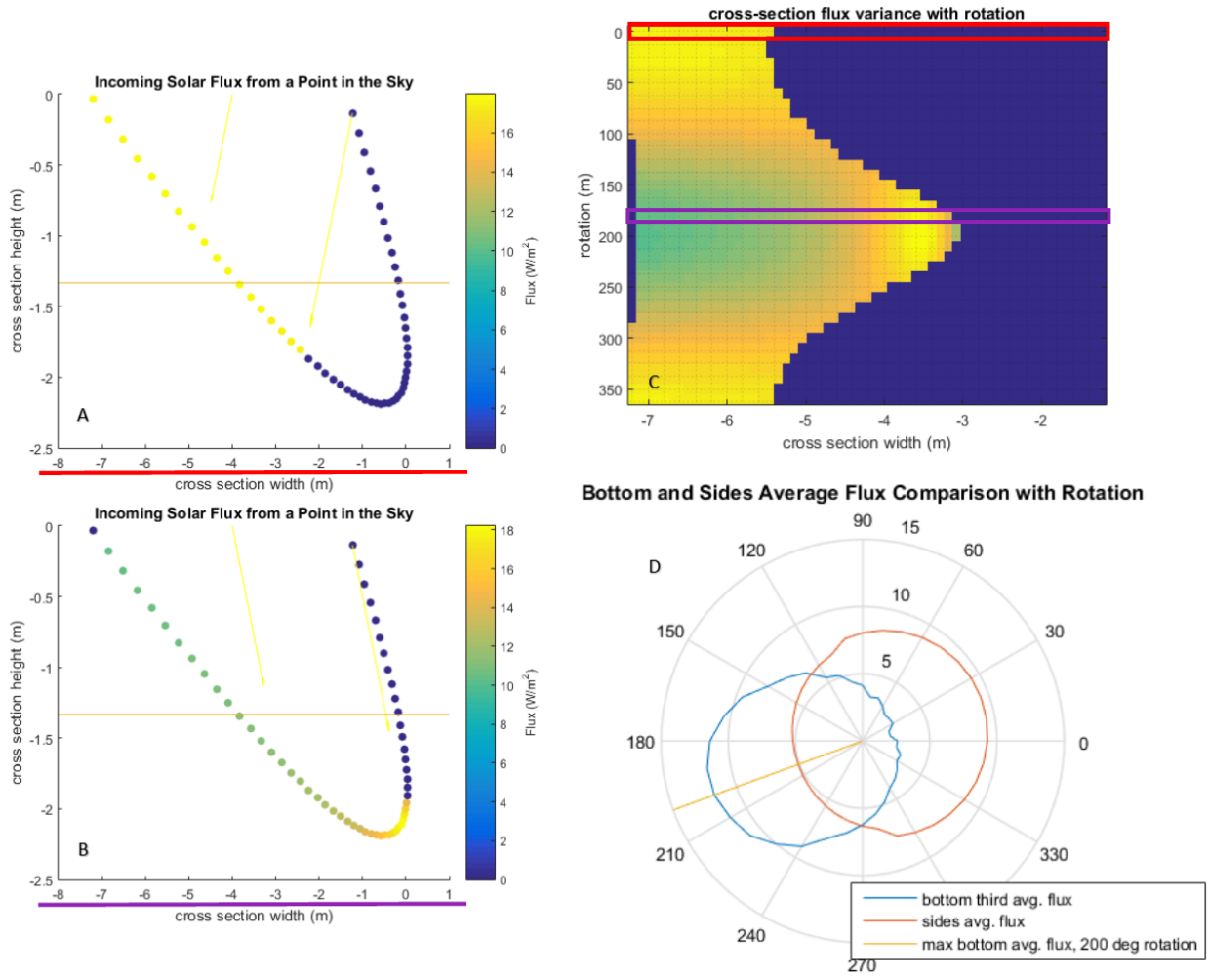

Figure 2.14: This figure follows the exact same format as figure 2.13. The sample flux and its incoming direction is also the same. The surface contour, however, underwent a 60 degrees rotational matrix to induce a tilt which creates asymmetry when considering the average fluxes with respect to rotation; this can be seen in panel D.

The internal reflection from incoming solar flux is treated as Lambertian reflectance such that reflected flux from the surface will radiate outward in all directions. The energy absorbed from reflected flux at point A to point B on the surface is given by equation 2.10. In equation 2.10, $E_{rec,B}$ is the energy received at point B from the reflected flux from a point A, $F_{rfl,A}$ is the reflected flux from point A given by $(1-a)F_{rec}$ from equation 2.3, $area_A$ is the area of the gridded surface of point A, $\hat{n}_B$ is the normal vector of the surface at point B. a is the albedo of the surface. Figure 2.15 shows the energy absorbed from a point reflecting an arbitrary value of flux.

$$E_{rec,B} = \frac{F_{rfl,A}(area_A)}{2\pi|\overrightarrow{AB}|}\hat{AB} \cdot \hat{n}_B \tag{2.10}$$

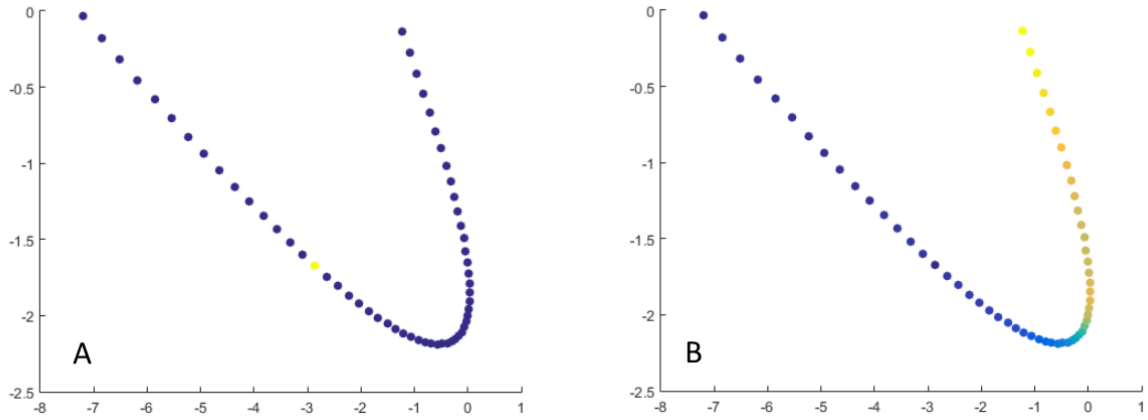

Figure 2.15: Panel A shows the flux reflected from a point where panel B shows the energy absorbed from the reflected flux of the point from Panel A

2.2.2 Finding the Preferred Size

The preferred size is given by maximizing the left hand side of the equation 2.7. Values for water ice properties are: $\mathcal{L} = 3 * 10^6$ J/kg, $\Lambda = 0.016$ m, $\kappa_s = 2$ W/m/K, and $\alpha = 1$ m/s (Claudin et al., 2015). Vapour diffusivity is taken from Hudson et al. (2007) where $D_\rho \simeq 4 * 10^{-4}\ m^2/s$. The mixing length l is given by equation 2.11 (Moores et al., 2017).

$$l \simeq \frac{5\mu}{\rho u_*} \tag{2.11}$$

In equation 2.11, the Martian atmosphere is treated as 100% CO_2 where the dynamic viscosity μ is calculated to be roughly $1 * 10^{-5}$ Ns/m^2 at 203 K (Crane 1988). The density ρ is calculated from the ideal gas law $P = \rho R_* T / M_{CO_2}$ where P is taken to be 600 Pa, the gas constant R_* is 8.3 J/K/mol, M_{CO_2} is the molar mass of $44 * 10^{-3}$ kg/mol, and T is taken to be 203 K making $\rho = 1.57 * 10^{-2}$ kg/m^3 . u_* is the frictional velocity which is different for turbulent flow or viscous flow.

An important term useful for distinguishing between different flow regime is the Reynolds number given by equation 2.12. In the equation, u is the general flow taken to be 10 m/s, l_c is the characteristic length taken to be 20 m to make it consistent with the small scale features found, ρ_{CO_2} is the density of CO_2 taken at a pressure of 6 mb and a temperature of 203 K, and μ_{CO2} is the kinematic viscosity from Crane (1988). Using these parameters will yield a Reynolds number of approximately $3 * 10^6$. With such a high Reynolds number, the flow is turbulent and the frictional velocity of $u_* = 0.4m/s$ for a Martian convective mixed layer is used (Petrosyan et al., 2011). If the flow is laminar somehow, u_* can be calculated in equation 2.13 from Ingersol et al. (1985).

$$R_e = \frac{u l_c \rho_{CO_2}}{\mu_{CO_2}} \tag{2.12}$$

$$u_* = \sqrt{\frac{\mu u 2}{\rho H}} \tag{2.13}$$

In equation 2.13, u is the general flow which is assumed to be approximately 10 m/s, and H is the scale height estimated to be $11 * 10^3$ m (Petrosyan et al., 2011). With these values, the frictional velocity u_* is calculated to be $1.09 * 10^{-3}$ m/s which yields a mixing length l

of 3 m. The equation is dependent on the scaled height factor of H/2 as we assume that the flow does not vary significantly vertically within the boundary layer; this allows for an easier calculation of u_* where u can be taken as an average velocity representative of the boundary layer and is useful for thin atmospheres (Ingersol et al., 1985)

The first derivative of the saturated vapour density ρ'_{sat} is calculated by equation 2.14 (Moores et al. 2017; Claudin et al. 2015). The molar mass of water M_{H_2O} is $18 * 10^{-3}$ kg/mol, the saturated vapour density is calculated from the ideal gas equation where the pressure used is the saturated vapour pressure P_s calculated from Goff Gratch equation 2.15 of water vapour over ice (Smithsonian, 1984).

$$\rho'_{sat} = \frac{\rho_{sat}}{T}\left(\frac{M_{H_2O}\mathcal{L}}{R_* T} - 1\right) \tag{2.14}$$

$$log_{10}P_s = -9.09718\left(\frac{273.16}{T} - 1\right) - 3.56654 log_{10}\left(\frac{273.16}{T}\right) + 0.876793\left(1 - \frac{T}{273.16}\right) + log_{10}(6.1071) \tag{2.15}$$

Equation 2.15 has input of T in [K] and the output of P_s in [hPa]. At 203 K, P_s is calculated to be 0.26 Pa which leads to a saturated vapour density ρ_s of $2.7 * 10^{-6}$ kg/m^3. Using these values for equation 2.14 yields ρ'_{sat} to be $4.17 * 10^{-7}$ kg/m^3/K. The variables introduced and calculated in this subsection are then used in equation 2.7 at a sample k value to find the growth rate.

Chapter 3

Results

3.1 Surface Features Observed

A total of 499 HiRISE images were found to have noteworthy surface features resulting in 559 extracted frames. Of these 559 frames, 405 frames have a high confidence value in spacing. 423 frames have a high confidence value in orientation tendency. 78 frames have both a low confidence in spacing and orientation. The mapping of all features found are shown in figure 3.1. When separating the frames into different types, the groupings of morphologically similar frames along with superficial details of the groups is summarized in table 3.1.

Frames containing surface patterns that have morphological characteristics of aeolian-driven features account for 69% of all the frames analyzed. The grouping types of these frames are transverse dunes, ripples, star dunes and TARs. Transverse dunes are observed the most with 26% of the observations. Uncategorized features account for 20% of all the frames, making them the second most abundant features. Some of the features in the group may exhibit patterns that suggest aeolian processes have taken place but the patterns are not consistent throughout the frame enough to draw any meaningful conclusions. 48% of

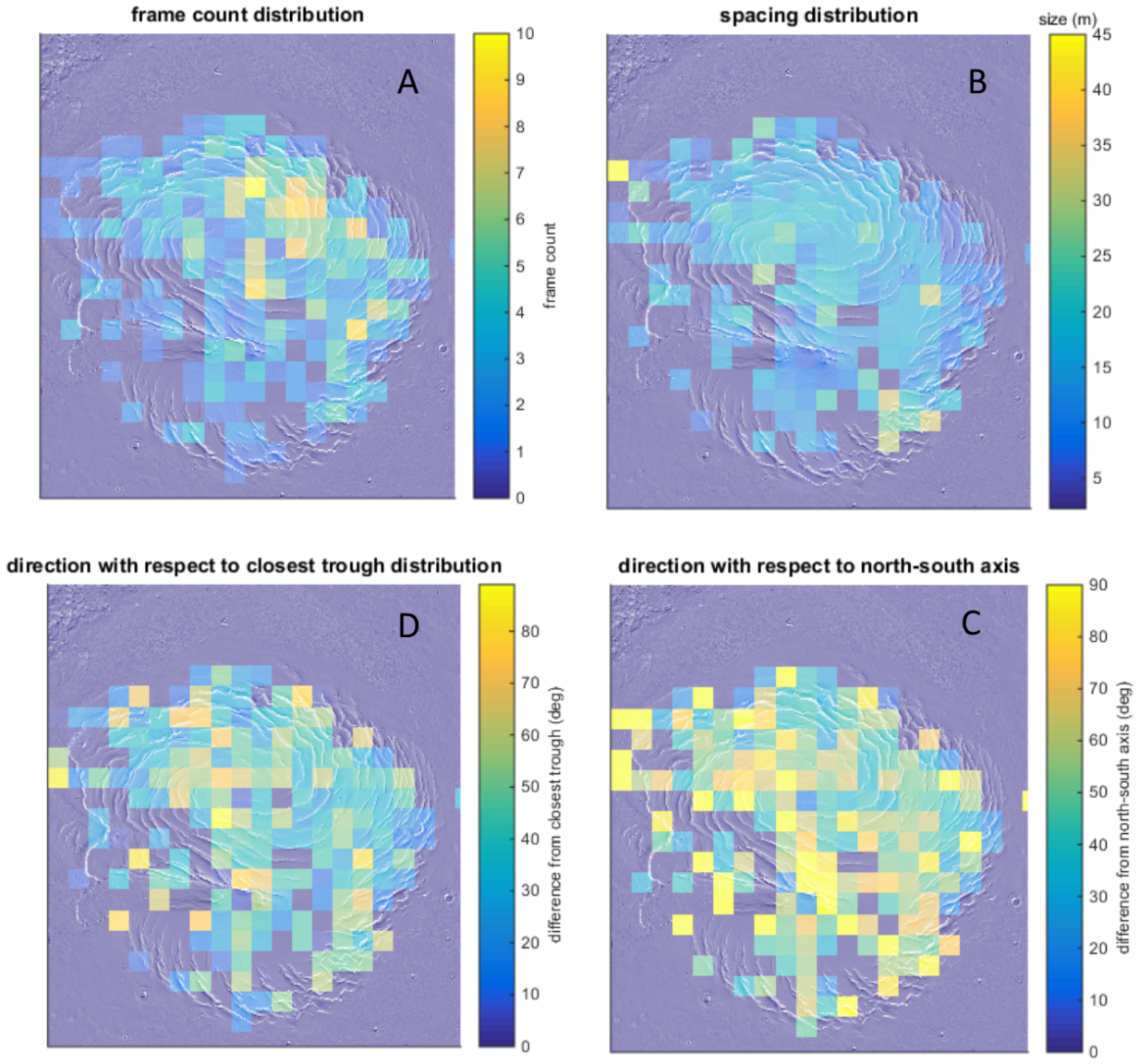

Figure 3.1: Panel A maps the frame count for the entire dataset. Panel B maps spacing (m) for all frames. Panel C maps the direction (°) with respect to the closest troughs for all frames. Panel D maps the direction (°) with respect to the North-South axis for all frames. Each bin square is 1 degree latitude in length.

the uncategorized features have neither high confidence in spacing nor orientation. All the dunes and ripples are mapped in figure 3.2.

Table 3.1: Table shows the grouping type, the number of frames belonging to the groups, the averaged spacing inferred, the averaged orientation with respect to the North-South axis, and the distribution of confidence levels assigned to each analyzed frame

Types	Count	Ave. spacing (m)	Ave. orient. (°)	Count of conf. lvl. 5, 4, 3, 2, 1
transverse dunes	146	15.43	25.50	88, 8, 28, 18, 4
ripples	106	7.51	38.15	58, 40, 6, 1, 1
star dunes	58	16.05	40.36	23, 10, 3, 18, 4
TARs	77	16.85	34.91	47, 9, 12, 4, 5
pits	34	17.73	40.11	17, 3, 5, 6, 3
polygonal	15	22.51	46.44	0, 0, 2, 8, 5
"slits"	11	18.86	55.05	6, 0, 2, 1, 2
other/uncategorized	112	16.44	44.19	35, 3, 18, 2, 54

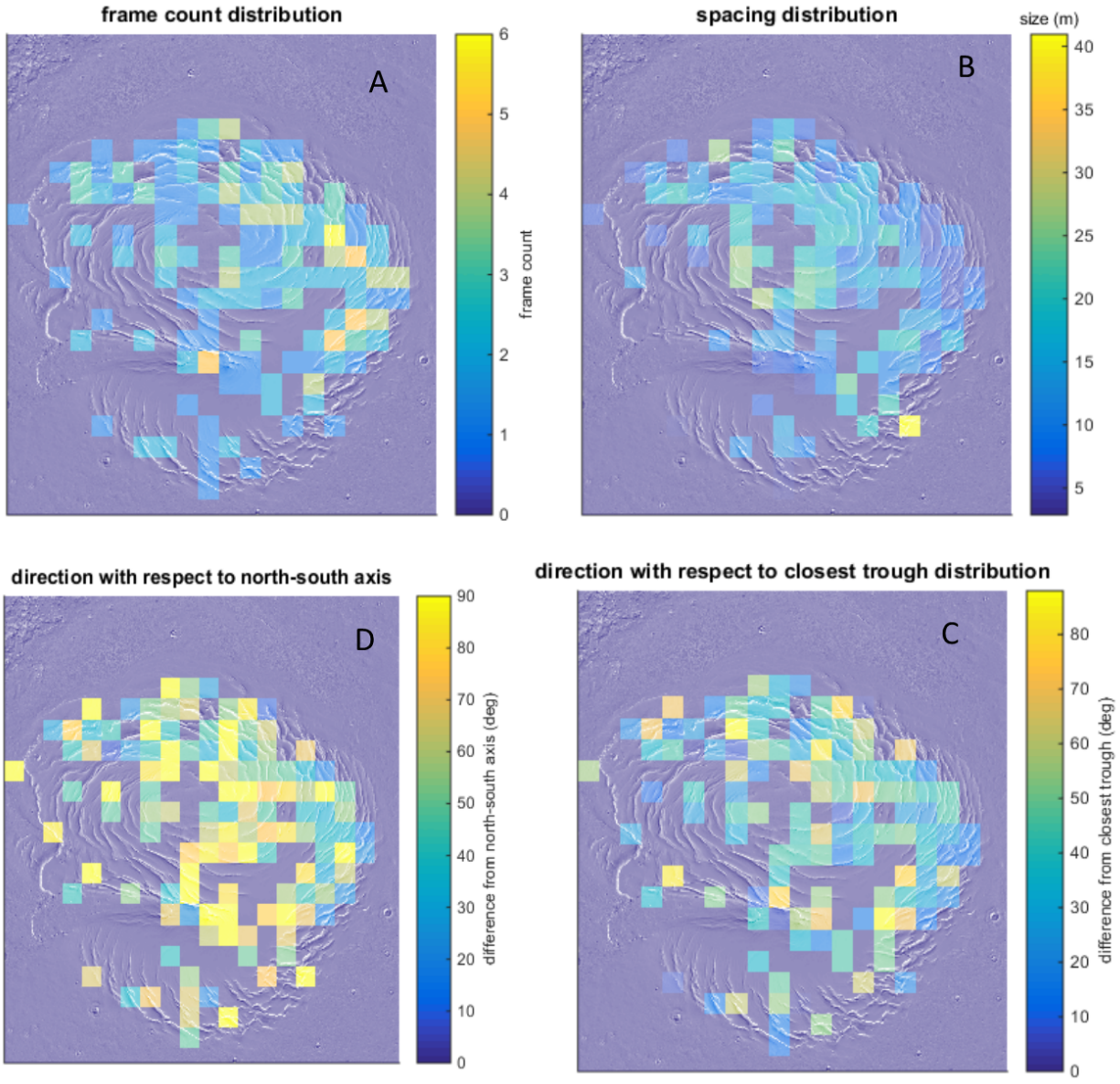

Figure 3.2: Panel A shows the mapping of all frames having ripple and dune-like features. Panel B shows the spacing (m) and panel C shows the orientation (°) with respect to the nearest trough. Panel D shows the direction (°) with respect to the north-south axis.

3.1.1 Ripples and Dunes

Although morphological differences between ripples and dunes are very difficult to distinguish, ripples are characterized here as being generally being smaller than 10 m. Their formation should still be perpendicular to the mean flow of aeolian transport but is more dependent on reptation than saltation (McKee, 1979). The mapping of all the ripples are shown in figure 3.3 and sample features are shown in figure 3.4. Ripples are the third biggest group after uncategorized. These features are very consistent in orientation and spacing as only 1 instance of these features have low confidence in orientation and spacing. Various ripple features are found to have changing directions when approaching and moving away from the nearby troughs. They are observed to align with the trough when they are near the trough but will become perpendicular to the trough when moving away. This is shown in figure 3.7.

Transverse dunes are the most dominant group with 146 recorded observation. Their formation should also be perpendicular with the mean flow for aeolian transport of materials. Their mapping is shown in figure 3.5 and sample features are shown in figure 3.6. Some of these features are similar to braided patterns characterized by Tsoar et al. (1979). This pattern seems to signify two perpendicular modes of wind direction and can be seen in panel C of figure 3.6. Other transverse dunes also have barchan like crescents perpendicular to their general longitudinal orientation which also suggests two perpendicular modes of wind flow. This can be seen in panel D of figure 3.6.

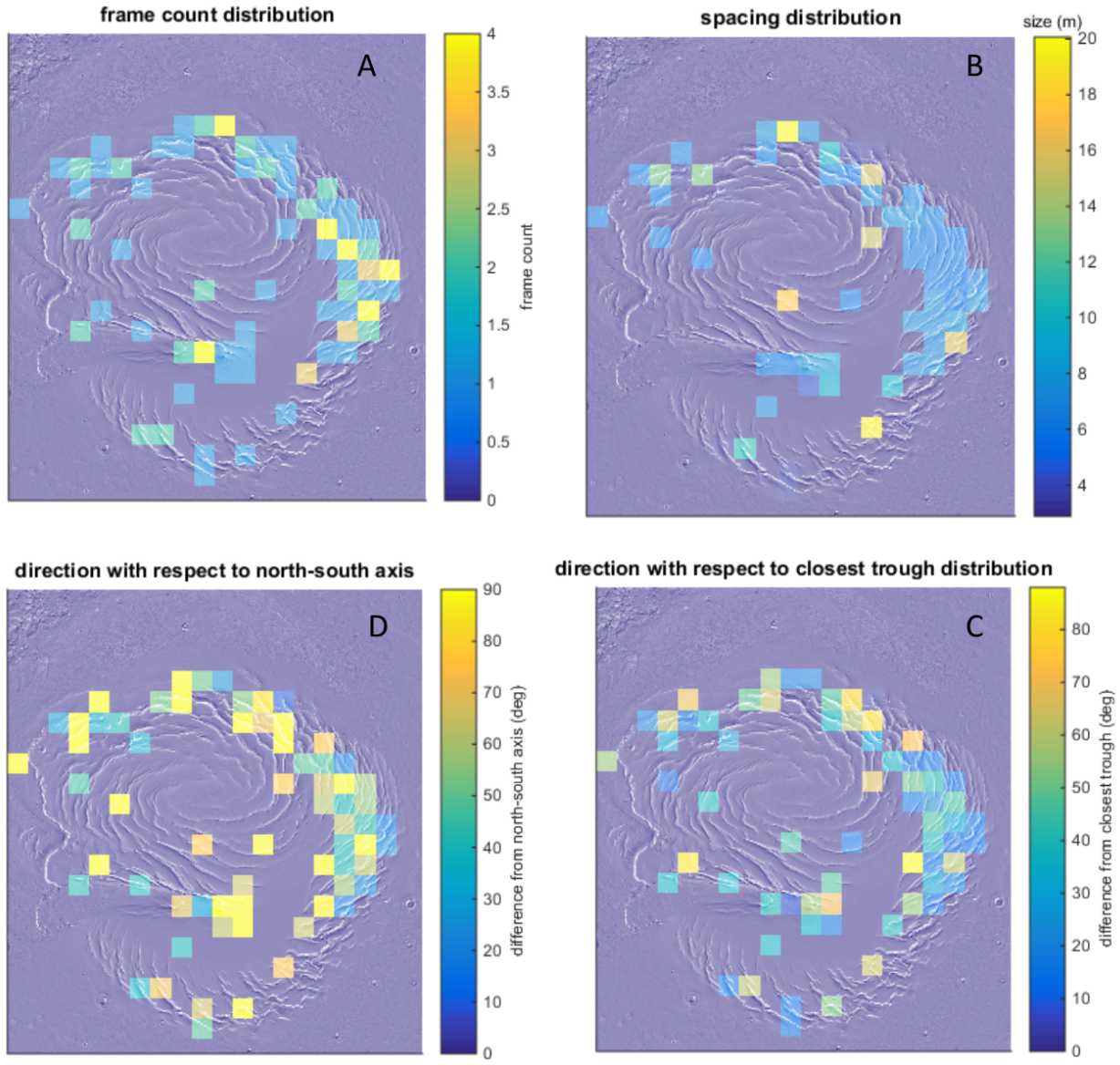

Figure 3.3: Panel A shows the mapping of all frames having ripple-like features. Panel B shows the spacing (m) and panel C shows the orientation (°) with respect to the nearest trough. Panel D shows the orientation (°) with respect to the north-south axis.

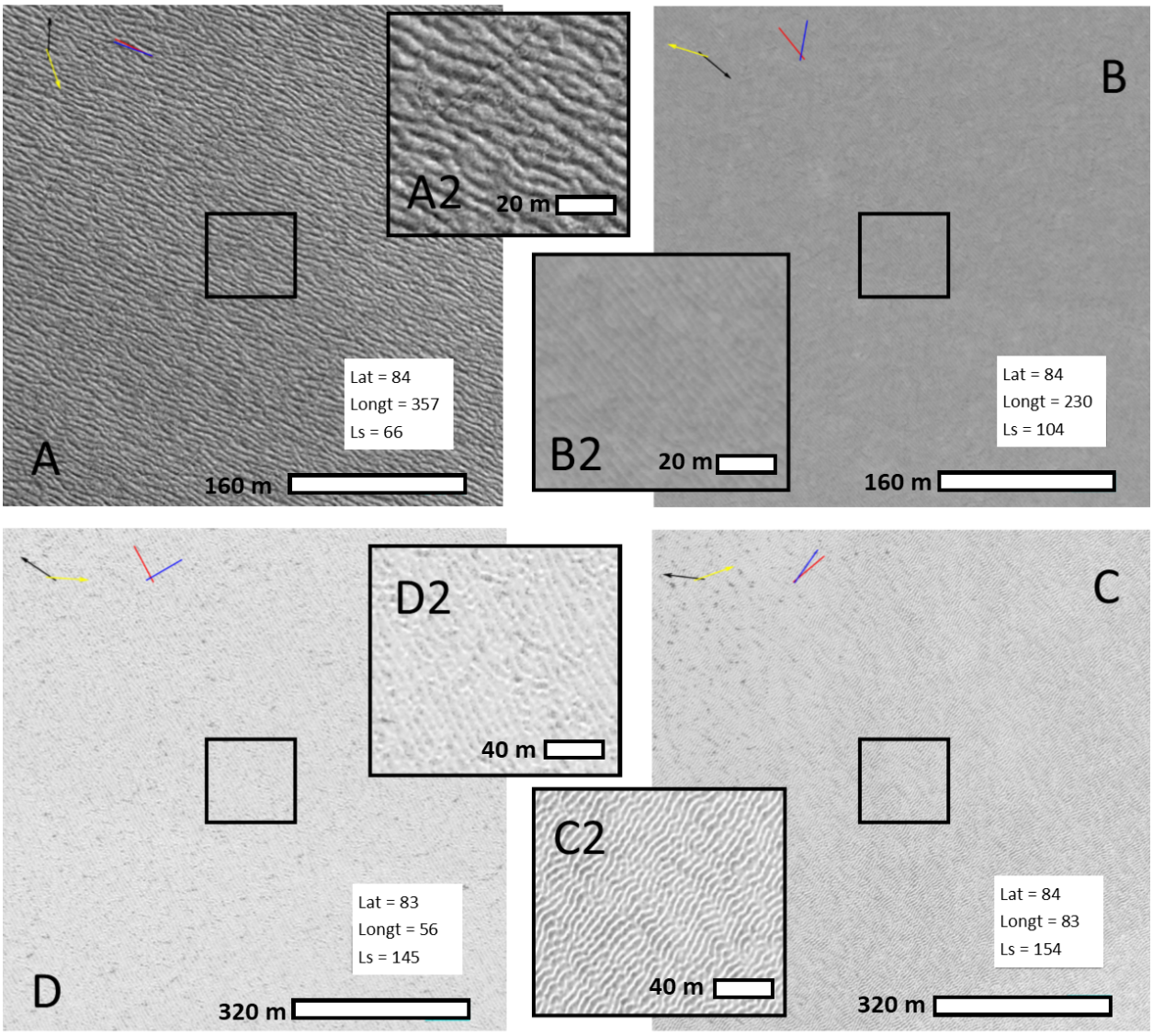

Figure 3.4: Panel A shows the frame ESP_017091_2645. Within the frame: the black arrow points to north, the yellow arrow points to the direction of the sun, the red line is the orientation tendency found through FFT analysis, the blue line is the orientation of the nearest trough, the scale is shown in the bottom right. All frames shown will follow this format. A2 is the magnification of the box in the centre of panel A. Panel B shows ESP_018190_2640. Panel C shows ESP_037144_2645. Panel D shows ESP_019291_2635.

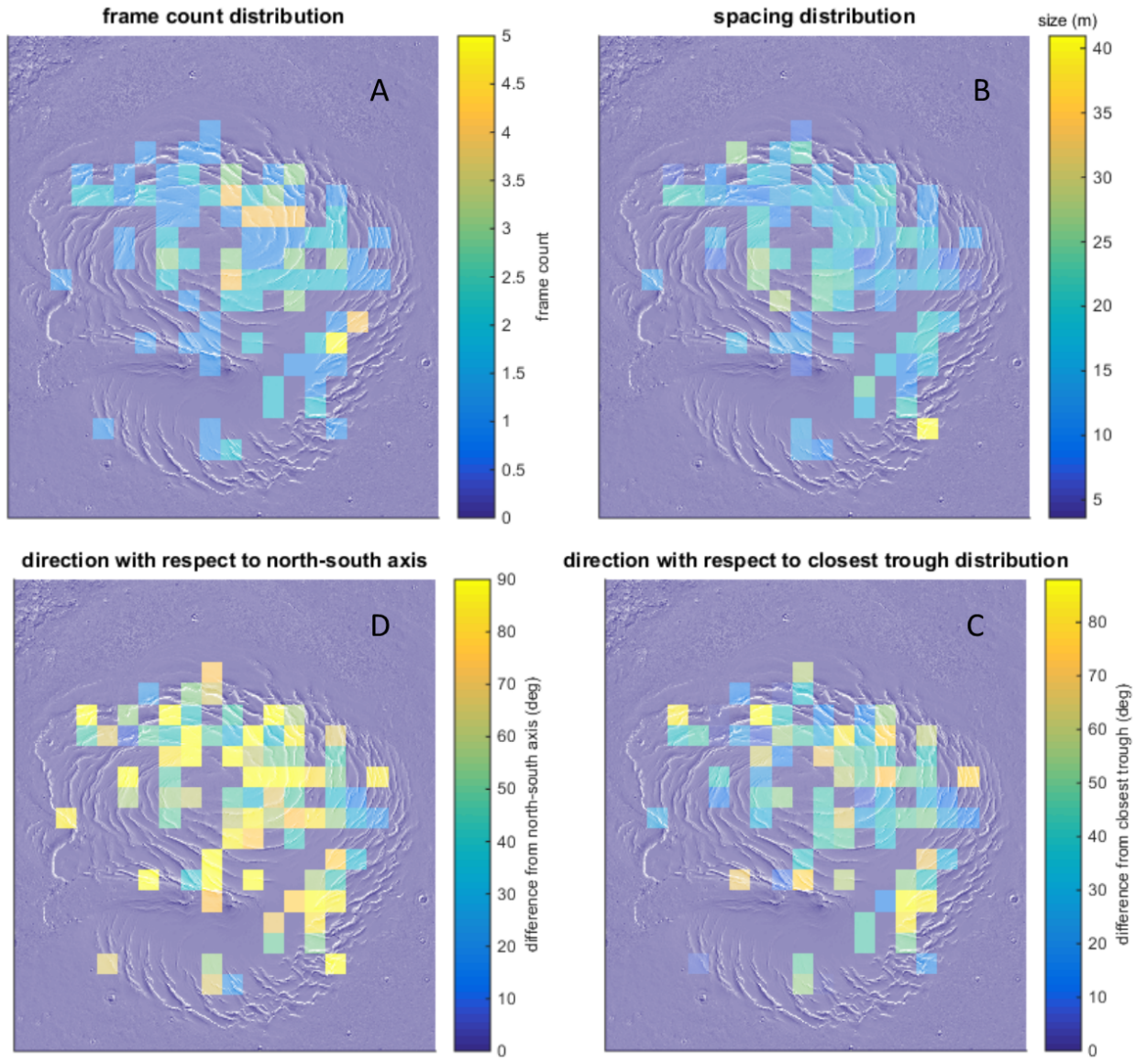

Figure 3.5: Panel A shows the mapping of all frames having transverse dune-like features. Panel B shows the spacing (m) and panel C shows the orientation (°) with respect to the nearest trough. Panel D shows the orientation (°) with respect to the north-south axis.

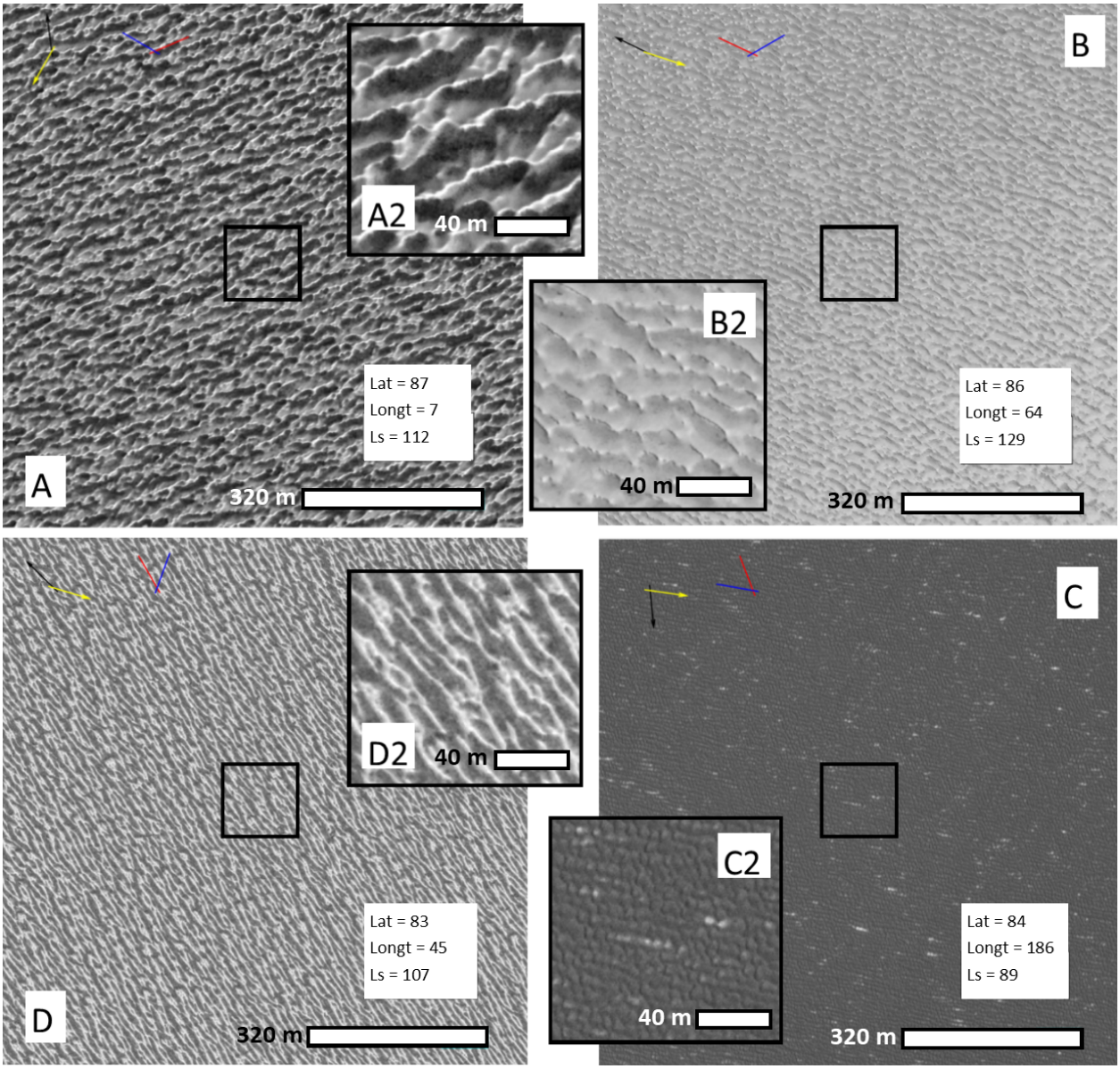

Figure 3.6: Panel A shows the frame ESP_018407_2675. A2 is the magnification of the box in the centre of panel A. Panel B shows ESP_018868_2665. Panel C shows ESP_017752_2750. Panel D shows ESP_018276_2635.

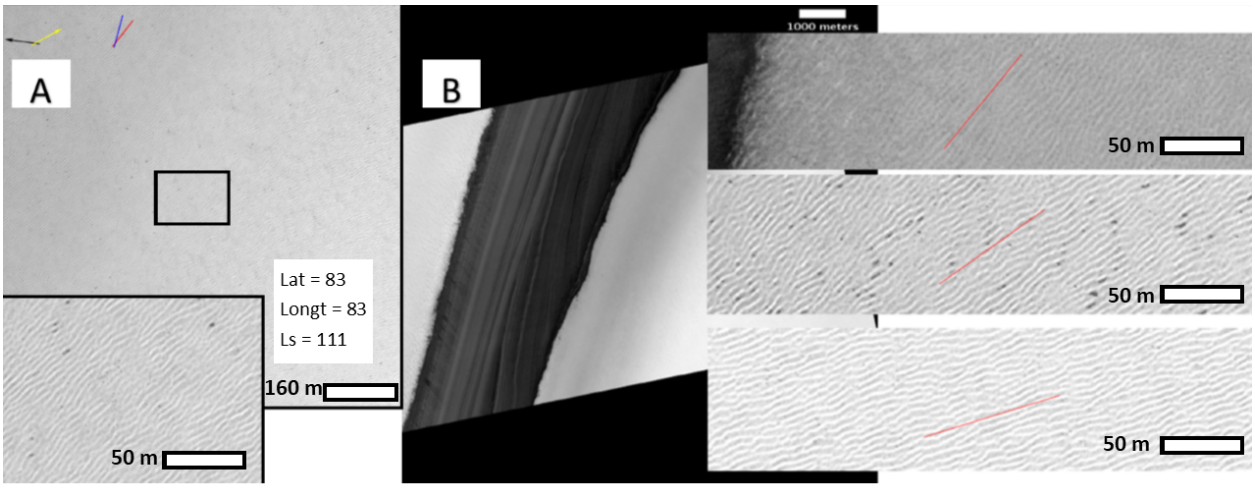

Figure 3.7: Panel A shows the frame extracted from PSP_009572_2630. Panel B shows the actual HiRISE image with smaller panels zooming in on various parts of the image. The smaller panels denote moving along the image to the right (south). It can be noted that the "fingerprint" pattern's orientation rotates clockwise as we move southward

3.1.2 TARs and other features

TARs belong to a small group occupying 14% of all the features observed. They can be split into 2 smaller subgroups: simple TARs (40 observations) and networked TARs (37 observations). Simple and unsaturated TARs are straight and have consistent orientation as no frames in that subgroup have a low confidence in orientation but 7 frames are found with low confidence in spacing. It is also important to note that the spacings measured are the distances between the features and not the widths of the feature themselves which are more useful for analyzing the dynamics of TARs done by Hugenholtz and Barchyn (2014).

Networked TARs, based on the classifications featured in Geissler (2014), are less consistent in orientation than simple TARs as 9 frames are found with low confidence in orientation. 9 frames are also found with low confidence in spacing. These features tend to have smaller bowl-shape depressions embedded within larger depressions where these bowl-shape features of different scales are usually perpendicular to one another. The mapping of all the TARs and sample frames can be found in figure 3.8.

Pits are classified as such for their round domes where their roundness is similar to the braided terrain. They are somewhat consistent in spacing and orientation as 59% of these features observed have both high confidence in spacing and orientation. The mapping along with sample frames can be found in figure 3.9.

Polygonal features or systems are patterns on the surface characterized by cracks stretching throughout the surface intercepting one another cutting out "polygons". The classification of these surfaces are based upon the works of Mangold (2005). These features have no tendency to orientate in any particular direction but their spacing is more consistent as 53% of the frames have high confidence in spacing. Their spacing is also the largest (average spacing of 22.51 m) of all the types of features observed. Sample frames can be found in figure 3.10.

"Slits" are called so because of their appearance resembling dark narrow openings on the ground. 73% of the features observed have high confidence in orientation but it should be noted that they are very rare as they only account for 2% of all the features observed. Sample frames can be found in figure 3.11. The "slits" can also be shadows cast by sharp crests which could imply an aeolian origin for these features. If this is the case, "slits" are likely to be barchans as opposed to transverse dunes since their longitudinal crests are not observed to be continuous.

There are instances of larger features (around 200 m), such as sastrugies, observed to have smaller features embedded within them. It is not overwhelmingly evident whether these smaller features are aeolian-driven. They are often grouped as "slits" or uncategorized but tend to be very consistent in orientation that is distinctly different from the larger features. This phenomenon is typically found in the Gemina Lingula which has a relatively scarce amount of HiRISE images. Examples can be found in figure 3.12.

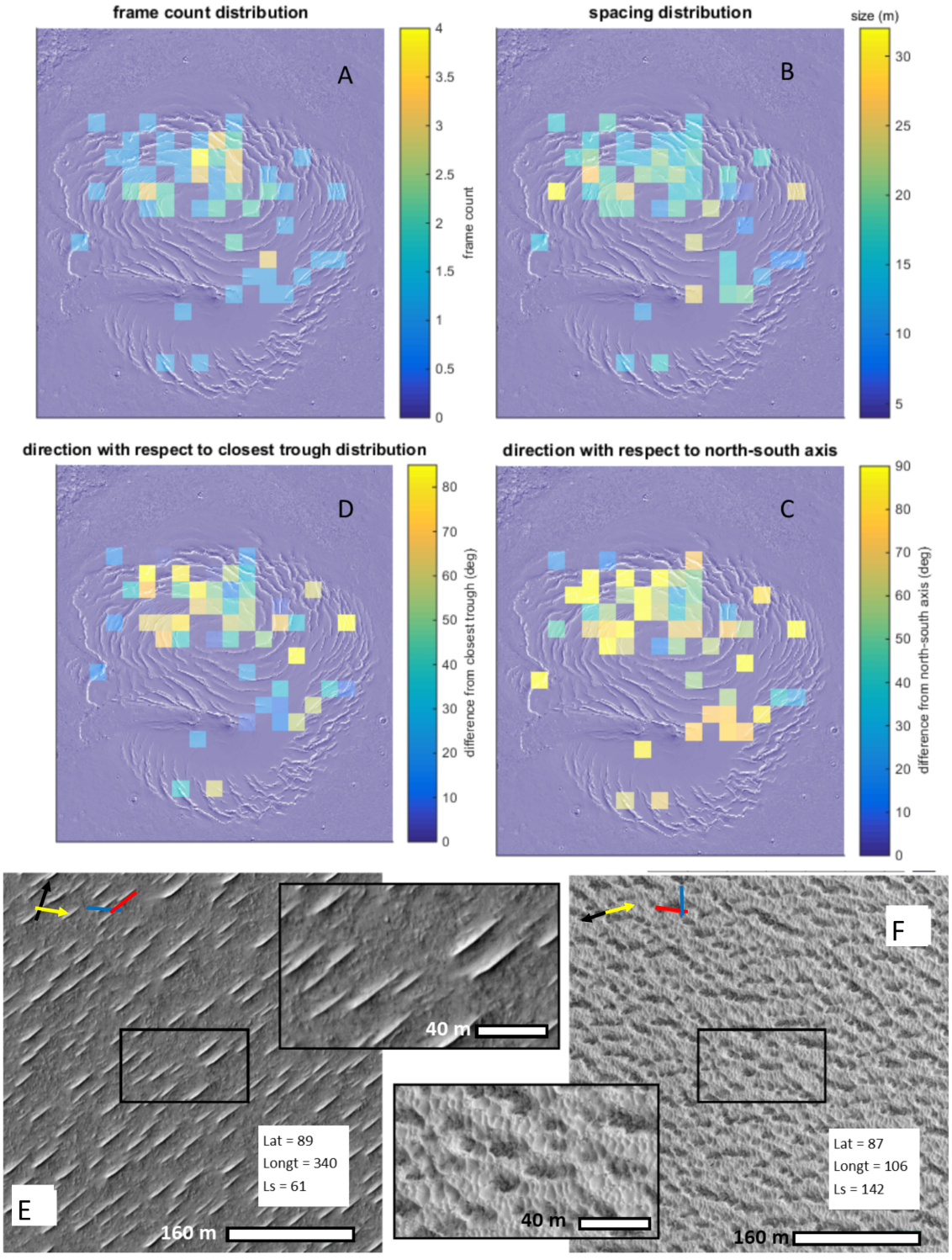

Figure 3.8: Panel A shows the mapping of TARs observed. Panel B shows the spacing (m) and panel C shows the orientation (°) with respect to the North-South axis. Panel D shows the orientation with respect to the closest trough. Panel E shows simple TARs in HiRISE image ESP_025758_2695. Panel F shows networked TARs in HiRISE image ESP_036839_2670.

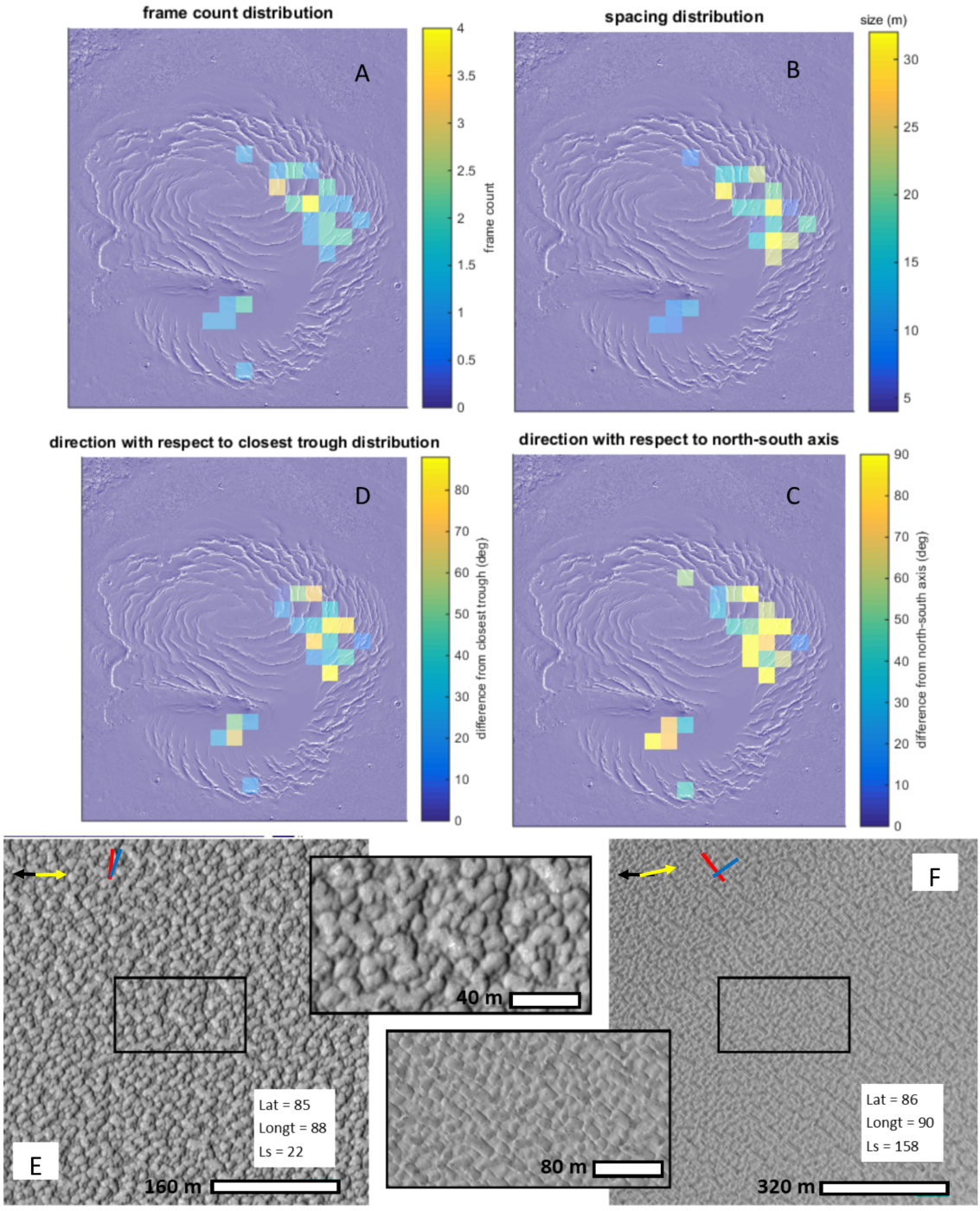

Figure 3.9: Panel A shows the mapping of pits observed. Panel B shows the spacing (m) and panel C shows the orientation (°) with respect to the North-South axis. Panel D shows the orientation (°) with respect to the closest trough. Panel E shows HiRISE image ESP_024643_2655. Panel F shows HiRISE image ESP_037262_2660.

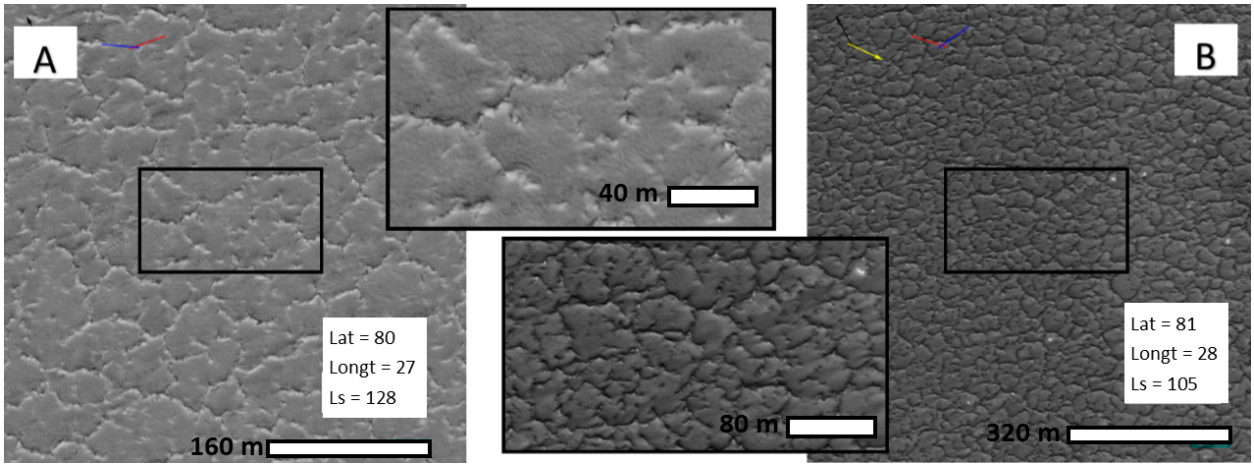

Figure 3.10: Panel A shows polygonal features in HiRISE image ESP_018844_2605. Panel B shows HiRISE image ESP_035841_2610.

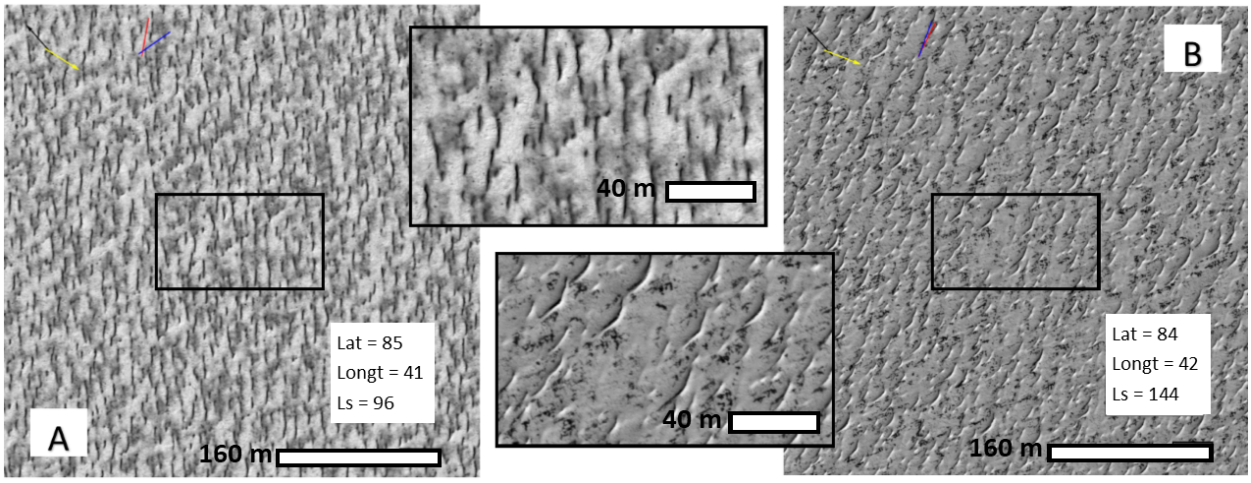

Figure 3.11: Panel A shows "slits" in HiRISE image ESP_026781_2650. Panel B shows HiRISE image ESP_037053_2645.

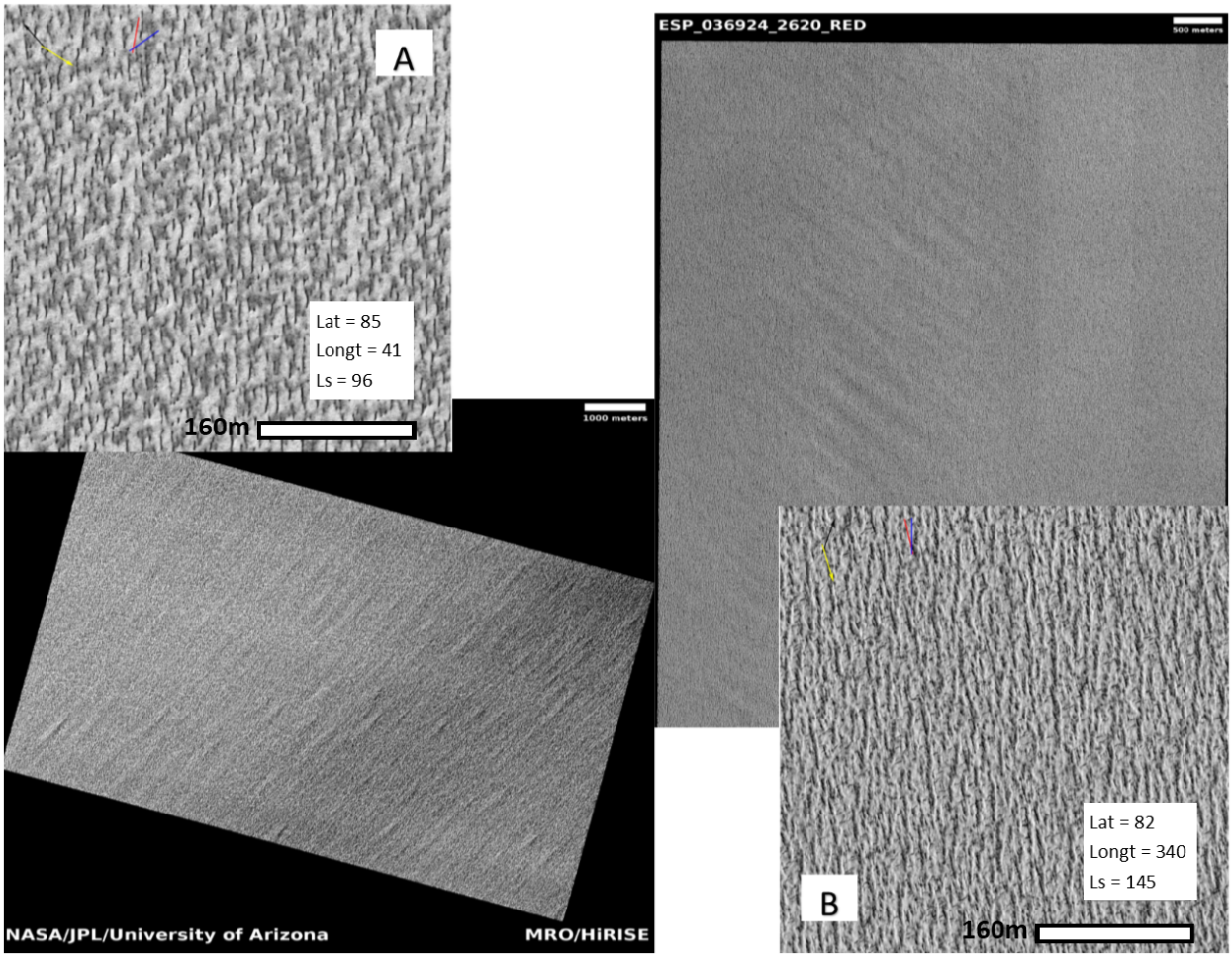

Figure 3.12: Panel A shows HiRISE image ESP_026781_2650 where the orientation of smaller "slits" is straight up and down while the bigger features' orientation leans more to the right. Panel B shows HiRISE image ESP_037053_2645 where the orientation of sastrugis (Herny et al., 2014) leans left while smaller uncategorized features orientate up and down.

3.2 Sublimation-driven Surface Features

3.2.1 Possibilities of Penitentes and their Preferred Orientation

With latitude bands of 10°, the latitude most representative of the NPLD is 80°. 3 main runs were done: no tilt on the surface contour with internal reflection where the albedo is 0.5, 60° tilt on the surface contour without internal reflection representing a surface with low albedo, and 60° tilt on the surface contour with internal reflection at a surface albedo of 0.5. At 80° latitude, Ls 210 - 330 have no sunlight. Only one bounce is attributed to the internal Lambertian reflection therefore most of the energy absorbed is from the initial incoming solar flux.

For a surface contour without any tilt, there were no Ls found that had conditions favourable for penitentes growth. Even with internal reflection, most the energy absorbed is on the sides (the upper $2/3^{\text{rd}}$ depth). Even so, the direction that had the most energy absorption in the trough are contours with 0°, 180° and 360° rotation to the original orientation thus favouring an east-west orientation of the hypothesized penitentes.

For the low albedo surface with tilt, energy absorbed cumulatively throughout the year did not have favourable conditions for penitente growth. However, the were a few Ls that did have prominent incoming solar fluxes that focused into the trough of the surface contour. The Ls that showed this were around Ls 20 and Ls 160; this can be seen in figure 3.13.

For the tilted surface with internal reflection of 1 bounce, there is enough year-round energy absorption in the bottom-third of the parabolic surface to favour penitente formation. As expected, the most preferred orientation is in the east-west direction with the surface tilting towards the equator. This is shown in figure 3.14.

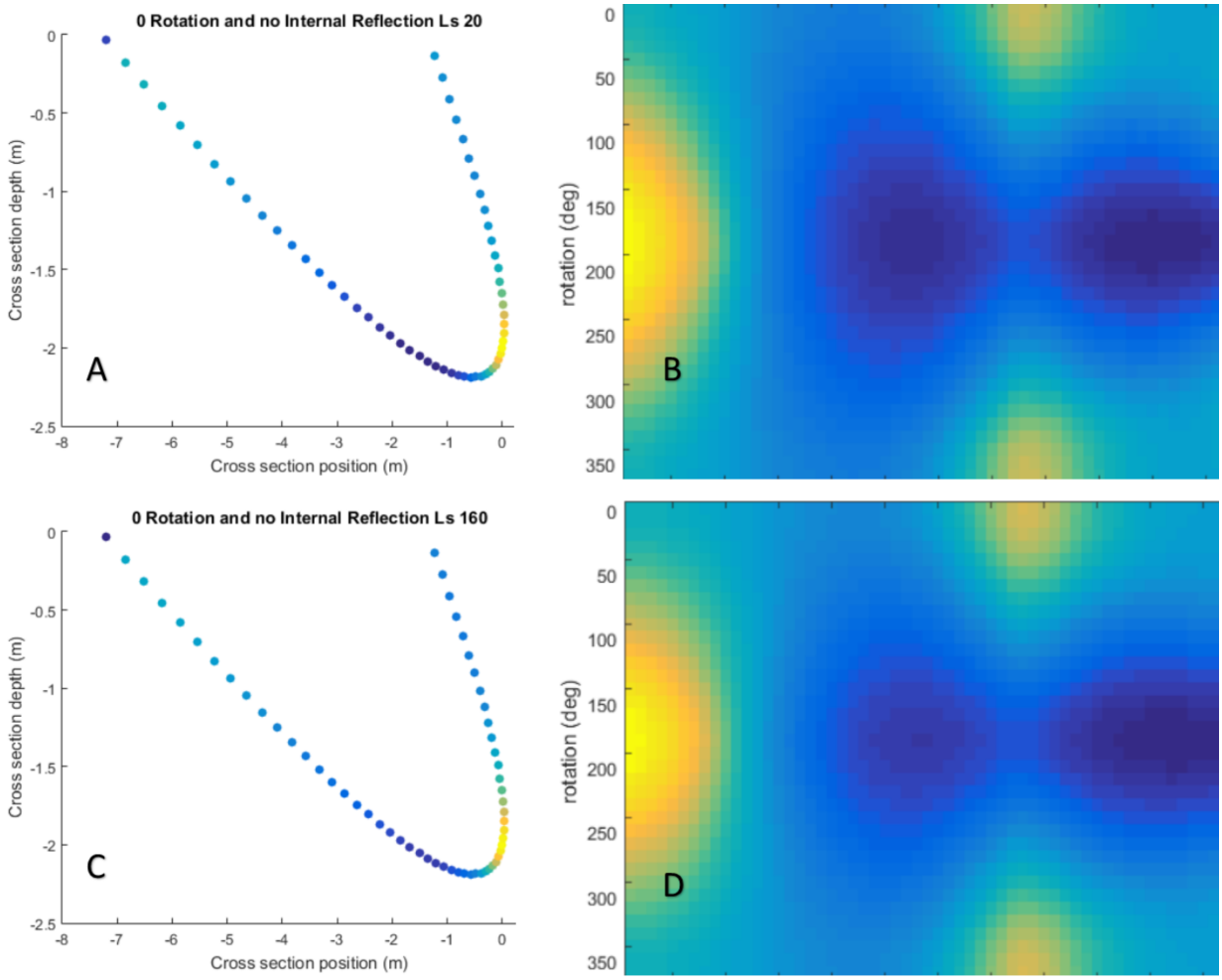

Figure 3.13: Panel A and B shows the reflection-less surface energy absorption for Ls 20. Panel A is the surface cross-section for an east-west oriented penitente with the tilt pointing towards the equator. Panel B shows the absorption of the surface with respect to rotation. The formatting of both panels is exactly like figure 2.14. Panels C and D are exactly like panel A and B but is instead in Ls 160.

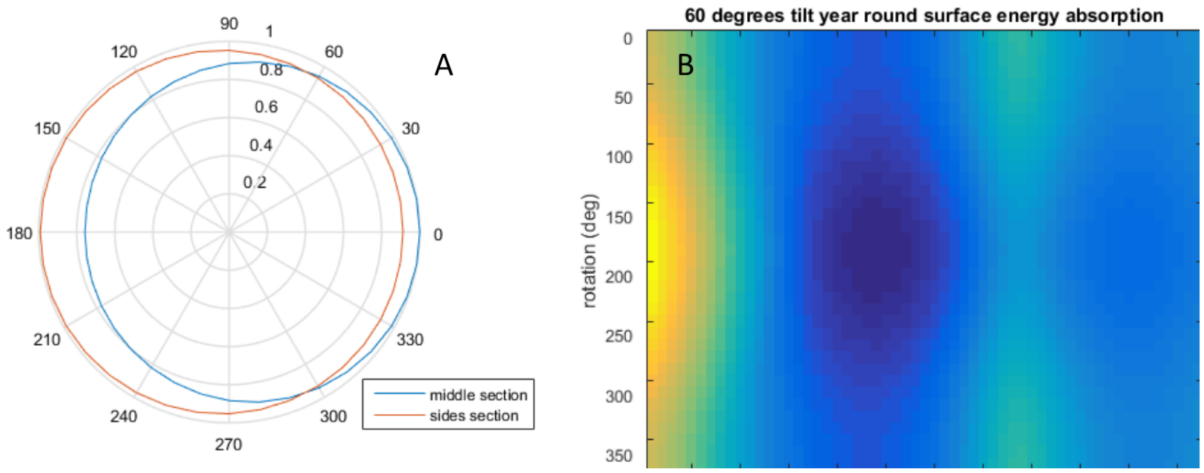

Figure 3.14: Panel A shows the polar plot of energy absorbed from the incoming solar flux and the subsequent internal reflection where the middle section represents the bottom-third depth and the sides' section represents the upper $2/3^{\text{rd}}$. Panel B shows the scaled image representation of the surface energy absorption with respect to rotation and is in the exact same format as figure 3.13 panels B and D.

For hypothetical penitente formation outside of the NPLD, simulations for contours without tilt were done for the latitude range of the northern hemisphere. The results of each latitude band are then grouped into the four seasons and two different albedo values were used: 0.2 and 0.5. These simulations show that summer is the best season for penitente growth and that the most favoured orientation is always east-west. Similar to Cathles et al. (2014), these simulations are done to test the geographic constraint of penitente formation.

For an albedo of 0.2, penitentes can form year round up to a latitude of 10°. However, by restricting the time range to the summer season, penitente can form up to a latitude of 40°. For an albedo of 0.5, penitentes can form year-round up to 60° latitude. In the summer, their formation can even reach 70°. All of this is shown in figure 3.15.

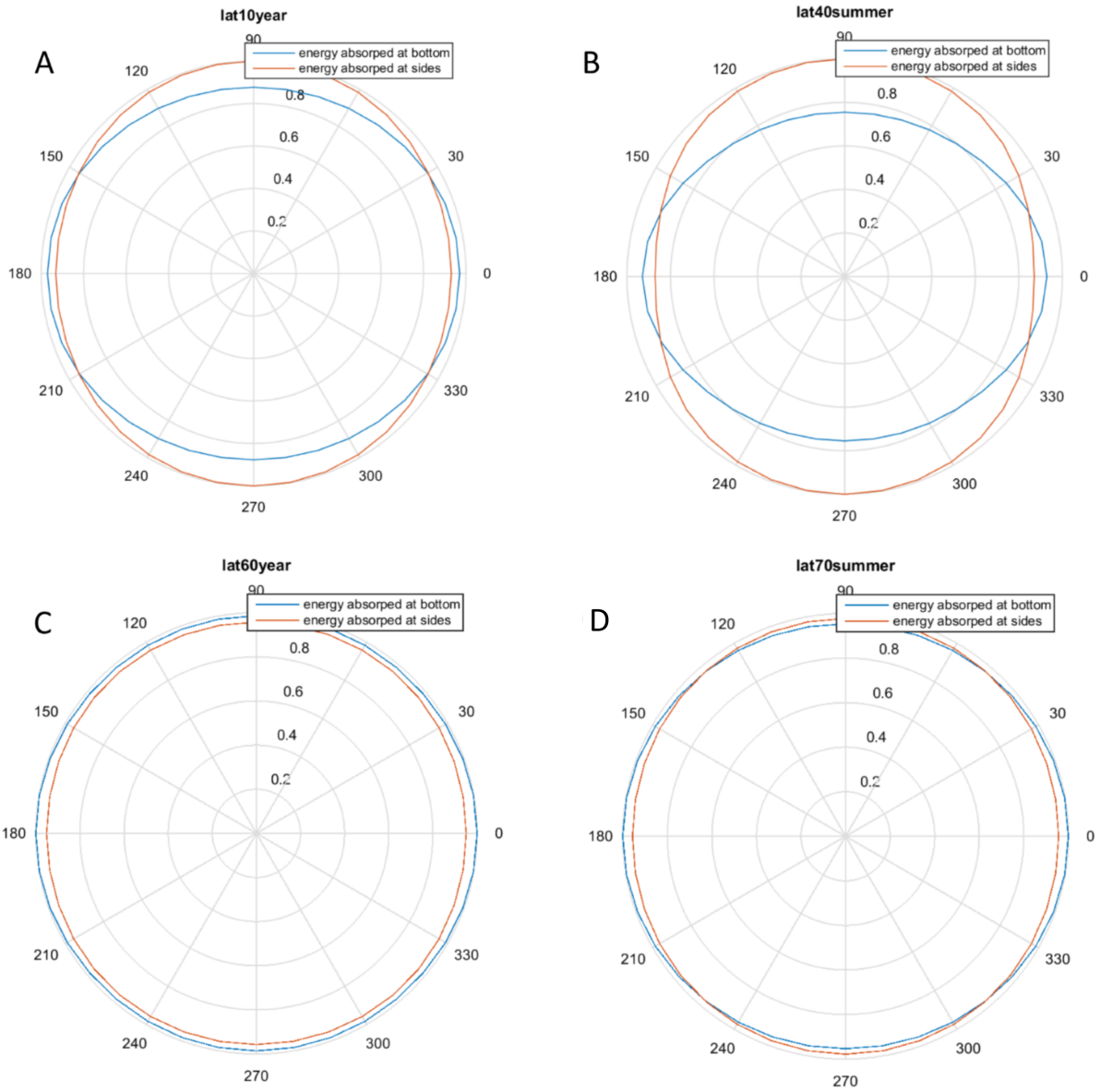

Figure 3.15: Each panel in the figure is in the same format as panel A from fig 3.14. Panels A and B show energy absorption of the contour for a surface with an albedo of 0.2 and no tilt. Panel A shows year-round energy absorption at 10° N while B shows energy absorption for the summer season at 40° N. Panels C and D show energy absorption for a surface albedo of 0.5. Panel C shows year-round energy absorption at 60° N and panel D shows energy absorption in the summer at 70° N.

3.2.2 Penitentes Preferred Sizing through Fastest Growth Rate

Using equation 2.7 and finding the maximum growth rate using parameters introduced and specified in chapter 2 yielded a maximum growth rate around 10 km. This is shown in figure 3.16. However, when substituted in frictional velocity u_* of 0.4 m/s from a more in-depth analysis of the Martian Planetary Boundary Layer (Petrosyan et al., 2011) instead of assuming a laminar flow, the mixing length becomes much more shallow to about 8 cm. This smaller mixing length lowers the wavelength with maximal growth to be about 250 m. This is shown in figure 3.17.

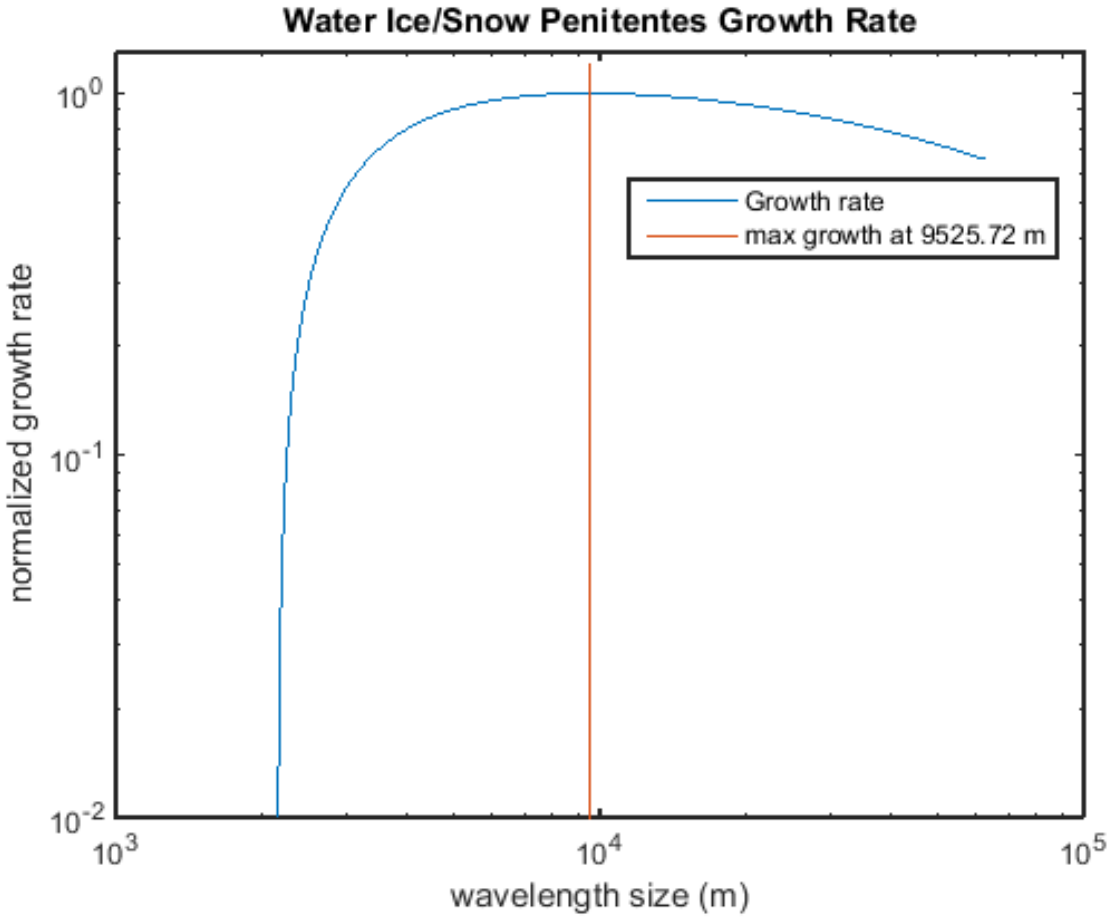

Figure 3.16: The figure shows the normalized growth rate for water snow/ice penitentes. It should be noted that both the growth rate and wavelenght axes are on a log scale.

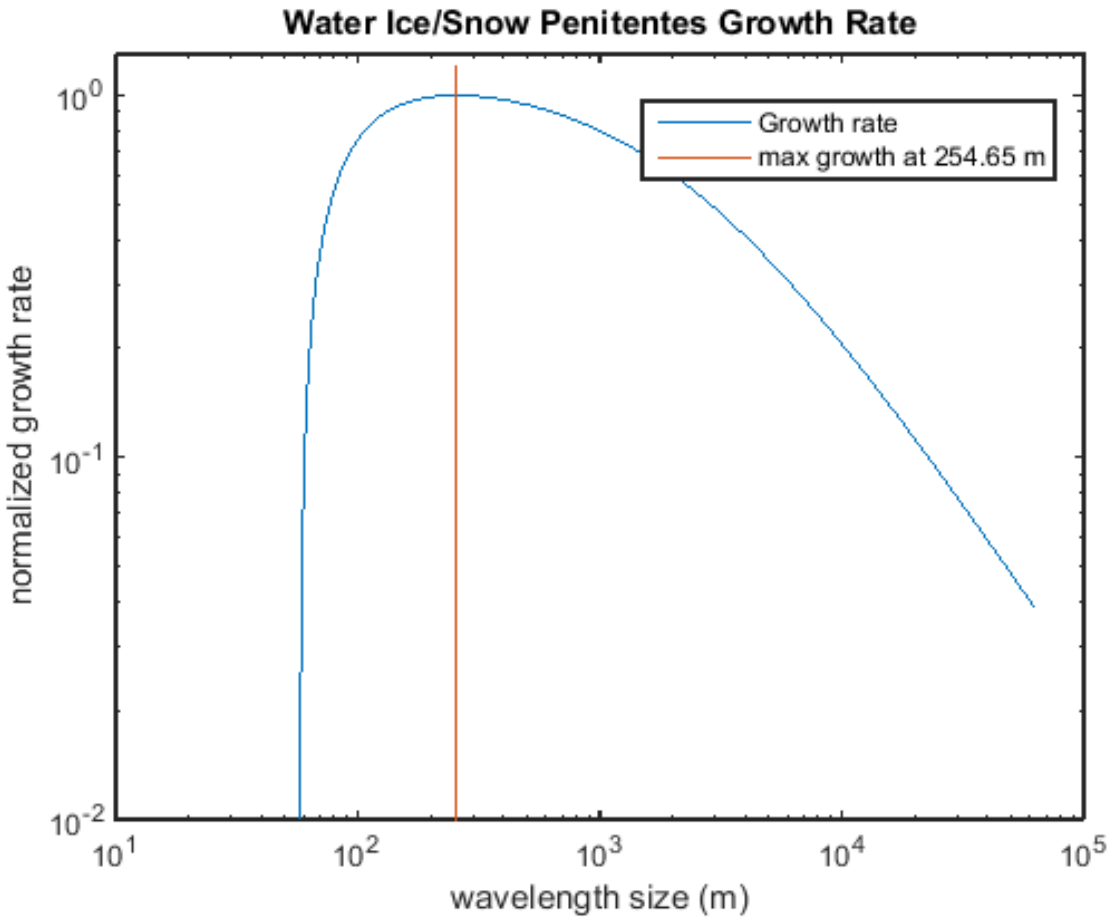

Figure 3.17: The figure shows the normalized growth rate for water snow/ice penitentes. It should be noted that both the growth rate and wavelength axes are on a log scale.

Chapter 4

Discussion

4.1 Surface Features on HiRISE

Although the 2D-FFT method works well for straight and consistent patterns, many of the surface features may require a more manual approach or different automated approach. However, through analyzing regional concentration of the features in the results section, regional dependence of various surface features can be inferred. It should be noted that the FFT analysis, when determining orientation, does not specify direction such that features perpendicular to the north-south axis are treated as both easterly and westerly. This may be troublesome for inferring wind from dunes with barchan-like qualities where specific wind directions can be derived visually but not through the FFT analysis. The orientation value derived from the FFT is the orientation of the axis for these features.

4.1.1 Dunes

With aeolian activities observed via dunes and ripples throughout the NPLD, the most likely material for sediment transport is snow and/or ice particles. Transverse dunes and ripples

mapping in figure 3.2 seems to concentrate from 90° E - 180° E. This corresponds to region 1,4 and 5 of the Smith and Holt (2015) NPLD characterization (figure 1.1). The orientation also does not seem to be follow a specific trend nor are they regionally dependent but this may be caused by the inclusion of the braided pattern and perpendicular barchans seen in figure 3.6. Tsoar et al. (1979) noted that braided terrain are likely to form in bimodal and perpendicular wind regimes but the derived orientation from the FFT only selects one direction even when there are multiple orientation tendencies observed. However, transverse dunes are fairly consistent in spacing and seem to follow the trend of getting bigger when moving towards the pole. With the exception of an outlier at around 80° E at the southern edge of the cap, this increasing sizing tendency can be seen in figure 3.5. Even though it has been noted that ripples and dunes are separated by size, morphologically similar features that are not in the same size range as their groupings will be grouped in favour of morphological similarities.

There were many features that have a strong longitudinal consistency (and therefore grouped as transverse dunes) but exhibit barchan-like qualities with crescentic slipfaces. These perpendicular crescent slipfaces often align themselves orthogonally to the nearby troughs suggesting katabatic winds to be the main driver of formation. A few of these sample cases are shown in figure 4.1.

The other interesting subset of transverse dunes, the braided pattern, suggests orthogonal pairs of prominent wind directions. This pattern is most apparent from panel C of figure 3.6. Additional sample frames that exhibit this pattern along with features observed by Tsoar et al. (1979) are shown in figure 4.2. When compared to the features in the Tsoar et al. (1979) paper, there is a huge difference in scale as the braided features found on the NPLD are typically smaller than 30 m. When mapping the braided patterns and transverse dunes with orthogonal barchan-like crescents, this could lead to finding regions prone to a bimodal wind distribution. This is done in figure 4.3 where the area around 110° E is then seen to

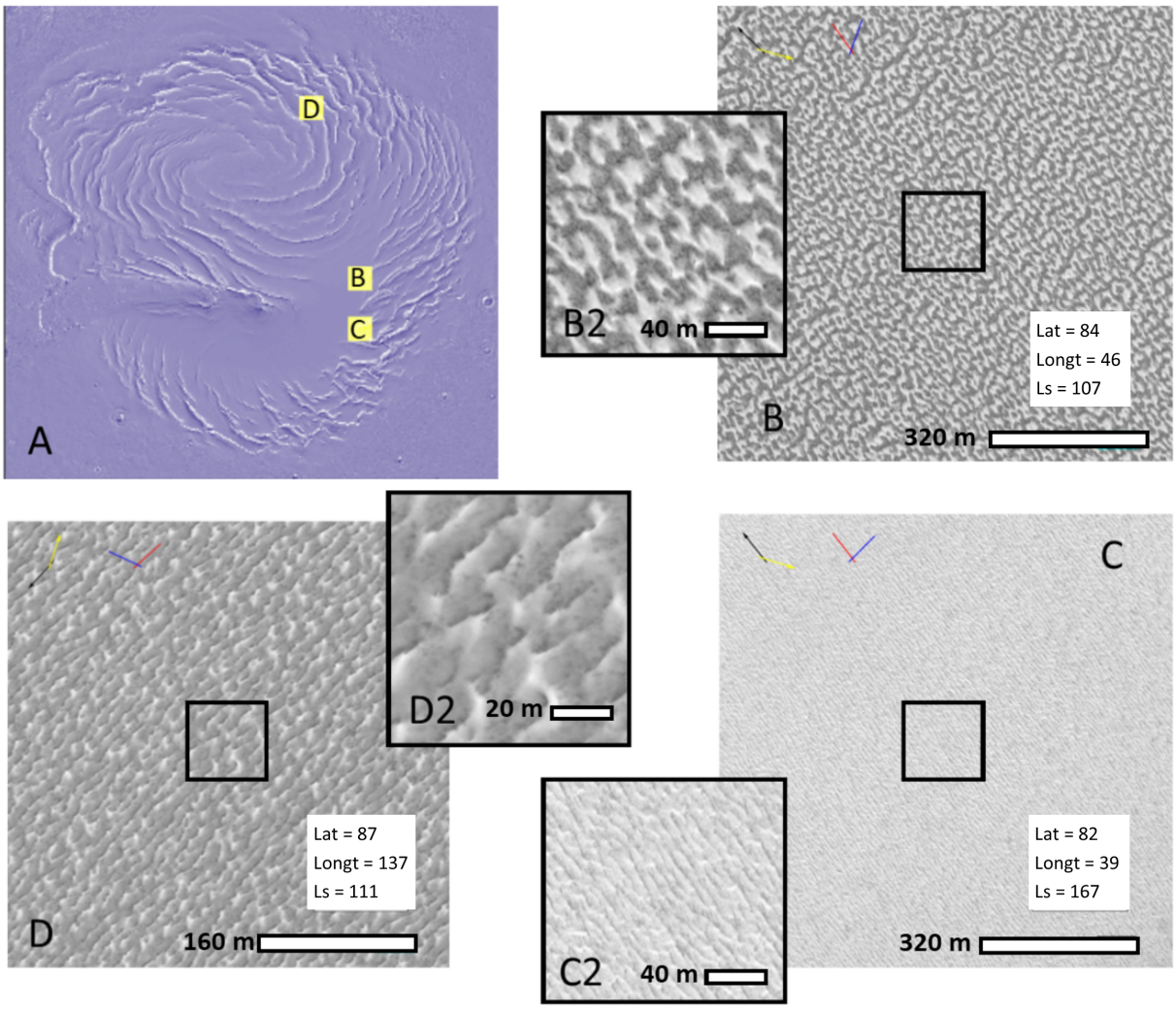

Figure 4.1: Panel A shows the sample mapping of the frames in the figure. Each coloured box represent the location of the frames found in each subsequent panel. Panel B is taken from HiRISE image ESP_018276_2635 where B2 zooms in the box in the middle of panel B. Panel C is from ESP_028641_2625 and panel D is from ESP_036008_2665.

have a significant amount of these features. This corresponds to the border region around region 1 and 4 of figure 1.1.

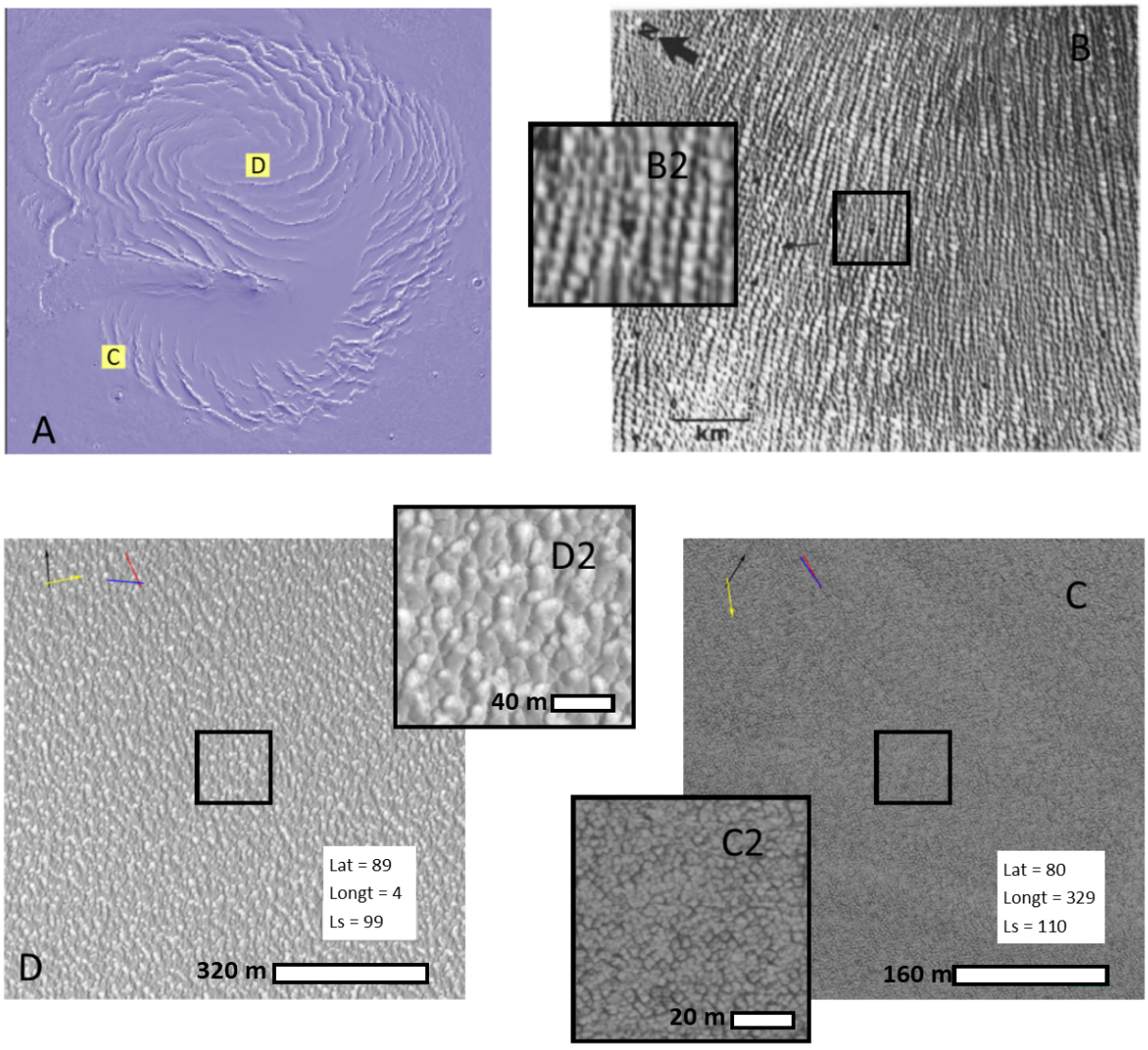

Figure 4.2: This figure follows the same format as figure 4.1 Panel A shows the location of HiRISE images represented by panel C and D. Panel B shows the braided pattern extracted from Tsoar et al. (1979). Panel C is taken from ESP_027180_2600 while Panel D is from ESP_044495_2695.

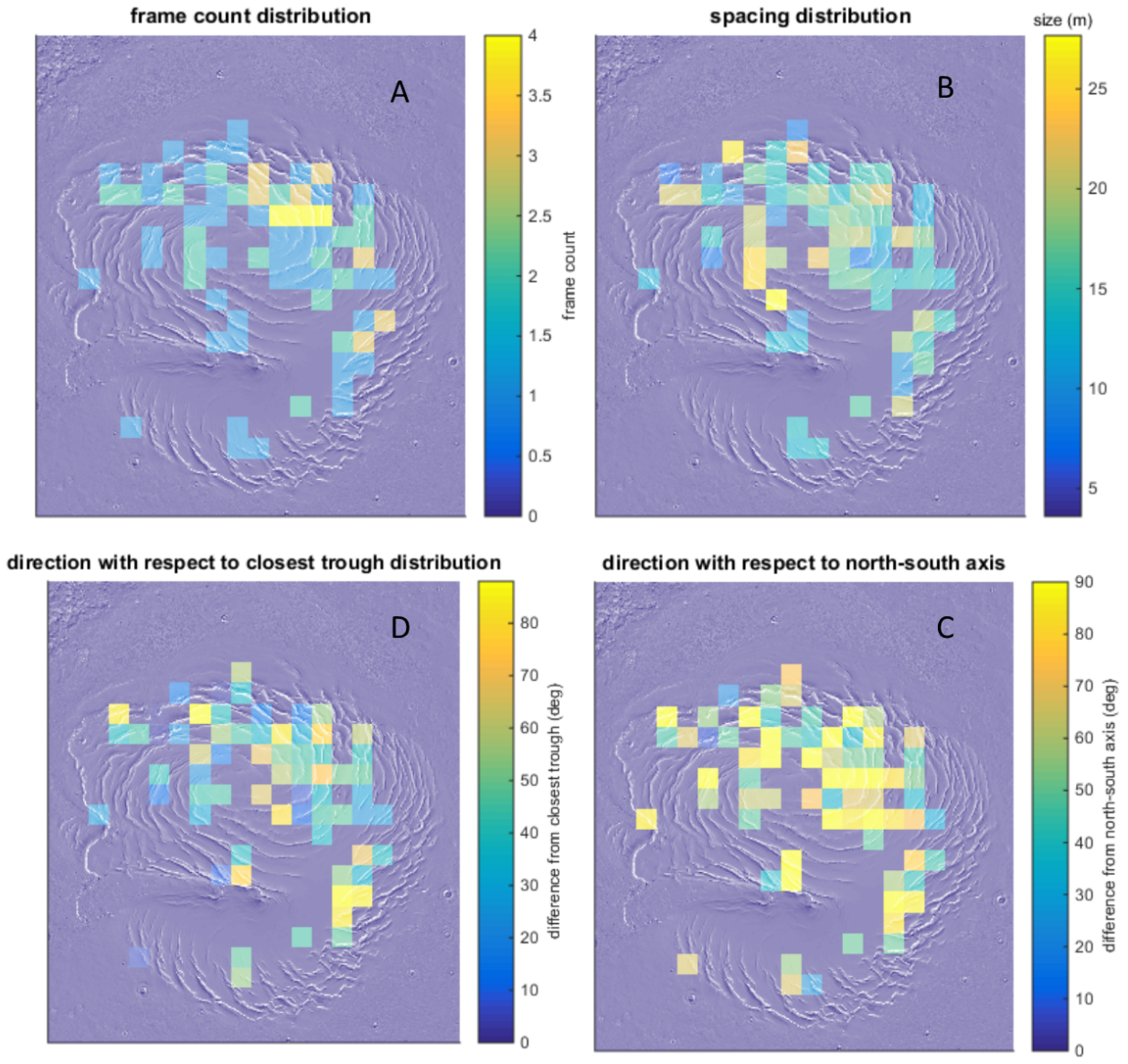

Figure 4.3: Panel A shows the mapping of features that are likely to form under bimodal wind regimes. Panel B shows the spacing distribution, panel C shows the orientation with respect to the north-south axes, and panel D shows the orientation with respect to the nearest trough.

While braided patterns along with transverse dunes with orthogonal barchanoid patterns seem to form under bimodal wind regimes, star dunes are features that form under multiple directions of wind. They are identified for their sharp and bright crests that branch out forming a pyramid base. Terrestrially, complex wind regimes that can form star dunes appears to be a result of significant seasonal variance in air circulation (Lancaster, 1995). Star dune patterns do not have consistent direction and spacing and therefore the spacing and orientation derivations from the 2D FFT are less relevant than for other dune and ripple-like features. However, mapping the concentration of star dunes on the NPLD can lead to finding regions with comparatively sporadic wind regimes. This is done in figure 4.4 accompanied with a larger star dune example from the Hayward et al. (2007) paper. When looking at star dunes' regional distribution, there appears to be a hot-spot of these features around 130^{o} E or in region 4 from fig 1.1. This can be seen in panel A of figure 4.4. Region 4 has poor observation geometry but is characterized with large-scale erosion and deposition (Smith and Holt, 2015). Many of the dunes and ripples found are located within region 4 and 5; these regions are observed to have the highest average slope of 0.32 degrees compared to all other regions with region 4 having the biggest deviation in slopes (Smith and Holt, 2015).

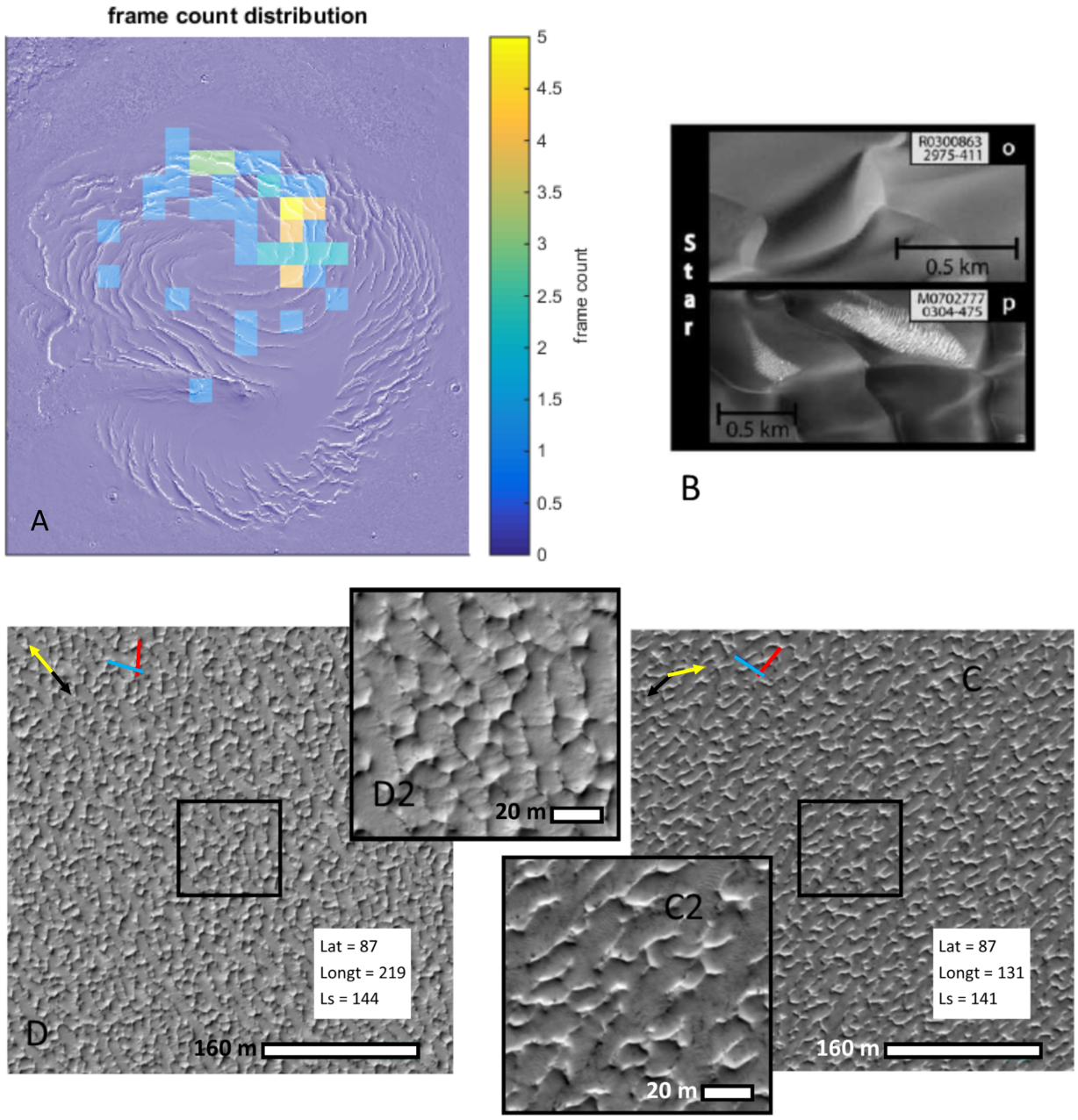

Figure 4.4: Panel A shows the mapping star dunes found on the NPLD. Panel B shows star dune examples from Hayward et al. (2007). Panel C is taken from ESP_036837_2635 while Panel D is from ESP_036914_2665.

4.1.2 Ripples

Although larger wave-like patterns are characterized as transverse dunes and not ripples, some and maybe most features observed may be mega-ripples but this work was not able to visually distinguish the differences. In fact, some ripple features are almost identical to large-scale transverse dunes seen in Hayward et al. (2007) except for the huge difference in size. This is illustrated in figure 4.5. The scale of these features is 10-30m which is much bigger than the ripples observed by Vaz et al. (2017) but much smaller than the spacing laws of Martian dunes done by Claudin and Andreotti (2006). These features instead fall within large wind ripples observed by MSL's Curiosity Rover (Lapotre et al., 2016). Due to the high kinematic viscosity of the low-density Martian atmosphere, these "transverse dunes" resemble fluid-dragged ripples but are actually formed by the Martian winds.

Ripples observed seem to have the most consistent sizing of 8-10 m at region 5 around 45° E- 130° E seen in panel B of figure 3.3. Smith and Holt's work signify that this particular region with its young troughs has much steeper equator-facing slopes. This has slight implications that strong katabatic winds may give rise to more consistently spaced ripples and/or dunes. Ripples that change direction at the proximity of the troughs are seen in figure 3.7. The features are observed to change direction downwind from the katabatic flow south of the trough. They could be affected by the katabatic jump as region 5's steep slopes make katabatic jumps more favourable than other regions. The katabatic jumps will inflict a sudden change in wind, pressure, and temperature (Smith et al., 2015) where they could act as the irregular yet local flow that leads to sudden changes in the direction of these ripples. However, this would imply that these ripples are formed aligning with the general wind direction making them more like longitudinal dunes; these ripples do not appear to have the long straight crests characteristic of longitudinal dunes. Ultimately more observations are needed to form any concrete assertions.

Inferences of the wind direction can now be made when isolating ripples and transverse

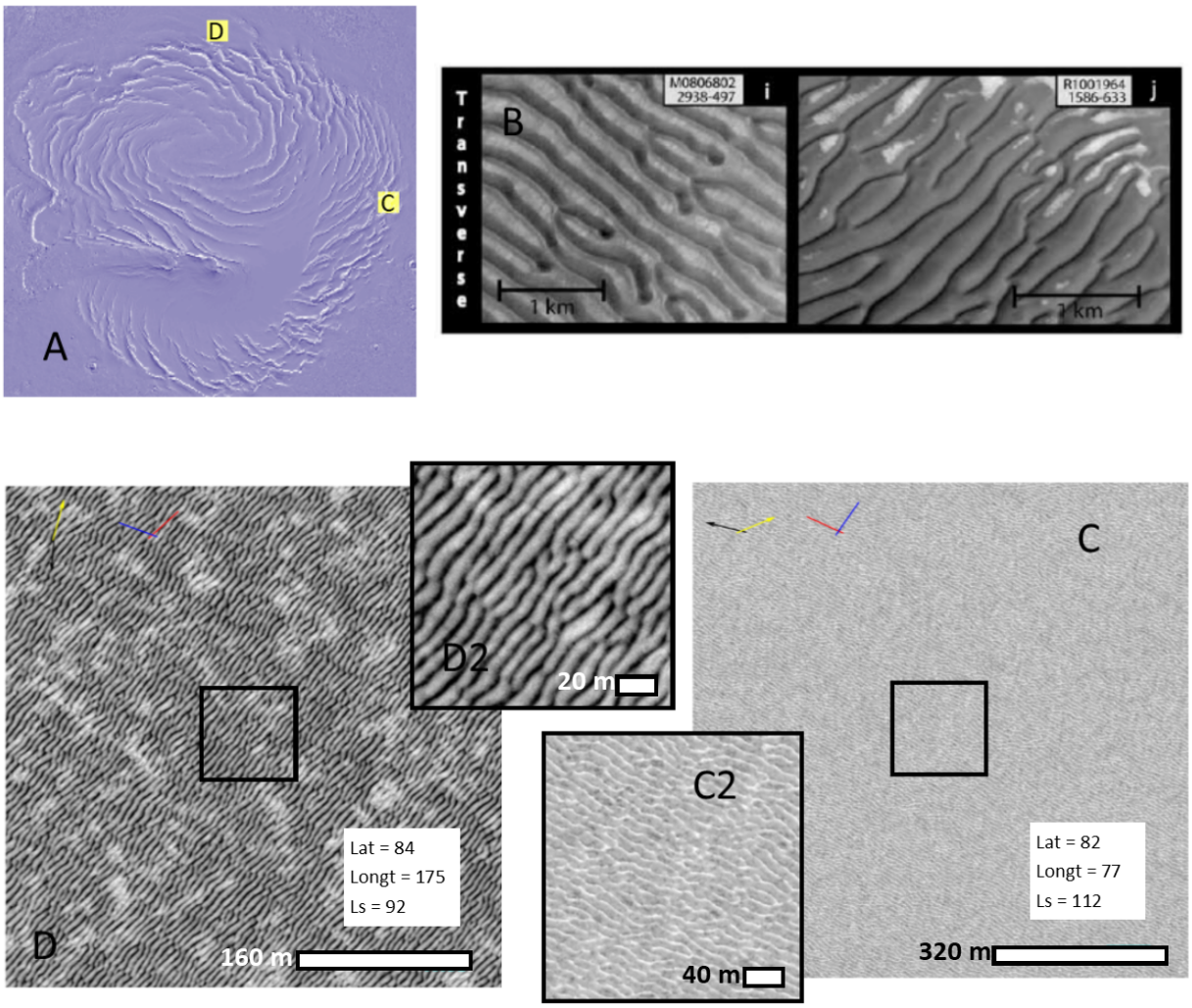

Figure 4.5: This figure follows the same format as figure 4.1 where the highlighted box represents the location of HiRISE images of panel C and D. Panel B shows examples of transverse dunes from Hayward et al (2007). Panel C is from ESP_036037_2620 and panel D is from ESP_035478_2640.

dunes on the NPLD. This is shown in figure 4.6. The wind directions are assumed to be perpendicular to the orientation of the features and only transverse dunes with a single mode of orientation are considered. While the orientation of features inferred from the FFT does not specify direction, the derived wind tracks are assumed to be northerly which is consistent with the katabatic flow observed by Massé et al (2012).

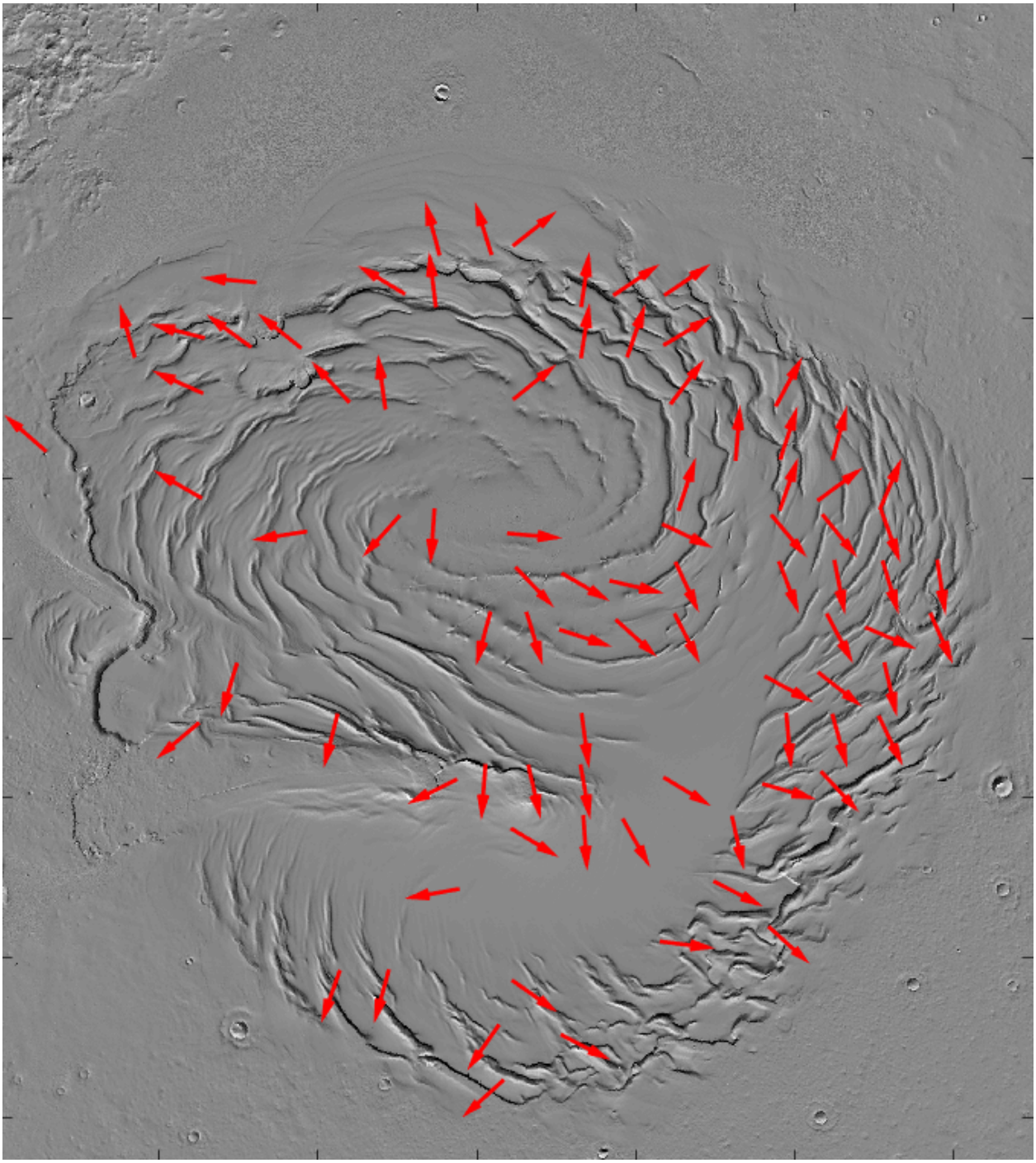

Figure 4.6: The figure shows wind direction inferred from ripples and transverse dunes with unimodal orientation tendency.

4.1.3 Other Features

Balme et al. (2008) noted that the TAR distribution is latitudinally dependent with very few TARs north of 30°. However, TARs are found to be prominent on the NPLD although

they are immobile and suggested to be formed by an earlier climate (Kok et al., 2012) and may hold no relation to the current wind regimes. However, areas of high concentration of TARs found in figure 3.8 may suggest a certain grain size for the surface as Balme et al. (2008) has pointed out that TARs are covered in granule-size grains with finer grains underneath. However, the composition of the TARs on the ice and snow covered polar cap may be different to TARs found elsewhere on Mars. The concentration of TARs falls mostly within region 3 and region 0 of fig 1.1.

Another group that may form from aeolian processes are pits seen in figure 3.9. They could have aeolian origins as dome or rounded barchan features seen by Hayward et al. (2007). Domes are observed to be much more sparse, akin to barchans, than the pits observed in this work. However, many of the pits exhibit very consistent spacing and orientation. This is shown in figure 4.7. Despite this, their round edges, especially on small scales (<20 m), can be easily mistaken for the braided pattern by confusing convex and concave surfaces; distinguishing these may not be trivial when looking from a top-down aerial view.

As for the features within features specified in figure 3.12, two theories based on Lancaster (1988) are proposed to describe the process for which this is possible. This, however, would be under the assumption that the smaller features are aeolian in origin. The first theory is that the smaller features are ripples superimposed on the lee flanks of the larger features where the larger features' spacing is determined by the saltation length while the smaller features' spacing is determined via the reptation length. The second theory is that the region contains ergs or megadunes which are complex systems of dunes with the smaller features superimposed on the larger features. The dunes are formed at different periods of time where smaller ripples are formed by the current wind regime and the larger features are formed from an earlier climate with another different wind regime.

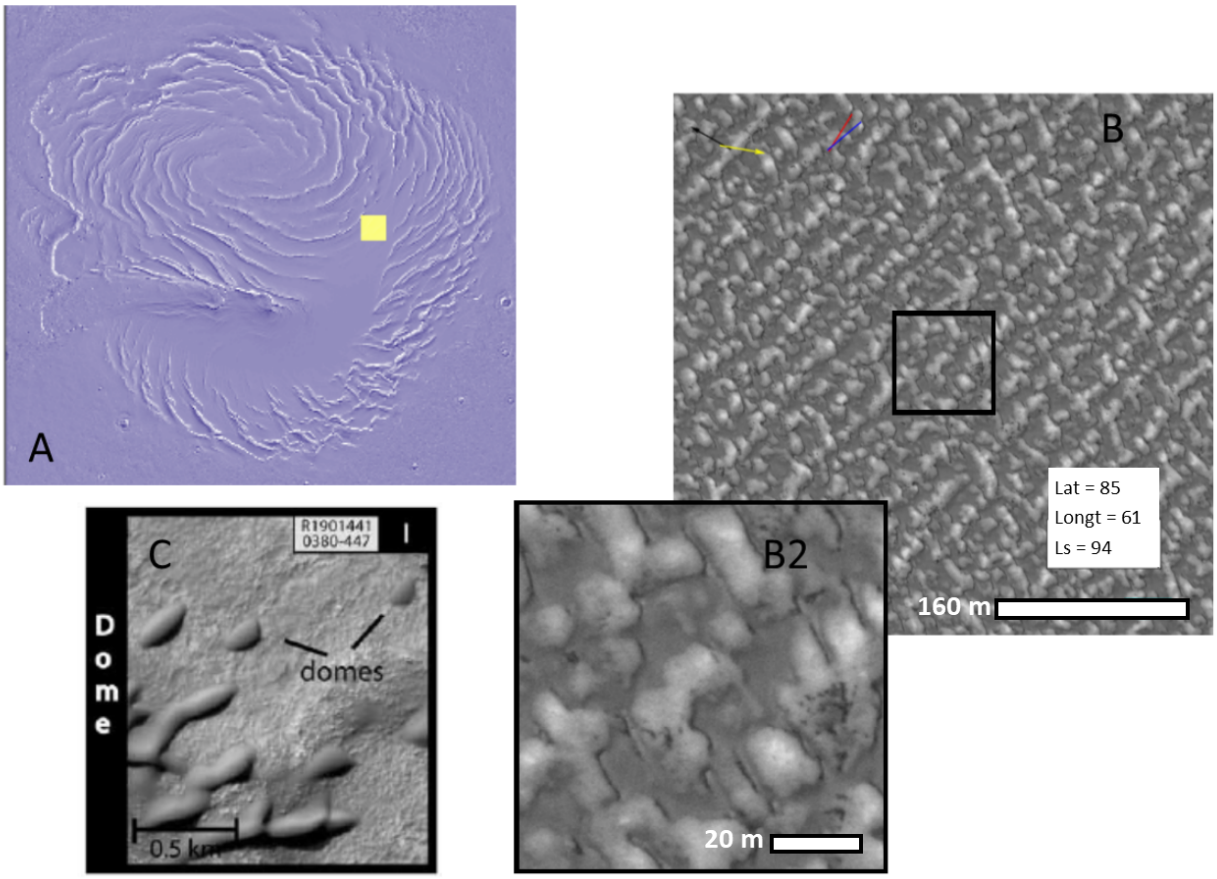

Figure 4.7: Panel A shows the location of the frame of panel B. Panel B is from ESP_035536_2650. Panel C is an example of dome dunes from Hayward et al. (2007).

4.2 Possibilites of Penitentes

A vertical tilt of 60° with internal reflection can produce favourable conditions for penitentes growth. The results imply a preferred orientation of being in the east-west direction which makes sense when taking the work of Cathles et al. (2014) into consideration. Given Earth's and Mars' similar orbital mechanics (in particular their tilt), penitentes orientating east-west have more incoming solar flux than having a north-south orientation. However, objectively comparing the parameters used and the actual conditions of the NPLD seem to lessen the likelihood of forming penitentes.

The incoming solar fluxes with respect to latitude is limited to discreet intervals of 10°.

Using 80° latitude is in no way representative of the polar cap as 80° is at the very southern edge. 85° latitude is a much better regional representation of the NPLD. Very few HiRISE frames are gathered at 80° as only 39/559 fall within 79°-81°. The steep tilt of 60° (from the vertical) is a bit more palatable as the spiraling troughs of the NPLD may provide the necessary elevation gradient to induce such a tilt. The albedo of 0.5 used, despite being in the range of albedo found by Bass et al. (2000), is too reflective for such a low latitude. The summer time albedo range of Bass et al. (2000) shows a low reflectance at the southern edge of the cap where the albedo is around 0.2 and gets more reflective northward where the albedo peaks at around 0.6 at the absolute middle of the north pole. However, the simulations ran only accounted for one reflection bounce and subsequent fluxes after the first bounce are simply unaccounted for. This would imply that the energy absorbed by the surface may not be truly representative of the specified surface albedo.

The effects of atmospheric scattering also play a significant role in the formation of penitentes. The scattered flux allowed for some insolation at a latitude of 80° for early spring time at around Ls 20-30. Without scattering, there would be no incoming flux at such a high latitude around that time using the Mars24 algorithm (Allison and McEwen, 2000). When looking at a sample case in late summer by taking a typical day around Ls 160, atmospheric scattering appears to increase the likelihood of penitente formation. This can be seen in panel C of figure 4.8 and figure 4.9. The sample case showed that the bottom portion of the penitentes get the most energy absorption, internal reflections included, when they are aligned east-west with the tilt towards the equator regardless of atmospheric scattering. However, the scattering allowed for more energy absorption at the bottom than the sides, favouring penitente growth.

When looking for geographic constraints of penitente formation, as seen in figure 3.15, the albedo plays a significant role. The higher the albedo, the more likely penitentes can form in the high latitude regions. For albedo values between 0.2 and 0.5, penitentes without tilt are

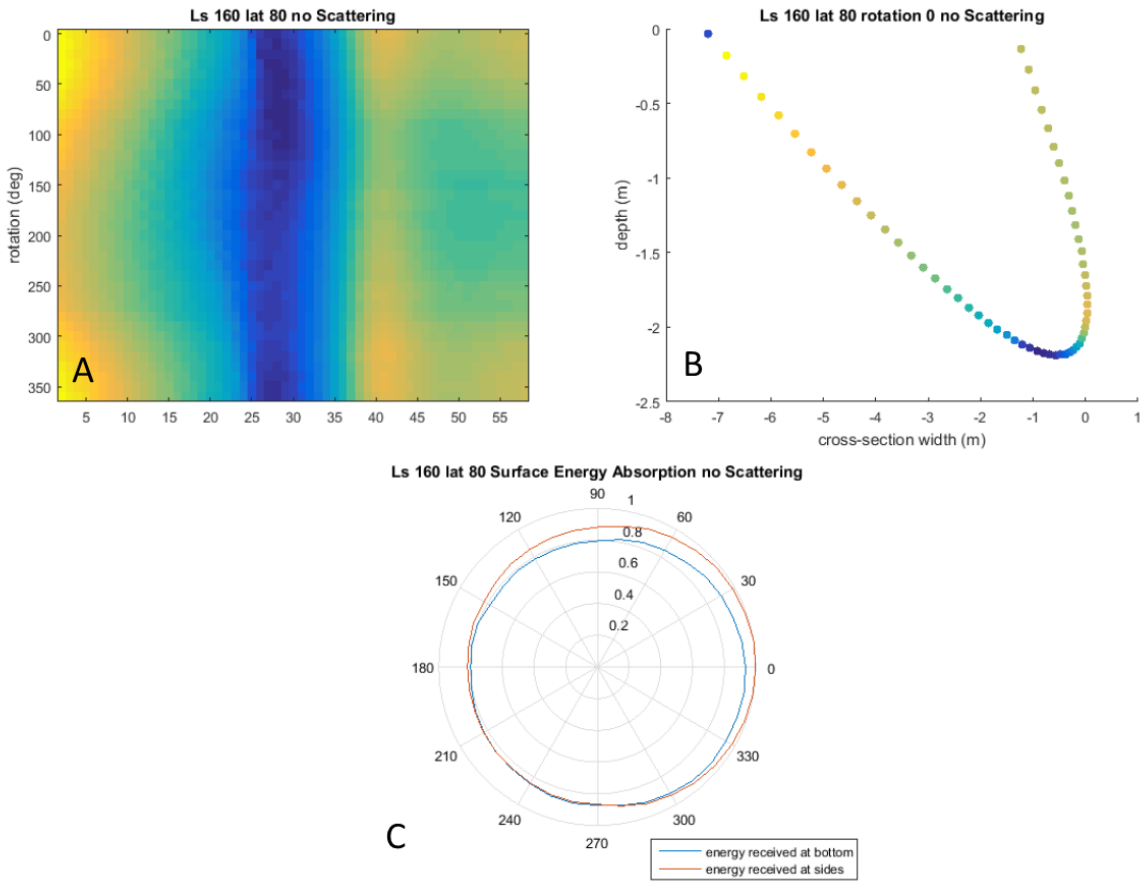

Figure 4.8: The figure shows a typical day around Ls 160 at a latitude of 80° using the Mars24 algorithm without any atmospheric scattering. Since the sun doesn't set around Ls 160, the whole day is taken to be the period between the two lowest points of elevation of the sun. Panel A shows the energy absorbed along the penitente cross-section with respect to the penitente rotation. Panel B shows the energy absorbed cross-section at 0° rotation (east-west orientation with the tilt towards the equator) representing the first row of panel A. Panel C shows the polar plot of energy absorption separated into the bottom and sides portion with respect to the penitente rotation. The figure shows that there is no clear orientation where the bottom third receives more energy than the sides. The asymmetry of the polar plot may be caused by the discreet 30 minutes time step when calculating the sun's position.

constrained to the mid-latitudes similar to Earth (Cathles et al., 2014). The latitude range might increase, however, by assuming that penitentes can grow only in spring and summer.

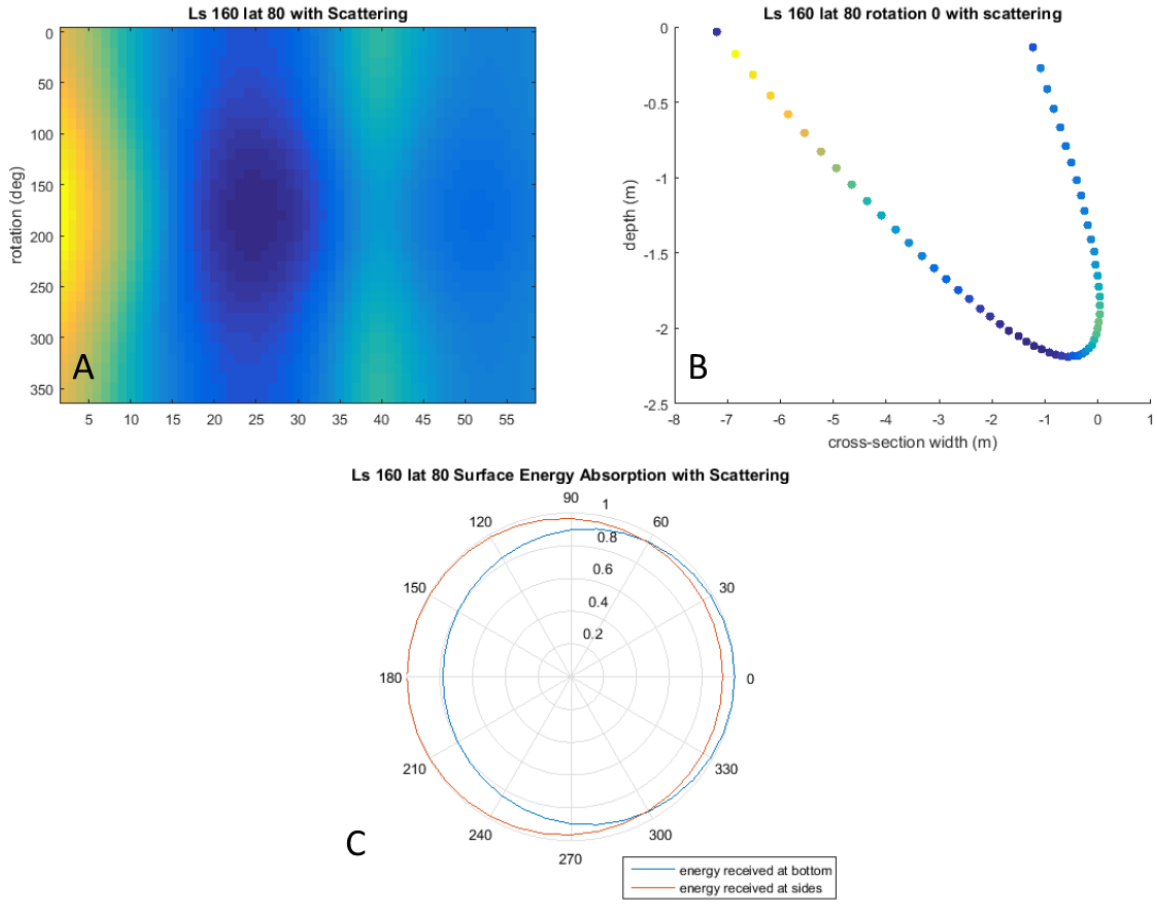

Figure 4.9: The figure has the exact same format as figure 4.8 except for the addition of atmospheric scattering. Panel A shows the relative energy absorbed along the cross-section with respect to orientation, panel B shows the contour at east-west orientation with southward tilt, and panel C shows the polar plot of energy absorption with respect to orientation when separated into bottom and sides portions. The figure shows favourable penitente formation at 60° deviation from east-west orientation with a southward tilt.

When finding the fastest growth rate of penitentes, albedo did not have significant effects. Other variables with negligible effects on the growth rate are the kinetic constant of sublimation α and the exponential value for the length of light penetration into the surface Λ. Variables that contribute largely to the growth rate but are more constrained are the latent heat of sublimation $\mathcal{L}$ and the sublimated vapour diffusivity D_ρ. Parameters of interest that play a significant role in penitente growth are the first derivative of the vapour density ρ'_{sat} and the mixing length l.

The first derivative of vapour density ρ'_{sat} was found to be dependent on the vapour pressure P_s which was then calculated via the Goff Gratch equation (Smithsonian, 1984). There are many models that could be used but ultimately those models tend to diverge as the temperature gets colder. Therefore, the accuracy of the first derivative of the vapour density ρ'_{sat} is very much in question. Investigating how much ρ'_{sat} affects the growth rate reveals that the higher the value, the smaller the wavelength of the fastest growing penitentes.

The mixing length l is a much less constrained parameter that seems to play a huge role in controlling the wavelengths of the fastest growing penitentes. This could be seen in figures 3.16 and 3.17. The frictional velocity u_* is instrumental in controlling the mixing length l but its values are more like estimations than rigorous measurements of fluid dynamics on the NPLD.

Only water ice/snow penitentes are considered. Given a cold enough temperature with springtime insolation, the possibility of CO_2 ice sublimating into penitentes is not explicitly ruled out. The main problem with considering CO_2-based penitentes is calculating the vapour diffusivity, which is problematic considering the assumption made about the Martian atmosphere that it is entirely composed of CO_2.

The results showed that penitente formation on the NPLD is not explicitly impossible. However, the conditions required are on the extreme side and the growth size calculations yield very large features. Therefore it is very unlikely that the HiRISE images collected

show features that are formed via sublimation-driven processes. This would accentuate the implication that any repetitive and wavy patterns found are almost entirely formed by aeolian processes.

4.3 Possible Flaws

The features characterized in this thesis follows the classification scheme for Earth especially for sand seas studied by McKee (1979). As mentioned by Hayward et al. (2007), many Martian dunes do not fit well within existing classification schemes and it is very easy to confuse different types of surface features on the NPLD. Despite the high resolution provided by HiRISE, subtle differences in morphology, in particular symmetry, useful for distinguishing linear and transverse dunes, are still difficult to observe, especially for features less than 10 m in size. Other difficulties, as discussed, include judging whether rounded features are dome-shape or bowl-shape as well as differentiating TARs from dunes. These difficulties make it likely that errors in the characterization of surface features have taken place.

There were possible flaws in the FFT analysis as well. Since confidence in spacing has less quantifiable aspects, as opposed to orientation confidence, the spacing value inferred is partly subjective giving way to human errors in judging the size of the overall feature. While the FFT analysis used can tell what the most dominant spacing and orientation values are, the analysis did not specify how much the features deviate from those values within a frame.

While the results do show that there is a concentration of star dunes, barchan-like transverse dunes, and braided terrain in region 4 and 5 of Smith and Holt (2015), a look back at panel A of figure 3.1 shows that more HiRISE images were extracted in those regions compared to other regions such as regions 2, 6 and 7. This could imply that these features can be abundant in other areas but their inferred regional dependence is limited to areas where there is simply more HiRISE data.

For penitente formation, there are flaws in both orientation and spacing simulation. When considering the internal reflections of the surface contour, additional bounces of light would more accurately determine the energy absorbed in the surface. Although this is negligible for low albedo values (< 0.2), it might not be so for higher values of albedo (> 0.5). For the calculations of penitentes' size preference, there were parameters such as saturated vapour pressure and frictional velocity that can affect the results significantly but are difficult to determine when applied to the conditions of the NPLD.

Chapter 5

Conclusions

In this investigation, various forms of aeolian-driven surface features found are mainly grouped into transverse dunes and ripples. Ripples were found to be very consistently spaced on the NPLD around 45° - 130° E, being around 8-10 m. Some ripples were also found to align themselves with the local katabatic winds suggesting that they are more like longitudinal dunes and are heavily subjected to katabatic jumps. Transverse dunes are observed to get bigger towards the pole. The sizing of transverse dunes on the NPLD are also less like typical Martian dunes and more like large-scale ripples characterized by Lapotre et al. (2016). In fact, for many of the dune morphologies found elsewhere on Mars, there exist a much smaller counterpart on the NPLD.

Dunes and ripples are often found in regions of relatively high slope in the NPLD. This may suggest that much of the aeolian processes are governed by katabatic winds. Some transverse dunes also display prominence to have formed in multi-directional winds that are perpendicular to each other. Prevalence of dunes exhibiting formation under more than one wind regime such as the braided pattern and star dunes suggest that katabatic winds may not be the only driver for the formation of these dunes. The concentration of star dunes around 130° E would imply that winds in that region will vary significantly from season to

season.

A significant number of features observed are TARs, hinting that although their presence gets rarer moving poleward, they are still observed on top of the NPLD. While areas with a high concentration of TARs can be interpreted as no longer being active in generating and maintaining aeolian-driven features (Kok et al., 2012), other areas may suggest otherwise. Dunes and ripples, likely driven by katabatic flow, can still be active considering that katabatic winds are still observed in the current Martian climate (Smith and Holt, 2015).

The Gemina Lingula hosts interesting surface features with superimposed features of different scale and orientation. The lack of HiRISE coverage in this area should be noted as more information in this region may uncover significant polar processes. Overall, many Martian surface morphologies are unsuited to be classified using terrestrial standards and more studies should be done on characterizing features unique to Mars.

Simulations show that penitentes can form on the NPLD, albeit with unfavourable conditions. The sizing scale of these penitentes falls around 10^2-10^3 m making the features observed extremely unlikely to be formed via sublimation. Similar to earth, the preferred orientation is in the east-west direction with a prominent tilt towards the equator. For penitentes without a tilt, their modeled growth is geographically constrained to the mid-latitudes for a surface albedo of less than 0.5.

5.1 Future Work

There is a case to be made on the prevalence of dune-like surface features to have regional dependencies within the NPLD. Other properties of dunes such as height and shape would be useful for studying aeolian processes. Eastwood et al. (2012) provides a methodology for investigating wind events from aeolian cross-data. This should prove to be useful to understand local conditions in the NPLD which hosts a series of regionally dependent aeolian-

driven features.

Whether or not aeolian-driven features are active could provide another avenue for future work. The work of Edgett and Malin (2000) is an excellent source to identify aeolian activity. Of three ways proposed, the first is to detect recent avalanches or slumps by looking for lineation on the slipface of dunes. The second way is to spot darker material under frosts and look for wind streaks. However, being on deposits of ice and snow, how well this work on layered deposits of ice and snow is debatable. The third way is to identify specific dunes, especially barchans for their low volumes, and track how they move over time. This may prove difficult since the features observed in this thesis are small and therefore it is hard to identify over multiple images.

Sublimation-driven processes are also very much opened to additional refinements. More robust internal reflection along with a consideration for energy balance should produce more confident results. For the scale of the fastest growing penitentes, additional runs with varying models for saturated vapour density would allow for better understanding of the sizing scales of penitentes. Runs with varying frictional velocity, such as accounting for turbulent flow instead of laminar flow, will also yield important results on the planetary boundary layer at the NPLD.

References

Anderson, R. S., 1987. A theoretical model for aeolian impact ripples. Sedimentology, vol. 34, issue 5, pp. 943-956. DOI:10.1111/j.1365-3091.1987.tb00814.x

Andreotti, B., Claudin, P., & Douady, S. (2002). Selection of dune shapes and velocities Part 1: Dynamics of sand, wind and barchans. The European Physical Journal B-Condensed Matter and Complex Systems, 28(3), 321-339.

Andrews, D. G. (2010). An introduction to atmospheric physics. Cambridge: Cambridge University Press.

Balme, M., Berman, D. C., Bourke, M. C., & Zimbelman, J. R. (2008). Transverse aeolian ridges (TARs) on Mars. Geomorphology, 101(4), 703-720.

Bass, D. S., Herkenhoff, K. E., & Paige, D. A. (2000). Variability of Mars' north polar water ice cap: I. Analysis of Mariner 9 and Viking Orbiter Imaging data. Icarus, 144(2), 382-396.

Bechtel, T. D., Forsyth, D. W., Sharpton, V. L., & Grieve, R. A. (1990). Variations in effective elastic thickness of the North American lithosphere. Nature, 343(6259), 636.

Blaney, D. L., & McCord, T. B. (1995). Indications of sulfate minerals in the Martian soil from Earth-based spectroscopy. Journal of Geophysical Research: Planets, 100(E7), 14433-14441.

Bourke, M. C., Wilson, S. A., & Zimbelman, J. R. (2003). The variability of transverse

aeolian ripples in Troughs on Mars.

Bridges, N. T., Ayoub, F., Avouac, J. P., Leprince, S., Lucas, A., & Mattson, S. (2012). Earth-like sand fluxes on Mars. Nature, 485(7398), 339.

Bridges, N., Geissler, P., Silvestro, S., & Banks, M. (2013). Bedform migration on Mars: Current results and future plans. Aeolian Research, 9, 133-151.

Byrne, S., & Murray, B. C. (2002). North polar stratigraphy and the paleo-erg of Mars. Journal of Geophysical Research: Planets, 107(E6).

Byrne, S. (2009). The polar deposits of Mars. Annual Review of Earth and Planetary Sciences, 37, 535-560.

Cathles, L. M., Abbot, D. S., & MacAYEAL, D. R. (2014). Intra-surface radiative transfer limits the geographic extent of snow penitents on horizontal snowfields. Journal of Glaciology, 60(219), 147-154.

Charru, F., Andreotti, B., & Claudin, P. (2013). Sand ripples and dunes. Annual Review of Fluid Mechanics, 45, 469-493.

Claudin, P., & Andreotti, B. (2006). A scaling law for aeolian dunes on Mars, Venus, Earth, and for subaqueous ripples. Earth and Planetary Science Letters, 252(1-2), 30-44.

Claudin, P., Jarry, H., Vignoles, G., Plapp, M., & Andreotti, B. (2015). Physical processes causing the formation of penitentes. Physical Review E, 92(3), 033015.

Crane Co. (1988). Flow of Fluids through Valves, Fittings, and Pipes

Durán, O., Claudin, P., & Andreotti, B. (2011). On aeolian transport: Grain-scale interactions, dynamical mechanisms and scaling laws. Aeolian Research, 3(3), 243-270.

Eastwood, E. N., Kocurek, G., Mohrig, D., & Swanson, T. (2012). Methodology for reconstructing wind direction, wind speed and duration of wind events from aeolian cross-strata. Journal of Geophysical Research: Earth Surface, 117(F3).

Edgett, K. S., & Malin, M. C. (2000). New views of Mars eolian activity, materials, and surface properties: Three vignettes from the Mars Global Surveyor Mars Orbiter Camera. Journal of Geophysical Research: Planets, 105(E1), 1623-1650.

Fishbaugh, K. E., & Head, J. W. (2000). North polar region of Mars: Topography of circumpolar deposits from Mars Orbiter Laser Altimeter (MOLA) data and evidence for asymmetric retreat of the polar cap. Journal of Geophysical Research: Planets, 105(E9), 22455-22486.

Fishbaugh, K. E., & Head III, J. W. (2005). Origin and characteristics of the Mars north polar basal unit and implications for polar geologic history. Icarus, 174(2), 444-474.

Fouchet, T., Lellouch, E., Ignatiev, N. I., Forget, F., Titov, D. V., Tschimmel, M., ... & Encrenaz, T. (2007). Martian water vapor: Mars Express PFS/LW observations. Icarus, 190(1), 32-49.

Geissler, P. E. (2014). The birth and death of transverse aeolian ridges on Mars. Journal of Geophysical Research: Planets, 119(12), 2583-2599.

Grotzinger, J. P., Crisp, J., Vasavada, A. R., Anderson, R. C., Baker, C. J., Barry, R., ... & Gellert, R. (2012). Mars Science Laboratory mission and science investigation. Space science reviews, 170(1-4), 5-56.

Haberle, R. M., & Jakosky, B. M. (1990). Sublimation and transport of water from the north residual polar cap on Mars. Journal of Geophysical Research: Solid Earth, 95(B2), 1423-1437.

Haberle, R. M., Leovy, C. B., & Pollack, J. B. (1982). Some effects of global dust storms on the atmospheric circulation of Mars. Icarus, 50(2-3), 322-367.

Hanel, R., Conrath, B., Hovis, W., Kunde, V., Lowman, P., Maguire, W., ... & Levin, G. (1972). Investigation of the Martian environment by infrared spectroscopy on Mariner 9. Icarus, 17(2), 423-442.

Hansen C. J.et al., 2012. Seasonal Erosion and Restoration of Mars' Northern Polar Dunes. Science 331 (6017), 575-578. DOI: 10.1126/science.1197636

Hayward, R. K., Mullins, K. F., Fenton, L. K., Hare, T. M., Titus, T. N., Bourke, M. C., ... & Christensen, P. R. (2007). Mars global digital dune database and initial science results. Journal of Geophysical Research: Planets, 112(E11).

Herkenhoff, K. E., & Plaut, J. J. (2000). Surface ages and resurfacing rates of the polar layered deposits on Mars. Icarus, 144(2), 243-253.

Herny, C., Massé, M., Bourgeois, O., Carpy, S., Le Mouélic, S., Appéré, T., ... & Rodriguez, S. (2014). Sedimentation waves on the Martian north polar cap: analogy with megadunes in Antarctica. Earth and Planetary Science Letters, 403, 56-66.

Holstein-Rathlou, C., Gunnlaugsson, H. P., Merrison, J. P., Bean, K. M., Cantor, B. A., Davis, J. A., ... & Hviid, S. F. (2010). Winds at the Phoenix landing site. Journal of Geophysical Research: Planets, 115(E5).

Howard, A. D. (2000). The role of eolian processes in forming surface features of the Martian polar layered deposits. Icarus, 144(2), 267-288.

Hudson, T. L., Aharonson, O., Schorghofer, N., Farmer, C. B., Hecht, M. H., & Bridges, N. T. (2007). Water vapor diffusion in Mars subsurface environments. Journal of Geophysical Research: Planets, 112(E5).

Hugenholtz, C. H., & Barchyn, T. E. (2017). A terrestrial analog for transverse aeolian ridges (TARs): Environment, morphometry, and recent dynamics. Icarus, 289, 239-253.

Ingersoll, A. P., Summers, M. E., & Schlipf, S. G. (1985). Supersonic meteorology of Io: Sublimation-driven flow of SO2. Icarus, 64(3), 375-390.

Kieffer, H. H., Chase, S. C., Martin, T. Z., Miner, E. D., & Palluconi, F. D. (1976). Martian north pole summer temperatures: Dirty water ice. Science, 194(4271), 1341-1344.

Kok, J. F., Parteli, E. J., Michaels, T. I., & Karam, D. B. (2012). The physics of wind-blown sand and dust. Reports on progress in Physics, 75(10), 106901.

Koutnik, M., Byrne, S., & Murray, B. (2002). South polar layered deposits of Mars: The cratering record. Journal of Geophysical Research: Planets, 107(E11).

Lancaster, N. (1988). The development of large aeolian bedforms. Sedimentary Geology, 55(1-2), 69-89.

Lancaster, N., (1995). Geomorphology of Desert Dunes. Routledge.

Langevin, Y., Poulet, F., Bibring, J. P., Schmitt, B., Douté, S., & Gondet, B. (2005). Summer evolution of the north polar cap of Mars as observed by OMEGA/Mars express. Science, 307(5715), 1581-1584.

Lapotre, M. G. A., Ewing, R. C., Lamb, M. P., Fischer, W. W., Grotzinger, J. P., Rubin, D. M., ... & Banham, S. G. (2016). Large wind ripples on Mars: A record of atmospheric evolution. Science, 353(6294), 55-58.

Laskar, J., Levrard, B., & Mustard, J. F. (2002). Orbital forcing of the Martian polar layered deposits. Nature, 419(6905), 375.

Mangold, N. (2005). High latitude patterned grounds on Mars: Classification, distribution and climatic control. Icarus, 174(2), 336-359.

Massé, M., Bourgeois, O., Le Mouélic, S., Verpoorter, C., Spiga, A., & Le Deit, L. (2012). Wide distribution and glacial origin of polar gypsum on Mars. Earth and Planetary Science Letters, 317, 44-55.

McCauley, J. F., Carr, M. H., Cutts, J. A., Hartmann, W. K., Masursky, H., Milton, D. J., ... & Wilhelms, D. E. (1972). Preliminary Mariner 9 report on the geology of Mars. Icarus, 17(2), 289-327.

McEwen, A. S., Eliason, E. M., Bergstrom, J. W., Bridges, N. T., Hansen, C. J., Delamere,

W. A., ... & Kirk, R. L. (2007). Mars reconnaissance orbiter's high resolution imaging science experiment (HiRISE). Journal of Geophysical Research: Planets, 112(E5).

McKee, E. D., (1979). A Study of Global Sand Seas. U.S. Government Printing Office.

Melosh, H. Jay, (2011). Planetary surface processes. Cambridge University Press.

Moores, J. E., Lemmon, M. T., Smith, P. H., Komguem, L., & Whiteway, J. A. (2010). Atmospheric dynamics at the Phoenix landing site as seen by the Surface Stereo Imager. Journal of Geophysical Research: Planets, 115(E1).

Moores, J. E., Lemmon, M. T., Rafkin, S. C., Francis, R., Pla-Garcia, J., de la Torre Juárez, M., ... & Mischna, M. (2015). Atmospheric movies acquired at the Mars Science Laboratory landing site: Cloud morphology, frequency and significance to the Gale Crater water cycle and Phoenix mission results. Advances in Space Research, 55(9), 2217-2238.

Moores, J. E., Smith, C. L., Toigo, A. D., & Guzewich, S. D. (2017). Penitentes as the origin of the bladed terrain of Tartarus Dorsa on Pluto. Nature, 541(7636), 188.

Mustard, J. F., Adler, M., Allwood, A., Bass, D. S., Beaty, D. W., Bell, J. F., ... & Edgett, K. S. (2013). Report of the mars 2020 science definition team. Mars Explor. Progr. Anal. Gr, 155-205.

Parish, T. R., & Howard, A. D. (1993). Numerical simulation of thermally induced near-surface flows over Martian terrain.

Pelletier, J. D. (2009). Controls on the height and spacing of eolian ripples and transverse dunes: A numerical modeling investigation. Geomorphology, 105(3-4), 322-333.

Petrosyan, A., Galperin, B., Larsen, S. E., Lewis, S. R., Määttänen, A., Read, P. L., ... & Spiga, A. (2011). The Martian atmospheric boundary layer. Reviews of Geophysics, 49(3).

Rasmussen, K. R., Valance, A., & Merrison, J. (2015). Laboratory studies of aeolian sediment transport processes on planetary surfaces. Geomorphology, 244, 74-94.

Rubin, D. M., & Hunter, R. E. (1985). Why deposits of longitudinal dunes are rarely recognized in the geologic record. Sedimentology, 32(1), 147-157.

Savijärvi, H., & Siili, T. (1993). The Martian slope winds and the nocturnal PBL jet. Journal of the Atmospheric Sciences, 50(1), 77-88.

Seu, R., Phillips, R. J., Biccari, D., Orosei, R., Masdea, A., Picardi, G., ... & Smrekar, S. E. (2007). SHARAD sounding radar on the Mars Reconnaissance Orbiter. Journal of Geophysical Research: Planets, 112(E5).

Silvestro, S., Fenton, L. K., Vaz, D. A., Bridges, N. T., & Ori, G. G. (2010). Ripple migration and dune activity on Mars: Evidence for dynamic wind processes. Geophysical Research Letters, 37(20).

Smith, D. E., & Zuber, M. T. (1998). The relationship between MOLA northern hemisphere topography and the 6.1-Mbar atmospheric pressure surface of Mars. Geophysical research letters, 25(24), 4397-4400.

Smith, D. E., Zuber, M. T., Frey, H. V., Garvin, J. B., Head, J. W., Muhleman, D. O., ... & Banerdt, W. B. (2001). Mars Orbiter Laser Altimeter: Experiment summary after the first year of global mapping of Mars. Journal of Geophysical Research: Planets, 106(E10), 23689-23722.

Smith, I. B., & Holt, J. W. (2010). Onset and migration of spiral troughs on Mars revealed by orbital radar. Nature, 465(7297), 450.

Smith, I. B., & Holt, J. W. (2015). Spiral trough diversity on the north pole of Mars, as seen by Shallow Radar (SHARAD). Journal of Geophysical Research: Planets, 120(3), 362-387.

Smith, I. B., Spiga, A., & Holt, J. W. (2015). Aeolian processes as drivers of landform evolution at the South Pole of Mars. Geomorphology, 240, 54-69.

Smithsonian, (1984). Smithsonian Met. Tables, 5th ed, p.350.

Soderblom, L. A., Malin, M. C., Cutts, J. A., & Murray, B. C. (1973). Mariner 9 observations of the surface of Mars in the north polar region. Journal of Geophysical Research, 78(20), 4197-4210.

Tanaka, K. L. (2005). Geology and insolation-driven climatic history of Amazonian north polar materials on Mars. Nature, 437(7061), 991.

Taylor, P. A., Kahanpää, H., Weng, W., Akingunola, A., Cook, C., Daly, M., ... & Polkko, J. (2010). On pressure measurement and seasonal pressure variations during the Phoenix mission. Journal of Geophysical Research: Planets, 115(E3).

Thomas, P. C., & Gierasch, P. J. (1995). Polar margin dunes and winds on Mars. Journal of Geophysical Research: Planets, 100(E3), 5397-5406.

Thomas, P. C., Malin, M. C., Edgett, K. S., Carr, M. H., Hartmann, W. K., Ingersoll, A. P., ... & Sullivan, R. (2000). North–south geological differences between the residual polar caps on Mars. Nature, 404(6774), 161.

Thomas, P. C., Calvin, W., Cantor, B., Haberle, R., James, P. B., & Lee, S. W. (2016). Mass balance of Mars' residual south polar cap from CTX images and other data. Icarus, 268, 118-130.

Tsoar, H., Greeley, R., & Peterfreund, A. R. (1979). Mars: The north polar sand sea and related wind patterns. Journal of Geophysical Research: Solid Earth, 84(B14), 8167-8180.

Tsoar, H. & Greeley, R. (1980). Estimate of Characteristic Grain Sizes for Martian Dunes. R. LUNAR AND PLANETARY SCIENCE XI, P. 1169-1171.

Vaz, D. A., Silvestro, S., Sarmento, P. T., & Cardinale, M. (2017). Migrating meter-scale bedforms on Martian dark dunes: Are terrestrial aeolian ripples good analogues?. Aeolian Research, 26, 101-116.

Welch, P. (1967). The use of fast Fourier transform for the estimation of power spectra: a method based on time averaging over short, modified periodograms. IEEE Transactions on audio and electroacoustics, 15(2), 70-73.

Wilson, I. G. (1973). Ergs. Sedimentary geology, 10(2), 77-106.

Zimbelman, J. R. (2010). Transverse aeolian ridges on Mars: First results from HiRISE images. Geomorphology, 121(1-2), 22-29.

Glossary

Aeolian: processes involved in sediment transport caused by the general wind.

Barchan: dune form with a characteristic crescent shape on their slipface.

Braided (terrain): a subset of transverse dunes formed under a bimodal wind regime with orthogonal directions.

Crest: the tip of the dune; generally the highest point of a dune.

Erg: large area consisting of dune fields which may have complex dune forms.

HiRISE: High Resolution Imaging Scientific Experiment; high resolution camera on the Mars Reconnaissance Orbiter.

Insolation: incoming solar radiation.

Katabatic: winds caused cold dense air accelerating down a slope.

Lambertian: type of reflectance where light is reflected uniformly in all directions.

Laminar: Viscous flow characteristic of a low Reynolds number.

Lee: the side of the dune downstream from the crest.

Penitentes: surface features that are formed from sublimation. Internal reflection of incoming solar flux of can sublimate the surface unevenly forming ice/snow patterns.

Reptation: process where grains are displayed by incoming saltating grains; the ejected

grains are lifted due to the splash made by the impacts.

Saltation: process where grains are displaced via lifting by the wind.

Sastrugies: linear dunes composed of snow generally found in arctic regions.

Stoss: the side of the dune upstream from the crest.

Suspension: process where small grains are lifted by the wind and remain in the air indefinitely.

TAR: Transverse Aeolian Ridge; a type of surface feature common on Mars likely to be aeolian in origin.

Tractation: process that creates fluid-dragged ripples.